Ionizing Radiation Quality and Dose Effects on DNA Double Strand Break Repair

Stefan J. Roobol

IONIZING RADIATION QUALITY AND DOSE EFFECTS ON DNA DOUBLE STRAND BREAK REPAIR

Stefan J. Roobol

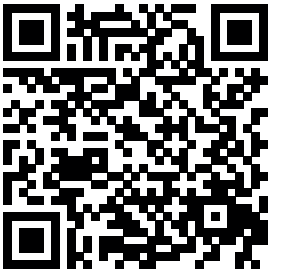

ISBN: 978-94-6361-516-7

Cover design	Studio LookOut!
Lay-out	Optima
Printed by	Optima

The studies presented in this thesis were mainly performed at the department of Molecular Genetics and Radiology & Nuclear Medicine of the Erasmus University Medical Centre, Rotterdam, The Netherlands

IONIZING RADIATION QUALITY AND DOSE EFFECTS ON DNA DOUBLE STRAND BREAK REPAIR

Effecten van eigenschappen en dosering van ioniserende straling op DNA-dubbelstrengs breuk reparatie

Proefschrift

Ter verkrijging van de graad van doctor aan de
Erasmus Universiteit Rotterdam
op gezag van de
rector magnificus

Prof.dr. F.A. van der Duijn Schouten

en volgens besluit van het College voor Promoties.
De openbare verdediging zal plaatsvinden op

9 maart 2021 om 15.30 uur

door

Stefan Johan Roobol
geboren te Rotterdam

Erasmus University Rotterdam

Erasmus

Promotoren

Prof. dr. R. Kanaar
Prof. dr. ir. M. De Jong

Overige leden

Prof. dr. A. B. Houtsmuller
Dr. ir. A.G. Denkova
Prof. dr. ir. J.A.F. Marteijn

Copromotoren

Dr. J. Essers
Dr. D.C. van Gent

Printing of this thesis was supported by:
Stichting Wetenschappelijk Onderzoek Prostaatkanker (SWOP)

CONTENTS

1

General Introduction

DNA damage

Human cells are continuously exposed to numerous exogenous and endogenous agents that damage the DNA. DNA damage alters replication and transcription, causes cell death, and can lead to mutations and oncogenic transformations. Ionizing Radiation (IR) is considered an exogenous DNA damaging factor which cells are exposed to either environmentally or as anthropogenic genotoxic agent. The DNA damage inflicted by IR is considered harmful, leading to mutations or oncogenic transformations, or helpful as therapy to induce cell death in cancer cells. DNA Double Stranded Breaks (DSBs) are inflicted by IR and are the most dangerous since they can cause permanent DNA damage such as deletions and translocations eventually leading to cell death or oncogenic transformations [1]. To counteract these deleterious actions, cells have evolved a number of DNA repair systems that each can repair a subset of these lesions. In this thesis, we focus on the analysis of induction and the repair of DBSs.

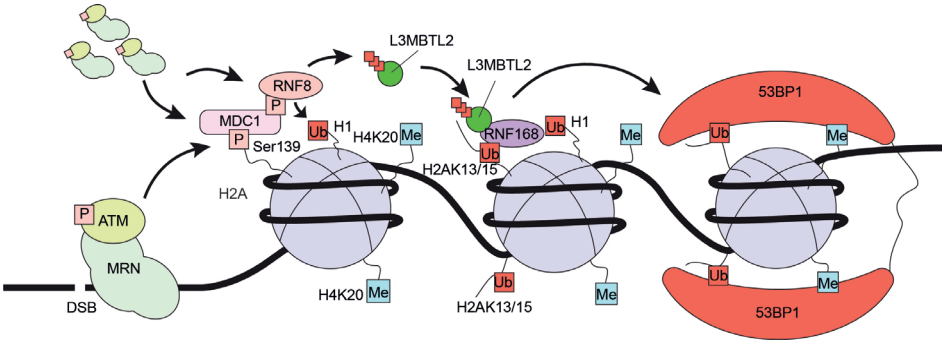

Figure 1. Schematic overview of chromatin signaling following DNA damage. *DSBs sensing by MRN leads to ATM mediated phosphorylation of the histone variant H2A (γH2AX) resulting in a positive feedback loop, recruiting more MRN/ATM complexes. ATM mediated phosphorylation of MDC1 initiates the recruitment of RNF8, which is the start of an ubiquitination cascade starting with the polyubiquitination of L3MBTL2 and histone H1. Both ubiquitinated L3MBTL2 and Histone H1 are recognized by RNF168, resulting in the ubiquitination of H2A at positions K13 and/or K15 (H2AK13/15). The ubiquitination of H2A together with the methylation of H4 (H4K20) serve as a scaffold that is recognized by 53BP1. The accumulation of 53BP1 protects DNA-ends from resection, thereby facilitating DSB repair pathway choice.*

Recognition of DSBs is the first step after IR hits cells (Figure 1). One of the first players in the process is the MRN-complex, a ring shaped complex consisting of three different proteins. The complex consists of the monomeric Nijmegen Breakage Syndrome 1 (NBS1) protein, which functions as a scaffold for two RAD50, and two Meiotic Recombination 11 (Mre11) proteins. The two RAD50 proteins form the ring that slides over the DNA break [2-4]. When the MRN-complex is bound to the DSB the serine/threonine kinase Ataxia Telangiectasia Mutated (ATM) is recruited and binds to the C-terminus of NBS1 [5]. ATM is then activated by auto-phosphorylation which separates the dimer into two active monomers [6]. Once activated, ATM phosphorylates proteins downstream of the DNA repair pathway. One important regulating

step is phosphorylation of histone H2AX at the serine-139 (γH2AX) residue by ATM [7]. γH2AX recruits proteins necessary for the next step in DNA repair. Mediator of DNA damage checkpoint 1 (MDC1) is directly recruited by γH2AX where its Ser-Asp-Thr (SDT) domain is phosphorylated by casein kinase 2 (CK2) [8, 9]. MDC1 amplifies the DNA damage signal by creating a positive feedback loop to concentrate MRN-ATM complexes at the DSB site, which will phosphorylate additional H2AX histones [10]. Recruited MRN-ATM complexes will phosphorylate the T-Q-X-F domain of MDC1 [11]. This phosphorylated MDC1 recruits the E3 ubiquitin-protein ligase RNF8 to the damage site, starting an ubiquitination cascade [12]. RNF8 ubiquinates both histone H1 and L3MBTL2, this attracts RNF168, a second E3 ubiquitin protein ligase [13,14]. RNF168 mono-ubiquitinates lysine (K) 13-15 residues of histones of the H2A family, forming K63 ubiquitin chains [14]. This ubiquitinated histone can be recognized by a dimer of p53-binding protein 1 (53BP1) [15]. This also requires interaction of 53BP1 with histone H4 methylated on lysine 20 (H4K20me) [16]. These alterations are recognized by the ubiquitination-dependent recruitment (UDR) motif and Tudor motif, respectively [15, 17]. 53BP1 then accumulates at the damaged site [18]. With no demonstrated enzymatic activity, 53BP1 is encoded by the TP53BP1 gene and has 1972 amino acids [19, 20]. 53BP1 has several important structural elements which include two BRCA1 carboxy-terminal (BRCT) domains, one glycine/arginine-rich region (GAR), multiple tandem Tudor domains and two dynein 8 kD light chain (LC8) binding sites. In addition, 53BP1 includes 32 PIK kinases and 41 cyclin-dependent kinase (CDK) phosphorylation sites [19]. The majority of these sites have been linked to roles in signaling after ionizing radiation (IR), protein interactions and cell cycle checkpoints [21-23]. The purpose of 53BP1 accumulation is to protect DNA ends from resection. Therefore, it is thought that 53BP1 recruitment, retention, and exclusion determines which DSB repair pathway is activated. There are four pathways by which the DSB can be repaired; the two major pathways Non-Homologous End Joining (NHEJ) and Homologous Recombination (HR), and two less common pathways Alternative End Joining (A-EJ) and Single Strand Annealing (SSA).

Non-homologous End Joining

The most direct way to repair a DSB is to ligate the break ends together, by NHEJ which is considered the most available pathway during cell cycle, albeit error-prone [24] (Figure 2). DNA ends at the damaged site are recognized by the heterodimer of Ku70 and Ku80, which forms a ring fitting directly on the broken DNA and thereby protecting the DNA ends from resection [25, 26]. Unlike any other DSB repair pathway, NHEJ requires no sequence homology [27]. The Ku70/Ku80 heterodimer recruits the DNA-PK catalytic subunit (DNA-PKcs) via a flexible linker its C-terminal region, composing the DNA-PK complex and stabilizing the DNA-ends. Recruitment of Artemis induces the assembly of the Artemis:DNA-PK complex, which opens up an variety of nuclease activities, being able to trim many kinds of DNA damaged ends for end-joining [27]. The addition of Artemis complements the whole DNA-PK complex, replacing the complex upstream for DNA-PKcs to be positioned at the DSB [28]. To finalize the DSB repair, the DNA

ends are stabilized and positioned by XLF and PAXX. Then, the factor XRCC4 activates DNA ligase IV (LIGIV), which ligates the ends [29].

Homologous recombination

A second pathway to repair DSB is Homologous Recombination (HR). Whilst only possible when a sister chromatid is available (S/G2 phase), this pathway is error-free and operational when DNA breaks do not consist of polished ends but are missing nucleotides (Figure 2) [30]. The start of the HR is initialized by the aforementioned MRN complex, which initializes the resection of the broken ends. Hereafter, the recruitment of CtIP, which is in complex with BRCA1, completes resection up to a couple of hundred nucleotides [31, 32]. Exonuclease 1 (EXO1), DNA replication helicase/nuclease 2 (DNA2) or the Bloom syndrome (BLM) complexes then process this early resection intermediate to generate longer 3' single stranded DNA (ssDNA) overhangs [33, 34]. These large 3' overhangs are highly susceptible for degradation by nucleases. Replication protein A (RPA) has high affinity to bind to single stranded DNA and will bind to 3' overhangs, which stabilizes ssDNA and protects it from nucleases [35]. Effective repair of HR relies on homology (>100 bp) with the daughter strand [36]. First, RPA has to be replaced by Rad51. This is done via the mediator protein BRCA2, which is recruited by BRCA1 through PALB2 [37]. Rad51 is transported to the resection by BRCA2, allowing Rad51 to bind ssDNA and displace RPA, wrapped around the ssDNA in a helical way [38]. This Rad51-ssDNA filament then facilitates the search for a homologous sister chromatid. Rad54 facilitates this search and has been described to have many functions all involved in the binding to a homologous chromatid, called synapsis, extensively reviewed in [39]. Pre-synapsis, Rad54 is described to stabilize and assist Rad51 filaments on the ssDNA, not requiring any ATP activity by RAD54 [40]. During synapsis, Rad54 shows ATP-dependent facilitation of Rad51 filaments in translocating along the DNA and clearing of nucleosomes from the synapsis site through chromatin remodeling activity. Lastly, post-synapsis Rad54 enhances D-loop formation with Rad51, assisted by PALB2, and is necessary for the dissociation of Rad51 from the DNA [41-43]. Once Rad51 is dissociated from the ssDNA, proliferating cell nuclear antigen (PCNA) can be loaded onto the D-loop. PCNA can stimulate the activity of Pol δ and pol η which carry out post invasion DNA synthesis, leading to the repair and resolving of the intertwined DNA molecule [44].

Alternative End Joining

Alternative end-joing (A-EJ) mainly occurs in the absence of key components of the NHEJ pathways, such as Ku70/80 or LIGIV. Repair of DSBs via A-EJ is based on joining the two DNA ends together, very similar as NHEJ [45]. However, most A-EJ repair requires limited 5' to 3' DNA end resection (up to 20 nucleotides) with 3-8 bp of homology within the resected ssDNA tails [46]. The limited resection is initiated by the MRE11 nuclease, leaving short ssDNA overhangs [47]. In these overhangs, minimal annealing takes place, generating micro homology, as short as 3-8 bp, promoted by DNA polymerase θ (Polθ) and its unique helicase-like domain at its N-

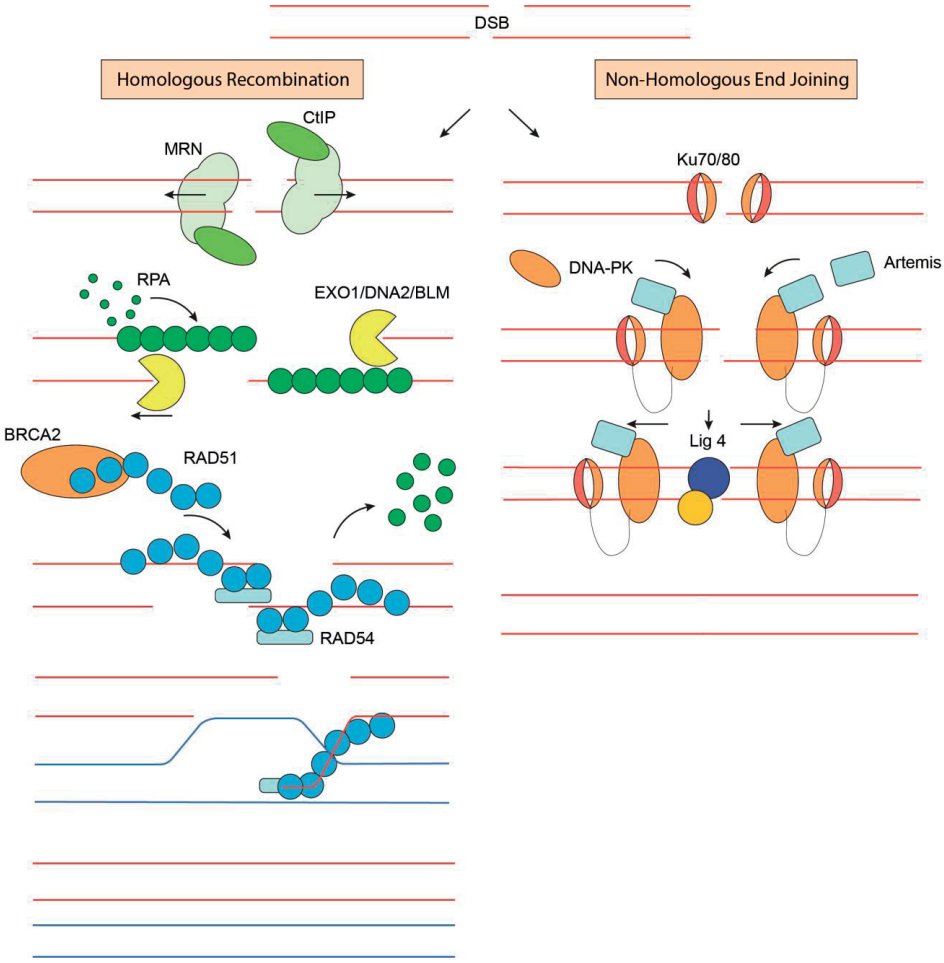

Figure 2. A schematic overview of DSB repair. *The initial step of Homologous Recombination (HR, left) the DNA is resected by MRN and CtIP, leading to long-range resection by EXO1, DNA2 or BLM. Resection of double stranded DNA results in single stranded DNA, which is protected from degradation by RPA. HR processing requires the recombinase protein RAD51 that is recruited via BRCA2 and replaces RPA on the single stranded DNA. Recruitment of RAD54 stimulates the strand invasion of the homologous daughter strand (blue) resulting in DSB repair. During Non-Homologous End Joining (NHEJ, right), DNA ends are recognized by the dimer Ku70/80 resulting in the protection of DNA ends. The DNA-PK complex in combination with Artemis processes DNA ends that are not resected. In the end, processed DNA ends are ligated by LIGIV, which is facilitated by XRCC4.*

terminus. Such annealing of micro homologies generates overhanging bases that are removed by nucleases generating gaps, which are in turn filled by Polθ. The double function of Polθ leads to the unique possibility to stabilize the annealing of two ssDNA tails with as little as 3 bp of homology [48, 49].

Single Strand Annealing

Similar as to HR, repair via the single strand annealing (SSA) pathway is limited to the late S and G2 phase and requires resection. The difference between HR and SSA is the extend of homology. HR requires a daughter strand to have more than 100 bp homology, whereas SSA typically requires homology of 50 bp [50]. Thus, when extensive resection takes place, but does not meet the requirements of HR, annealing of homologous bp takes place, facilitated by RAD52 [51]. Just like in A-EJ, annealing of homologous bp within a DNA strand generates overhanging bases, which have no homology. These non-complementary overhangs are removed by the endonuclease XPF-ERCC1. Finally, the remaining nicks are sealed by LIG1. Due to the removal of non-complementary sequences, SSA is a highly deleterious pathway [52].

DSB repair pathway choice

Almost all DSBs that are inflicted outside the S and G2 phase are repaired by NHEJ in human cells and even within the G2 phase, up to 80% of IR induced DSBs are repaired by NHEJ [53]. However, the other pathways still play a crucial part in DSB repair. The choice between these DSB repair pathways is dictated by the extent of homology. There is an increasing requirement for homology from NHEJ (0-4 bp), A-EJ (3-8 bp), SSA (>50 bp) and HR (>100 bp) (Figure 3) [54]. The extent of homology is a direct consequence of the resection length, which is in turn tightly regulated by by end resection factors, such as CtIP/BRCA1 or the MRN complex and DNA end protection protein, such as 53BP1, RAP1-interacting factor 1 (RIF1) and the shieldin complex [55-58].

CtIP and MRN, generating 3’ ssDNA, mediate initial DNA end resection. This short ssDNA serves as scaffold for long-ranged resection by EXO1, DNA2 and BLM [59]. Processes such as HR, degradation of faulty replicated DNA, and DSB repair choice rely on effective DNA end resection. Therefore, initiation, extension, and termination of DNA end resection is strictly regulated and involves many mechanisms. The accumulation of 53BP1 protects DNA end from resection which involves interactions with replication timing regulatory factor 1 (RIF1) [60]. In turn, RIF1 recruits the Shieldin complex consisting of SHLD1, 2, 3 and REV7 [58, 61, 62]. Like 53BP1, the shieldin complex has no known enzymatic activity. Furthermore, the presence of BRCA1 and CtIP is thought to antagonize the accumulation of 53BP1 in late S and G2 phases, thereby limiting DNA end protection and promoting HR over NHEJ [60, 63]. Together, these observations suggest that pathway choice, which is based on the extent of homology, is regulated by opposing roles of DNA end resection factors in combination with factors, which protect DNA ends from (extended) resection.

Ionizing radiation induced foci

The recruitment of repair factors to damaged chromatin sites requires complex spatial and temporal coordination among the proteins and within the chromatin. This assembly and modifications of proteins in reaction to DSBs can be visualized microscopically and are called ionizing

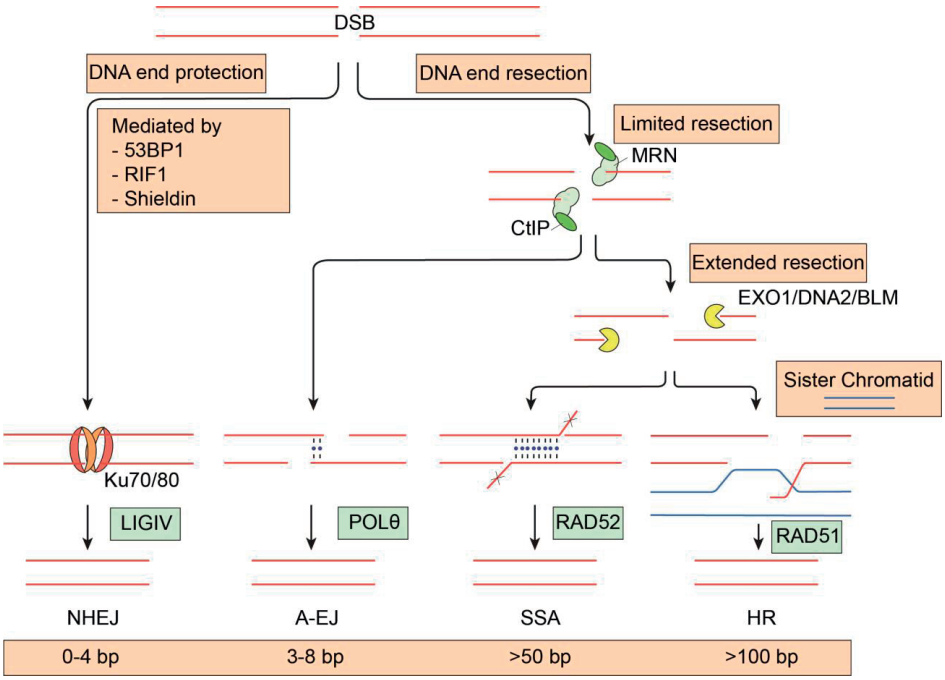

Figure 3. The influence of resection extent on DSB repair pathway choice. *The choice between Non-Homologous End Joining (NHEJ), Alternative End Joining (A-EJ), Single Strand Annealing (SSA) and Homologous Recombination (HR) is mostly a consequence of the extend of homology between the DNA ends of the DSB. The homology between the two DNA ends is regulated by the range of DNA end resection, depending on how well DNA ends are protected from nucleolytic resection. Factors such as p53 binding protein 1 (53BP1), RAP1-interacting factor 1 (RIF1) and the shielding complex (Shieldin) protect DNA ends, limiting resection and thereby allowing recruitment of the Ku70/80 dimer. This leads to the repair via the NHEJ pathway in which LIGIV plays a crucial role in ligating DNA ends together. On the other hand, if DNA end protection is limited, DNA end resection is initiated by CtBP-interacting protein (CtIP) and the MRE11-RAD50-NBS1 (MRN) endonuclease complex allowing limited homology, leading to A-EJ in which Polymersase θ (POLθ) is involved. In the case of absent DNA end protection, long-range resection is mediated by nucleases Bloom syndrome protein (BLM), DNA replication ATP-dependent helicase/nuclease (DNA2) and exonuclease 1 (EXO1). Long ranged homology leads to SSA in which the annealing of the homologous base pairs is mediated by RAD52 and where non-homologous sequences are cut off (indicated by the crosses). In the case of the presence of a homologous sister chromatid in which the extend of homology is even larger; HR takes in which RAD51 plays an essential role in strand invasion. The range of homology is indicated below each pathway in the highlighted box. Figure is adapted from [54].*

radiation-induced foci (IRIF) [64]. With the use of indirect immunofluorescence or by tagging protein of interest with fluorescent tags, like GFP the understanding of proteins residing in IRIF and their retention in these structures has broadened and has led to the quantitative observation of an increase of the number of IRIF per cell in a dose-dependent manner [65]. In addition, IRIF number and size change over time following IR, which could be used as surrogate marker for DNA damage processing [66, 67]. Two of the most commonly known DSB markers are γH2AX and 53BP1. As these two markers do not discriminate between possible DSB repair pathways,

functional protein in the HR pathway are often used to quantify HR specific repair [68]. Markers such as RAD51 and BRCA2 are the most used protein to investigate HR repair. In addition, RPA is used to investigate resection, which is essential for HR.

Radiotherapy

Inducing DNA damage in tumor cells to halt their division and growth is an important basis for several cancer treatments. Radiotherapy (RT) is an important tool to treat cancer and is estimated to be used in two-third of all cancer patients, as unique or combined treatment [69]. RT is based on IR, which is radiation with sufficient energy to change the material through which it passes and therefore inflicting several types of DNA damage. IR deposits energy to the material, which it is passing through. A measure of how much energy IR transfers to material is characterized as the linear energy transfer (LET). By definition, LET is the amount of energy transferred to the material the IR traverses per unit distance [70]. A high LET means that a particle generates an abundance of dense ionizations in the matter it traverses, depositing a large amount of energy. The amount of deposited energy has a direct effect on the penetration depth in the material and is different between types of IR (Figure 4A). Dosimetry is used to understand this difference by evaluating radiation-weighting factors, such as the absorbed dose. Mostly, these differences are dependent on the type of radiation and the energy that they carry [71]. Deposition of similar energy by two different IR types could lead to other biological effect, such as increased cell death. This increased effect can be calculated as a ratio, leading to the relative biological effectiveness (RBE), which if generally higher using high-LET irradiation.

In this thesis, we focus on two different applications of radiotherapy: External beam radiotherapy (EBRT) and Radiopharmaceutical therapy (RPT). The basis of EBRT is treatment from outside, thereby irradiating a specific part of the body, which contains the cancer. For example, to treat lung cancer, a large part of the chest is irradiated. Unlike EBRT, with RPT the radioactivity is administered in the bloodstream, delivering the cytotoxic radiation directly to cancer cells. Important to note: an external beam delivers the irradiation per cell regardless of the number of cells. However, in RPT, the number of cells that are clustered together influences the absorbed irradiation per cell and the number of cells that have been targeted (Figure 4B).

External Beam Radiotherapy

External beam radiotherapy (EBRT) can be performed using photons, protons, or electrons. The most used radiation type in EBRT are photons (X-rays), which can penetrate the body and reach tumors located deep in the body. X-rays are a form of electromagnetic radiation, which consists of waves propagating through space that carry electromagnetic radiant energy. The wavelength of X-rays is in the range of 0.1 to 10 nm, giving them a corresponding energy of 100 eV to 100 keV [72]. Important to note: X-rays are not the same as gamma rays (γ-rays). The X-rays are artificially generated by accelerating electrons, which collide with a metal target, whereas γ-rays originate from atoms during radioactive decay. In addition, the maximum energy of the

produced X-ray spectrum can be controlled, whereas the energy of an emitted γ-ray from a certain atom is always the same. However, despite these differences, X-rays generated with a certain energy have the same potential in causing DNA damage as that of γ-rays harboring that same energy naturally.

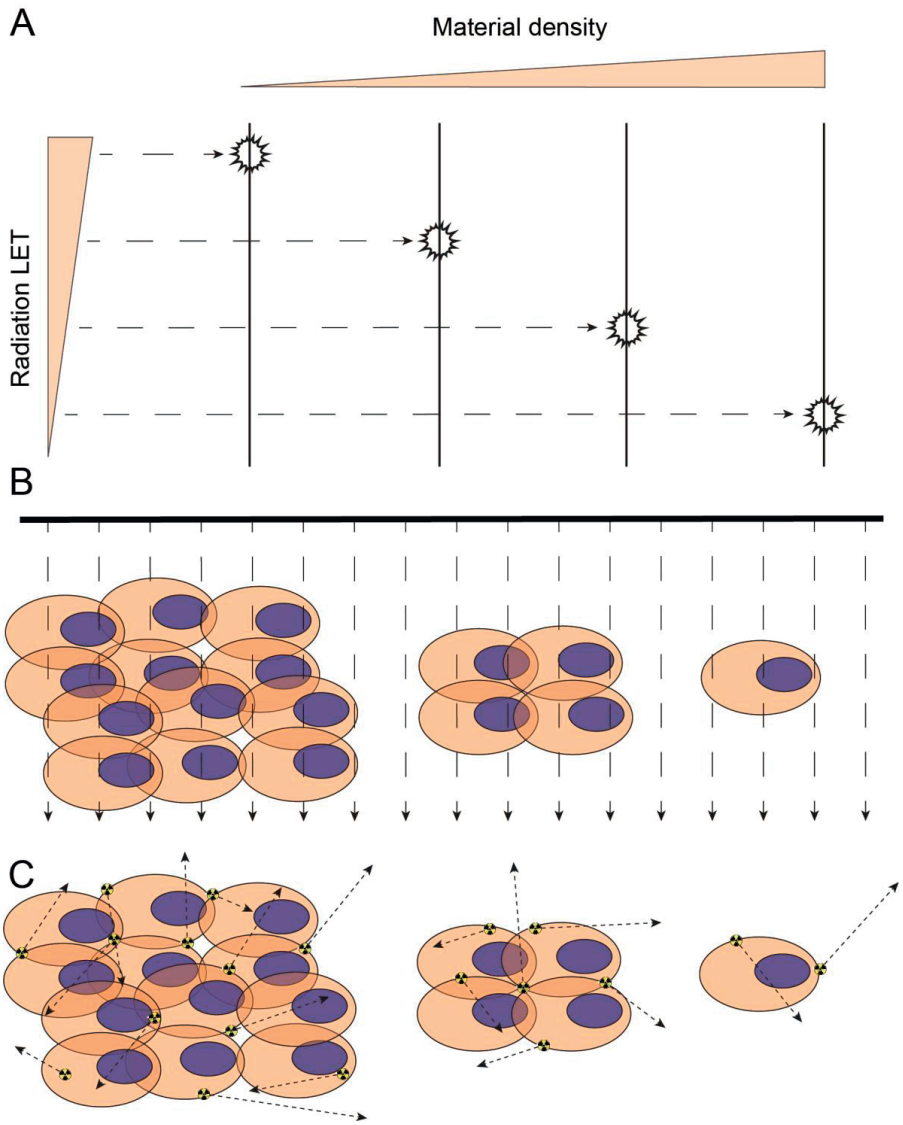

Figure 4. Penetration depth of IR and radiation delivery of EBRT or RPT. *(A) Schematic overview of the increasing penetration depth of IR in dense material with decreasing LET. (B) External Beam Radiation Therapy (EBRT) will deliver the same dose to cells, regardless of how large the targeted tumor is. However, in Radiopharmaceutical Therapy (RPT) (C), the delivered dose is dependent on the range of radioactive emission and the number of cells in which the radioactivity successfully is delivered.*

X-rays are generated with relatively low energy and have a low-LET, producing dispersed DNA damage throughout cell nuclei (Figure 5A). In addition, the types DNA damage induced by X-ray irradiation (mainly DNA single stranded breaks) are comparable with endogenous DNA damage in which 75% of the DNA damage is comprised of single stranded breaks [73]. Hence, the DNA damage repair pathways are highly efficient in repairing such damage. Therefore, the RBE values of X-rays are low, compared to other types of IR, which inflict more complex DNA damage for which repair is more difficult. Therefore, EBRT requires high X-ray doses during treatment, causing situations involving unacceptable toxicities toward healthy tissues in the patient. For example, metastasized cancer or tumors which are located in the vicinity of crucial or sensitive organs will lead to off target irradiation exposure [74]. A more targeted approach such as RPT offers the possibility to treat tumor cells specifically, reducing possible side effects.

Radiopharmaceutical Therapy

The use of RPT is defined by delivering radionuclides to tumor cells using specific tumor-associated (molecular) targets. Unlike EBRT, when RPT is administered, the cytotoxic radiation is delivered systemically in the body, much like chemotherapy. Targeting the radionuclide to specific tumor cells or their microenvironment is done using delivery carriers that either recognize specific endogenous targets of tumor cells or accumulate in microenvironments surrounding the tumor. Due to the systemic approach, development of RPT has been a highly multidisciplinary field, including expertise in oncology, radiobiology, pharmacology, radiochemistry, dosimetry, medical physics, and radionuclide imaging. This wide array of practitioners has led to a lack of focus in development. However, the shown efficacy with minimal toxicity in combination with a remarkable potential of RPT has led the attention of pharmaceutical companies and thereby a large financial benefit [75, 76].

Although the base knowledge of killing tumor cells by radiation is similar between RPT and EBRT, delivering radionuclides specifically to tumor cells, as is done in RPT, has unique properties which need to be understood to employ the full potential of RPT [77]. For example, the delivered dose using PRT is cumulative over several weeks, while in radiotherapy that same dose is delivered in short fragments, creating a large difference in the administered dose rate [78]. Moreover, the efficiency of RPT is largely based on targeting of carriers, which could be sub-optimal, leading to asymmetrical delivery of IR [79]. Thus, the efficacy of RPT relies on the efficiency of local energy deposition.

Alpha particle therapy

The aspect of internal irradiation in PRT provided the possibility to use radionuclides that emit high energy radiation that are not suitable for external irradiation, since such radioactivity does not penetrate the skin. In this thesis, we focus on the type of radiation, which is currently investigated intensively and shows preliminary therapeutic potential: alpha particle (α-particle) irradiation [80].

An α-particle consist of two protons and two neutrons, similar as the helium nucleus, and are emitted from certain radionuclides during their radioactive decay. Unlike photons or electrons, α-particles traverse only up to 100 µm in tissue, largely dependent on their emission energy

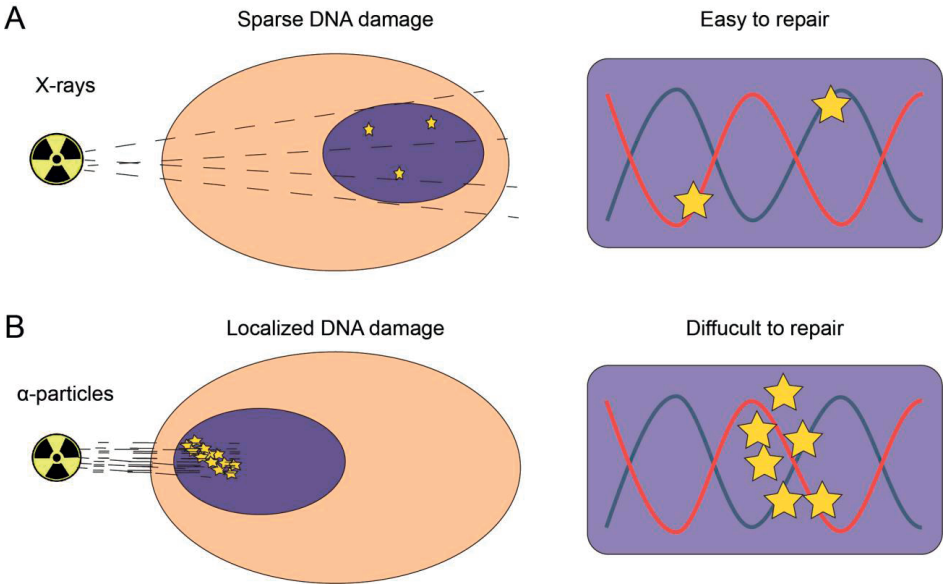

Figure 5. Schematic visualization of DNA damage induction by X-ray or α-particle irradiation. *(A) Low-LET X-ray irradiation inflicts few ionizations to the material it passes and therefore only sparse DNA damage. Generally, the inflicted DNA damage is easy to repair by several DNA damage repair pathways. (B) High-LET α-particle irradiation has a very dense ionization pattern, which inflicts highly condensed DNA damage. Such clustered DNA damage is considered highly complex and requires more specialized DNA repair pathways making this type of DNA damage more difficult to repair.*

(Figure 5B) [81]. Such short range is beneficial in a therapeutic setting as α-particles will less likely reach healthy tissue surrounding the target tumor. However, off-target binding and clearance still cause toxicity to other health organs. For example, most RPT molecules are extruded via the kidneys causing irradiation deposition and thereby renal toxicity.

One of the reasons of the characteristic short path length of α-particles is the high-LET, which is estimated to be 50 - 200 times higher compared to X-rays [82]. Radiation with such high-energy deposition is thought to inflict much more complex DNA damage compared to, for example, X-rays. In addition, the energy deposition of α-particles is highly localized and is thought to induce clustered DNA damage, which requires more complex DNA damage repair pathways [81, 83]. These observations show that the biological effect of α-particle irradiation is much higher compared to X-rays, resulting in a high RBE (up to 20 times) and greater treatment value.

Encapsulating α-particle emitting radionuclides

Although α-particle based PRT has large therapeutic potential, the use of α-particle irradiation comes with an additional challenge: recoiling daughter radionuclides [84]. During recoiling events, high-energy radionuclides break apart from the delivery vehicle and are free to roam in the body, possibly inflicting harm to surrounding tissue (Figure 6). Retaining the recoiling daughter radionuclides has seen much interest in the chemistry field, searching for solutions to this problem [85]. Liposomes have shown some potential in retaining mother radionuclides (up to 98%) but not recoiled daughter radionuclides, which was less than 20% [86]. In this thesis we focus on nano-carriers composed of polymers, which are more robust and therefore have more potential in retaining daughter radionuclides [87, 88].

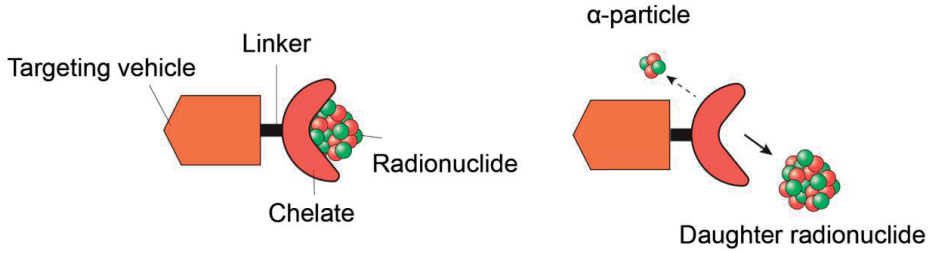

Figure 6. Recoiling daughter nuclides. *During radioactive decay, the remaining nuclide is often referred to as the daughter nuclide. In Radiopharmaceutical Therapy, the radionuclide is attached to the targeted vehicle using a chelator, which ensures efficient and strong binding of the radionuclide. However, during alpha decay, the daughter radionuclide experiences high recoiling energy, which ruptures the binding to the chelator. Therefore, with the use of long-lived α-particle emitting radionuclides comes a higher chance of setting their daughter radionuclides free from their carrier [85].*

Polymersomes

Polymersomes (PMs) are nano-carriers formed from amphiphilic block copolymers. Block copolymers undergo self-assembly when the concentration exceeds the critical aggregate concentration [89]. Most PMs are mode from block copolymers that consist of a hydrophobic part (mainly poly(styrene) and poly (ethyl ethylene)) and a hydrophilic part which mainly consist of poly(ethylene glycol) also known as PEG [90]. The consequence of using both hydrophilic and hydrophobic parts to prepare PMs is an aqueous core that is surrounded by a hydrophobic bilayer (Figure 7A).

By using different assembly techniques or extruding the PMs through polycarbonate filters, the size of PMs can be altered. Adjustments to PM sizes can be dependent on the application. For example, circulation times of PMs below 200 nm in diameter are drastically longer compared to larger PMs due to mechanical filtration in the spleen [90]. In addition, the lenght of the PEG-chain, is reported to affect circulation time, tumor uptake and clearance pathways.

For PMs to be of use in the field of PRT, radionuclides have to be encapsulated or labeled to the surface of PMs. Pentetic acid (DTPA) is often used to chelate radionuclides for application in bio distributions. By attaching DTPA to the hydrophilic outer layer, surface labeling of PMs can be achieved. However, this approach showed to be not very effective for PRT, as labeling efficiency was high but unstable [91]. In contrast, encapsulating radionuclides within PMs showed more promising results.

By encapsulating DTPA in the process of PM preparation, radionuclides can be trapped in the aqueous core, retaining more than 95% of the radionuclide after 24h (Figure 7B) [92]. The first reports of encapsulation of radionuclides in PMs were mainly performed using indium-111 [88, 91-93]. Further research explored the encapsulation of therapeutic radionuclides, mainly focusing on a-particle emitters actinium-225 and bismuth-213 [94-96].

Encapsulating high-energy α-particle emitting radionuclides in PMs has shown great potential of retaining the recoiling daughter radionuclides. Adding $InPO_4$ or $LaPO_4$ nanoparticles to PMs increased the recoil retention up to 20% and 28%, respectively [95]. In addition, Monte Carlo simulations show that adding high atomic number material to the PMs design, such as iron (Fe), improves recoil retention drastically (59.3%) [97].

These characteristics and improvements of PMs seem very promising for therapeutic use. However, aspects such as, circulation time, toxicity, and uptake have been lacking or are completely absent regarding PMs. Before PMs could be therapeutically viable, not only the chemical advantages should be investigated, but also the biological consequence of injecting PMs systemically.

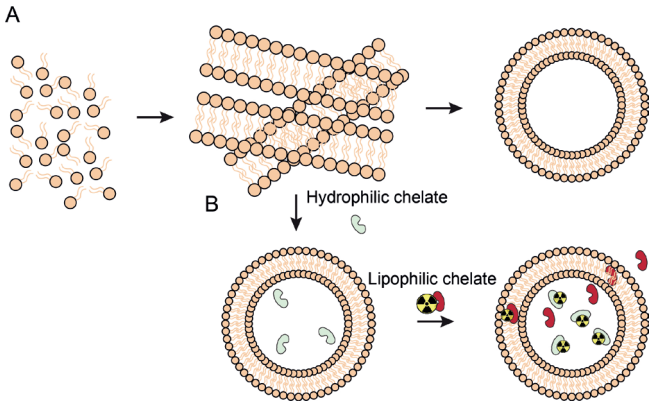

Figure 7. Preparation and radioactive labeling of Polymersomes. *(A) Schematic visualization of the self-assembly of block-copolymers, eventually forming bi-layered Polymersomes (PMs). The self-assembled PMs consist of an aqueous core surrounded by a hydrophobic bi-layer. (B) During the self-assembly is it possible to add hydrophilic chelates to the mixture, leading to the addition of a chelate in the core and therefore the ability to label the PMs with radionuclides. PMs are radiolabeled by adding radionuclides bound to lipophilic chelates, which can pass the hydrophobic bilayer, transporting the radionuclides to the core. In the PM core, the radionuclides are transported to the hydrophilic chelate, which is unable to escape through the bilayer resulting in a radiolabeled PM. The leftover lipophilic chelate is washed out ensuring only encapsulated radionuclides in the mixture.*

Scope of this thesis

Although EBRT has been applied for many decades as anti-tumor therapy, it has not been effective against metastasized cancer. RPT has shown to be a successful addition to the treatment options, targeting specific molecular targets and low energy radionuclides. However, complete cure of metastasized disease is seldom reached, due to insensitivity of tumor tissue and the induction of adverse side effects after therapy. These observations call for treatment optimization, searching for viable combination therapies and other irradiation strategies, inflicting more DNA damage whilst limiting side effects.

In this thesis project we therefore analyzed; (1) the effect of eliminating NHEJ, HR or both on IR protection, (2) a methodology for external α-particle irradiation, (3) DSB processing after high- or low-LET irradiation and (4) intracellular uptake processing of PMs used for local delivery of α-particles.

Chapter 1 describes the mechanisms of DNA damage repair together with how radioactivity is used in the clinic and which nano-carries would be suited best, to carry high-energy radionuclides.

In **Chapter 2**, we aim to understand how HR and NHEJ cooperate in IR protection. By exposing mutant adult mice and their embryonic stem cells or fibroblasts to IR we investigate the consequence of HR or NHEJ deficiency. Using mRNA expression profiling, effects of the introduced mutations were analyzed in endogenous conditions. Finally, the cell biological consequence of eliminating NHEJ or HR was examined by confocal and super resolution microscopy using 53BP1 kinetics.

In **Chapter 3**, we describe a method to address the lack of affordable and easily accessible external α-particle irradiation systems. This chapter presents a detailed approach on the development of an easy to use novel irradiation set-up for cell biological experiments to study the impact of α-particles.

We applied the developed irradiation system in **Chapter 4** to compare the DSB processing in living cells after high- or low-LET irradiation. This chapter describes a detailed analysis method to track DSB formation and processing in living cells. By comparing high- and low-LET irradiation, we aimed to quantify differences in DSB processing using live-cell, confocal and super-resolution imaging.

Polymersomes are nano-cariers, which have a high potential to be applied in targeted radionuclidetherapy using α-particle emitters. In **Chapter 5**, we investigated the effect of PM size on uptake in different cell types. In addition, we analyze geometrical distribution and post-uptake processing of PM using co-localization studies. Furthermore, we show DNA damage induction of radiolabeled PMs.

REFERENCES

1. Jackson, S.P. and J. Bartek, *The DNA-damage response in human biology and disease.* Nature, 2009. **461**(7267): p. 1071-8.
2. Williams, G.J., S.P. Lees-Miller, and J.A. Tainer, *Mre11-Rad50-Nbs1 conformations and the control of sensing, signaling, and effector responses at DNA double-strand breaks.* DNA Repair (Amst), 2010. **9**(12): p. 1299-306.
3. Lafrance-Vanasse, J., G.J. Williams, and J.A. Tainer, *Envisioning the dynamics and flexibility of Mre11-Rad50-Nbs1 complex to decipher its roles in DNA replication and repair.* Prog Biophys Mol Biol, 2015. **117**(2-3): p. 182-193.
4. Syed, A. and J.A. Tainer, *The MRE11-RAD50-NBS1 Complex Conducts the Orchestration of Damage Signaling and Outcomes to Stress in DNA Replication and Repair.* Annu Rev Biochem, 2018. **87**: p. 263-294.
5. You, Z., et al., *ATM activation and its recruitment to damaged DNA require binding to the C terminus of Nbs1.* Mol Cell Biol, 2005. **25**(13): p. 5363-79.
6. Bakkenist, C.J. and M.B. Kastan, *DNA damage activates ATM through intermolecular autophosphorylation and dimer dissociation.* Nature, 2003. **421**(6922): p. 499-506.
7. Rogakou, E.P., et al., *DNA double-stranded breaks induce histone H2AX phosphorylation on serine 139.* J Biol Chem, 1998. **273**(10): p. 5858-68.
8. Melander, F., et al., *Phosphorylation of SDT repeats in the MDC1 N terminus triggers retention of NBS1 at the DNA damage-modified chromatin.* Journal of Cell Biology, 2008. **181**(2): p. 213-226.
9. Stucki, M., et al., *MDC1 directly binds phosphorylated histone H2AX to regulate cellular responses to DNA double-strand breaks.* Cell, 2005. **123**(7): p. 1213-26.
10. Lou, Z., et al., *MDC1 maintains genomic stability by participating in the amplification of ATM-dependent DNA damage signals.* Mol Cell, 2006. **21**(2): p. 187-200.
11. Mailand, N., et al., *RNF8 ubiquitylates histones at DNA double-strand breaks and promotes assembly of repair proteins.* Cell, 2007. **131**(5): p. 887-900.
12. Huen, M.S., et al., *RNF8 transduces the DNA-damage signal via histone ubiquitylation and checkpoint protein assembly.* Cell, 2007. **131**(5): p. 901-14.
13. Zhou, T., et al., *The Functions of DNA Damage Factor RNF8 in the Pathogenesis and Progression of Cancer.* Int J Biol Sci, 2019. **15**(5): p. 909-918.
14. Mattiroli, F., et al., *RNF168 ubiquitinates K13-15 on H2A/H2AX to drive DNA damage signaling.* Cell, 2012. **150**(6): p. 1182-95.
15. Fradet-Turcotte, A., et al., *53BP1 is a reader of the DNA-damage-induced H2A Lys 15 ubiquitin mark.* Nature, 2013. **499**(7456): p. 50-+.
16. Botuyan, M.V., et al., *Structural basis for the methylation state-specific recognition of histone H4-K20 by 53BP1 and Crb2 in DNA repair.* Cell, 2006. **127**(7): p. 1361-73.
17. Tong, Q., et al., *Structural plasticity of methyllysine recognition by the tandem tudor domain of 53BP1.* Structure, 2015. **23**(2): p. 312-21.
18. Hable, V., et al., *Recruitment Kinetics of DNA Repair Proteins Mdc1 and Rad52 but Not 53BP1 Depend on Damage Complexity.* Plos One, 2012. **7**(7).
19. Adams, M.M. and P.B. Carpenter, *Tying the loose ends together in DNA double strand break repair with 53BP1.* Cell Division, 2006. **1**.
20. Panier, S. and S.J. Boulton, *Double-strand break repair: 53BP1 comes into focus.* Nature Reviews Molecular Cell Biology, 2014. **15**(1): p. 7-18.

21. Jowsey, P., et al., *Characterisation of the sites of DNA damage-induced 53BP1 phosphorylation catalysed by ATM and ATR.* DNA Repair, 2007. **6**(10): p. 1536-1544.
22. Munoz, I.M., et al., *Phospho-epitope binding by the BRCT domains of hPTIP controls multiple aspects of the cellular response to DNA damage.* Nucleic Acids Research, 2007. **35**(16): p. 5312-5322.
23. Ward, I.M., et al., *Accumulation of checkpoint protein 53BP1 at DNA breaks involves its binding to phosphorylated histone H2AX.* Journal of Biological Chemistry, 2003. **278**(22): p. 19579-19582.
24. Tippin, B., et al., *To slip or skip, visualizing frameshift mutation dynamics for error-prone DNA polymerases.* J Biol Chem, 2004. **279**(44): p. 45360-8.
25. Gottlieb, T.M. and S.P. Jackson, *The DNA-Dependent Protein-Kinase - Requirement for DNA Ends and Association with Ku Antigen.* Cell, 1993. **72**(1): p. 131-142.
26. Ciccia, A. and S.J. Elledge, *The DNA Damage Response: Making It Safe to Play with Knives.* Molecular Cell, 2010. **40**: p. 179-204.
27. Lieber, M.R., *The mechanism of double-strand DNA break repair by the nonhomologous DNA end-joining pathway.* Annu Rev Biochem, 2010. **79**: p. 181-211.
28. Yannone, S.M., et al., *Coordinate 5' and 3' endonucleolytic trimming of terminally blocked blunt DNA double-strand break ends by Artemis nuclease and DNA-dependent protein kinase.* Nucleic Acids Res, 2008. **36**(10): p. 3354-65.
29. Ahnesorg, P., P. Smith, and S.P. Jackson, *XLF interacts with the XRCC4-DNA ligase IV complex to promote DNA nonhomologous end-joining.* Cell, 2006. **124**(2): p. 301-13.
30. Wyman, C. and R. Kanaar, *DNA Double-Strand Break Repair: All's Well that Ends Well.* Annual Review of Genetics, 2006. **40**: p. 363-383.
31. Reczek, C.R., et al., *The interaction between CtIP and BRCA1 is not essential for resection-mediated DNA repair or tumor suppression.* Journal of Cell Biology, 2013. **201**(5): p. 693-707.
32. Sartori, A.A., et al., *Human CtIP promotes DNA end resection.* Nature, 2007. **450**(7169): p. 509-U6.
33. Nimonkar, A.V., et al., *BLM-DNA2-RPA-MRN and EXO1-BLM-RPA-MRN constitute two DNA end resection machineries for human DNA break repair.* Genes & Development, 2011. **25**(4): p. 350-362.
34. Tomimatsu, N., et al., *Exo1 plays a major role in DNA end resection in humans and influences double-strand break repair and damage signaling decisions.* DNA Repair (Amst), 2012. **11**(4): p. 441-8.
35. Chen, H., M. Lisby, and L.S. Symington, *RPA coordinates DNA end resection and prevents formation of DNA hairpins.* Mol Cell, 2013. **50**(4): p. 589-600.
36. Jasin, M. and R. Rothstein, *Repair of strand breaks by homologous recombination.* Cold Spring Harbor Perspectives in Biology, 2013. **5**: p. a012740.
37. Zhang, F., et al., *PALB2 links BRCA1 and BRCA2 in the DNA-damage response.* Curr Biol, 2009. **19**(6): p. 524-9.
38. Liu, J., et al., *Human BRCA2 protein promotes RAD51 filament formation on RPA-covered single-stranded DNA.* Nat Struct Mol Biol, 2010. **17**(10): p. 1260-2.
39. Heyer, W.D., et al., *Rad54: the Swiss Army knife of homologous recombination?* Nucleic Acids Res, 2006. **34**(15): p. 4115-25.
40. Mazin, A.V., A.A. Alexeev, and S.C. Kowalczykowski, *A novel function of Rad54 protein. Stabilization of the Rad51 nucleoprotein filament.* J Biol Chem, 2003. **278**(16): p. 14029-36.
41. Petukhova, G., et al., *Yeast Rad54 promotes Rad51-dependent homologous DNA pairing via ATP hydrolysis-driven change in DNA double helix conformation.* J Biol Chem, 1999. **274**(41): p. 29453-62.
42. Solinger, J.A., K. Kiianitsa, and W.D. Heyer, *Rad54, a Swi2/Snf2-like recombinational repair protein, disassembles Rad51:dsDNA filaments.* Mol Cell, 2002. **10**(5): p. 1175-88.

43. Bianco, P.R., R.B. Tracy, and S.C. Kowalczykowski, *DNA strand exchange proteins: a biochemical and physical comparison.* Front Biosci, 1998. **3**: p. D570-603.
44. Li, J., D.L. Holzschu, and T. Sugiyama, *PCNA is efficiently loaded on the DNA recombination intermediate to modulate polymerase delta, eta, and zeta activities.* Proceedings of the National Academy of Sciences of the United States of America, 2013. **110**(19): p. 7672-7677.
45. van Schendel, R., et al., *Genomic Scars Generated by Polymerase Theta Reveal the Versatile Mechanism of Alternative End-Joining.* PLoS Genet, 2016. **12**(10): p. e1006368.
46. Zhang, Y. and M. Jasin, *An essential role for CtIP in chromosomal translocation formation through an alternative end-joining pathway.* Nat Struct Mol Biol, 2011. **18**(1): p. 80-4.
47. Truong, L.N., et al., *Microhomology-mediated End Joining and Homologous Recombination share the initial end resection step to repair DNA double-strand breaks in mammalian cells.* Proc Natl Acad Sci U S A, 2013. **110**(19): p. 7720-5.
48. Saito, S., R. Maeda, and N. Adachi, *Dual loss of human POLQ and LIG4 abolishes random integration.* Nat Commun, 2017. **8**: p. 16112.
49. Zelensky, A.N., et al., *Inactivation of Pol theta and C-NHEJ eliminates off-target integration of exogenous DNA.* Nat Commun, 2017. **8**(1): p. 66.
50. Kelso, A.A., et al., *Distinct roles of RAD52 and POLQ in chromosomal break repair and replication stress response.* PLoS Genet, 2019. **15**(8): p. e1008319.
51. Motycka, T.A., et al., *Physical and functional interaction between the XPF/ERCC1 endonuclease and hRad52.* Journal of Biological Chemistry, 2004. **279**(14): p. 13634-13639.
52. Bhargava, R., D.O. Onyango, and J.M. Stark, *Regulation of Single-Strand Annealing and its Role in Genome Maintenance.* Trends Genet, 2016. **32**(9): p. 566-575.
53. Kakarougkas, A. and P.A. Jeggo, *DNA DSB repair pathway choice: an orchestrated handover mechanism.* Br J Radiol, 2014. **87**(1035): p. 20130685.
54. Zhao, B., et al., *The molecular basis and disease relevance of non-homologous DNA end joining.* Nat Rev Mol Cell Biol, 2020.
55. Williams, R.S., et al., *Mre11 Dimers Coordinate DNA End Bridging and Nuclease Processing in Double-Strand-Break Repair.* Cell, 2008. **135**: p. 97-109.
56. Sartori, A.A., et al., *Human CtIP promotes DNA end resection.* Nature, 2007. **450**: p. 509-14.
57. Silverman, J., et al., *Human Rif1, ortholog of a yeast telomeric protein, is regulated by ATM and 53BP1 and functions in the S-phase checkpoint.* Genes and Development, 2004. **18**: p. 2108-2119.
58. Noordermeer, S.M., et al., *The shieldin complex mediates 53BP1-dependent DNA repair.* Nature, 2018. **560**(7716): p. 117-121.
59. Symington, L.S. and J. Gautier, *Double-Strand Break End Resection and Repair Pathway Choice.* Annual Review of Genetics, 2011. **45**: p. 247-271.
60. Escribano-Díaz, C., et al., *A Cell Cycle-Dependent Regulatory Circuit Composed of 53BP1-RIF1 and BRCA1-CtIP Controls DNA Repair Pathway Choice.* Molecular Cell, 2013. **49**: p. 872-883.
61. Zlotorynski, E., *Shieldin the ends for 53BP1.* Nat Rev Mol Cell Biol, 2018. **19**(6): p. 346-347.
62. Dev, H., et al., *Shieldin complex promotes DNA end-joining and counters homologous recombination in BRCA1-null cells.* Nat Cell Biol, 2018. **20**(8): p. 954-965.
63. Panier, S. and S.J. Boulton, *Double-strand break repair: 53BP1 comes into focus.* Nature Reviews Molecular Cell Biology, 2014. **15**: p. 7-18.
64. Misteli, T. and E. Soutoglou, *The emerging role of nuclear architecture in DNA repair and genome maintenance.* Nat Rev Mol Cell Biol, 2009. **10**(4): p. 243-54.
65. van Veelen, L.R., et al., *Ionizing radiation-induced foci formation of mammalian Rad51 and Rad54 depends on the Rad51 paralogs, but not on Rad52.* Mutat Res, 2005. **574**(1-2): p. 34-49.

66. Polo, S.E. and S.P. Jackson, *Dynamics of DNA damage response proteins at DNA breaks: a focus on protein modifications.* Genes & Development, 2011. **25**(5): p. 409-433.
67. Rothkamm, K., et al., *DNA damage foci: Meaning and significance.* Environ Mol Mutagen, 2015. **56**(6): p. 491-504.
68. Brandsma, I. and D.C. Gent, *Pathway choice in DNA double strand break repair: observations of a balancing act.* Genome Integr, 2012. **3**(1): p. 9.
69. Gianfaldoni, S., et al., *An Overview on Radiotherapy: From Its History to Its Current Applications in Dermatology.* Open Access Maced J Med Sci, 2017. **5**(4): p. 521-525.
70. Ward, J.F., *DNA Damage Produced by Ionizing-Radiation in Mammalian-Cells - Identities, Mechanisms of Formation, and Reparability.* Progress in Nucleic Acid Research and Molecular Biology, 1988. **35**: p. 95-125.
71. *The 2007 Recommendations of the International Commission on Radiological Protection. ICRP publication 103.* Ann ICRP, 2007. **37**(2-4): p. 1-332.
72. Hogle, W.P., *Radiation therapy 101: the basics every nurse needs to know.* Clin J Oncol Nurs, 2003. **7**(2): p. 230-2.
73. Lindahl, T. and D.E. Barnes, *Repair of endogenous DNA damage.* Cold Spring Harb Symp Quant Biol, 2000. **65**: p. 127-33.
74. Chamberlain, M.C. and J.S. Barnholtz-Sloan, *Medical treatment of recurrent meningiomas.* Expert Rev Neurother, 2011. **11**(10): p. 1425-32.
75. Dolgin, E., *Radioactive drugs emerge from the shadows to storm the market.* Nat Biotechnol, 2018. **36**(12): p. 1125-1127.
76. Gill, M.R., et al., *Targeted radionuclide therapy in combined-modality regimens.* Lancet Oncol, 2017. **18**(7): p. e414-e423.
77. Dale, R. and A. Carabe-Fernandez, *The radiobiology of conventional radiotherapy and its application to radionuclide therapy.* Cancer Biother Radiopharm, 2005. **20**(1): p. 47-51.
78. Fowler, J.F., *Radiobiological aspects of low dose rates in radioimmunotherapy.* Int J Radiat Oncol Biol Phys, 1990. **18**(5): p. 1261-9.
79. Sgouros, G., et al., *Radiopharmaceutical therapy in cancer: clinical advances and challenges.* Nat Rev Drug Discov, 2020. **19**(9): p. 589-608.
80. Targeted Alpha Therapy Working, G., et al., *Targeted Alpha Therapy, an Emerging Class of Cancer Agents: A Review.* JAMA Oncol, 2018. **4**(12): p. 1765-1772.
81. Raju, M.R., et al., *RBE and OER of pi-minus mesons for damage to cultured T-1 cells of human kidney origin.* Br J Radiol, 1972. **45**(531): p. 178-81.
82. Franken, N.A., et al., *Cell survival and radiosensitisation: modulation of the linear and quadratic parameters of the LQ model (Review).* Int J Oncol, 2013. **42**(5): p. 1501-15.
83. Franken, N.A., et al., *Comparison of RBE values of high-LET alpha-particles for the induction of DNA-DSBs, chromosome aberrations and cell reproductive death.* Radiat Oncol, 2011. **6**: p. 64.
84. Kozempel, J., O. Mokhodoeva, and M. Vlk, *Progress in Targeted Alpha-Particle Therapy. What We Learned about Recoils Release from In Vivo Generators.* Molecules, 2018. **23**(3).
85. de Kruijff, R.M., H.T. Wolterbeek, and A.G. Denkova, *A Critical Review of Alpha Radionuclide Therapy-How to Deal with Recoiling Daughters?* Pharmaceuticals (Basel), 2015. **8**(2): p. 321-36.
86. Sofou, S., et al., *Engineered liposomes for potential alpha-particle therapy of metastatic cancer.* J Nucl Med, 2004. **45**(2): p. 253-60.
87. Discher, D.E. and A. Eisenberg, *Polymer vesicles.* Science, 2002. **297**(5583): p. 967-73.
88. Thijssen, L., et al., *Polymersomes as nano-carriers to retain harmful recoil nuclides in alpha radionuclide therapy: a feasibility study.* Radiochimica Acta, 2012. **100**(7): p. 473-481.

89. Meng, F.H., Z.Y. Zhong, and J. Feijen, *Stimuli-Responsive Polymersomes for Programmed Drug Delivery.* Biomacromolecules, 2009. **10**(2): p. 197-209.
90. Lee, J.S. and J. Feijen, *Polymersomes for drug delivery: design, formation and characterization.* J Control Release, 2012. **161**(2): p. 473-83.
91. Brinkhuis, R.P., et al., *Size dependent biodistribution and SPECT imaging of (111)In-labeled polymersomes.* Bioconjug Chem, 2012. **23**(5): p. 958-65.
92. Wang, G., et al., *Polymersomes as radionuclide carriers loaded via active ion transport through the hydrophobic bilayer.* Soft Matter, 2013. **9**(3): p. 727-734.
93. Murdoch, C., et al., *Internalization and biodistribution of polymersomes into oral squamous cell carcinoma cells in vitro and in vivo.* Nanomedicine (Lond), 2010. **5**(7): p. 1025-36.
94. de Kruijff, R.M., et al., *The therapeutic potential of polymersomes loaded with (225)Ac evaluated in 2D and 3D in vitro glioma models.* Eur J Pharm Biopharm, 2018. **127**: p. 85-91.
95. de Kruijff, R.M., et al., *Improved (225)Ac daughter retention in InPO4 containing polymersomes.* Appl Radiat Isot, 2017. **128**: p. 183-189.
96. Wang, G., et al., *Retention studies of recoiling daughter nuclides of 225Ac in polymer vesicles.* Appl Radiat Isot, 2014. **85**: p. 45-53.
97. Kruijff, R.M., *Alpha Radionuclide Therapy Using Polymeric Nanocarries: Solution to the Recoil Problem?* Thesis, 2018.

2

Homologous Recombination and Non-Homologous End Joining are Mutually Exclusive in Ionizing Radiation Protection

Stefan J. Roobol[1,2,3], Sigrid Swagemakers[4,5], Yanto Ridwan[1,3], Paula van Heijningen[1], G. van de kamp[1], T. Heemskerk[1], C. Roland Wolf[6], George Garinis[7], Christophe Badie[8], Roland Kanaar[1,2], Dik C. van Gent[1,2] and Jeroen Essers[1,9,10, *]

[1]Department of Molecular Genetics, [2]Oncode Institute, Erasmus University Medical Center, Rotterdam, The Netherlands

[3]Department of Radiology & Nuclear Medicine, Erasmus University Medical Center, Rotterdam, The Netherlands

[4]Department of Pathology, Erasmus University Medical Center, Rotterdam, The Netherlands

[5]Department of Bioinformatics, Erasmus University Medical Center, Rotterdam, The Netherlands

[6]Department of Systems Medicine, School of Medicine, University of Dundee, Ninewells Hospital, Dundee, United Kingdom.

[7]Institute of Molecular Biology and Biotechnology, Foundation for Research and Technology-Hellas, Nikolaou Plastira 100, 70013, Heraklion, Crete, Greece

[8]Cancer Mechanisms and Biomarkers Group, Radiation Effects Department, Centre for Radiation, Chemical and Environmental Hazards, Public Health England, Chilton, Didcot, United Kingdom.

[9]Department of Radiation Oncology, Erasmus University Medical Center, Rotterdam, The Netherlands

[10]Department of Vascular Surgery, Erasmus University Medical Center, Rotterdam, The Netherlands

*Correspondence

Jeroen Essers: j.essers@erasmusmc.nl

Manuscript in preperation

ABSTRACT

Ionizing radiation (IR) induced DNA damage activates many pathways which are crucial to preserve genome integrity. One of the most toxic type of DNA damage is the Double Strand Break (DSB), which can be repaired by at least two different DNA repair pathways, Non-Homologous End Joining (NHEJ) and Homologous Recombination (HR). Here we combined deletion of DNA-PK_{CS}, which has a role in NHEJ, with the disruption of HR gene *RAD54* to investigate the possible interplay of two distinct DSB repair pathways. Disrupting *RAD54* in mice with a *DNA-$PK_{CS}^{-/-}$* background induced synergistic sensitivity to IR. Transcriptome profiling using livers of *DNA-$PK_{CS}^{-/-}$* or *DNA-$PK_{CS}^{-/-}$RAD54$^{-/-}$* mice showed endogenous *CDKN1A* (p21) upregulation. In addition, *DNA-$PK_{CS}^{-/-}$* and *DNA-$PK_{CS}^{-/-}$RAD54$^{-/-}$* mice had increased and sustained p21 expression after IR treatment, compared to WT and *RAD54$^{-/-}$* mice. Moreover, DNA-PK_{CS} deficiency impaired dissolution of 53BP1, a marker for DSBs, in both mouse embryonic stem (mES) cells and mouse embryonic fibroblasts (MEFs). In this report we show evidence of mutually exclusive roles for HR and NHEJ in IR protection, where cell type or genetic background determines the extent of each pathway in which it partakes in DSB repair.

Keywords: Non-homologous end joining, DNA double strand break repair, DNA damage response, Ionizing radiation, Homologous recombination

INTRODUCTION

DNA double strand breaks (DSBs) constitute the most dangerous type of DNA damage induced by ionizing radiation (IR) (1). IR induced DNA damage can cause cell death or chromosomal instability, especially in cells with intrinsic DNA repair defects (2). In response to DNA damage, histones undergo posttranslational modifications including phosphorylation, acetylation, methylation and ubiquitination. Such histone modifications represent a histone code that directs the recruitment of protein involved in DNA damage sensing and repair processes (3,4). A long protein recruitment cascade starts with the recruitment of the E3 ubiquitin-protein ligase RNF8 (5). In turn, RNF8 starts an ubiquitination-cascade leading to RNF168-mediated mono-ubiquitination of lysine (K) 13-15 residues of histones of the H2A family (6). This ubiquitination-code can be recognized by a dimer of p53-binding protein 1 (53BP1) (7). The accumulation of 53BP1 at a lesion protects DNA ends from excessive 5' end-resection, thereby facilitating in DSB repair pathway choice (8). In addition, 53BP1 accumulation can be visualized as nuclear foci and can therefore be used as surrogate marker for DSBs.

All higher eukaryotes have at least two pathways of DSB repair, non-homologous end joining (NHEJ) and homologous recombination (HR). NHEJ operates throughout the cell cycle and is initiated by the Ku70/80 heterodimer, a ring shaped dimer which binds to DNA ends (9,10). Upon binding, DNA-PK_{CS} is recruited and activated by auto phosphorylation. At the final step, Ligase IV (LIG4) ligates processed DNA-ends (11,12). During the S and G2 phases of the cell cycle, HR is active as addition to NHEJ (13,14). The HR pathway starts with 5'-3' resection of the DNA ends, generating 3' single stranded DNA, stabilized by RPA (15,16). Recombination protein RAD51 then replaces RPA and forms a protein filament on the single stranded DNA, which facilitates the search for homology (17). RAD54 is a motor protein that increases the efficiency of homology search (18).

Although RAD54 binds directly to Rad51, its function is not essential and RAD54 mutant mice are viable, fertile and do not show IR sensitivity. Interestingly, in contrast to adult mice, *RAD54*$^{-/-}$ mouse embryos (E3.5) and mouse embryonic stem (mES) cells are IR sensitive (19,20). On the other hand, NHEJ deficient adult *scid* mice show IR sensitivity (20). Interestingly, *scid RAD54*$^{-/-}$ double mutant mice show higher IR sensitivity than the single mutants, a phenomenon which was also observed when deletions of KU80 or Lig4 are combined with the deletion of RAD54 (21,22). These observations led to the conclusion that HR and NHEJ function throughout development, in which HR possibly acts as a backup pathway for NHEJ in adult mice.

To further understand the cooperating role of NHEJ and HR we generated *RAD54*$^{-/-}$, *DNA-PK*$_{CS}^{-/-}$ and *DNA-PK*$_{CS}^{-/-}$*RAD54*$^{-/-}$ mutant mice. We report synergistic IR sensitivity when mice are disrupted in HR in a NHEJ deficient background. In addition, transcriptome analysis showed an elevated p21 stress response in *DNA-PK*$_{CS}^{-/-}$ and *DNA-PK*$_{CS}^{-/-}$*RAD54*$^{-/-}$ mutant mice which was increased and sustained after IR, compared to WT. Finally, we show that disrupting *DNA-PK*$_{CS}$ impairs 53BP1 foci dissolution and size increase in both MEFs and mES cells, while only

RAD54$^{-/-}$ mES cells showed similar phenotypes and *RAD54*$^{-/-}$ MEFs did not. Here we confirm both a primary and backup role for RAD54 in DSB repair in stem cells and differentiated cells, respectively. These results show that the role of either HR and NHEJ is mutually exclusive, depending on cell type or genetic background.

MATERIAL AND METHODS

Mice

All mice were backcrossed at least 8 times against C57/BL6, ensuring identical genetic background except for the mutations in *DNA-PK*$_{CS}$ and *RAD54*. To introduce the p21 reporter, *DNA-PK*$_{CS}^{-/-}$*RAD54*$^{-/-}$ mice were crossed with p21 reporter mice, a kind gift from the lab of Drs. Collin Henderson and Roland Wolf (23). All mice were kept under pathogen free conditions in individually ventilated cages in order to prevent infections.

Cell Culture

All Mouse Embryonic Fibroblast (MEFs), cell lines were cultured in Dulbecco's modified Eagle's medium (DMEM) mixed with Ham's F10 (1:1) supplemented with 1% Penicillin/Streptomycin and 10% Fetal Calf Serum (FCS). All mES cell lines were cultured DMEM in a 1:1 mixture with DMEM conditioned by exposure to a confluent monolayer of buffalo rat liver (BRL) cells in T175 flask, 50 mL FCS, 5 mL nonessential amino acids (Lonza), 200 U/mL penicillin, 200 µg/mL streptomycin, 89 µM β-mercaptoethanol, 1000 U/mL leukemia inhibitory factor. MEFs were incubated at 37 degrees in a water-saturated atmosphere with 5% CO_2 and 3% O_2. mES cells were incubated at 37 degrees in a water saturated atmosphere with 5% CO_2 and 20% O_2.

Irradiation

Mice survival experiments were performed by exposing the mice to 2 or 3 Gy using a 137-Cs source. Irradiation of p21-reporter mice was done using a microCT-imaging device (Quantum FX, Perkin Elmer). Radiation dosages relative to exposure time and magnification were previously determined (24). Irradiation was done with the following settings: 10 µm and 60 µm voxel size with 90 kV, 200 µA, and 3 min of scan time. By scanning the mice twice, the given dose was approximately 2 Gy.

All cells were irradiated using the RS320 (Xstrahl Live Sciences), a self-contained cabinet, with a dose rate of 1.6554 Gy/min (195 keV). Cells were cultured on round glass coverslips (diameter: 24 mm). To ensure a monolayer of mES cells the coverslips were coated with 0.05 mg/mL Laminin (Roche).

Clonogenic survival was performed as described before (19). In short, cells were seeded in the appropriate cell density and incubated for 7 hours. Subsequently, the cells were exposed to

2, 4 or 6 Gy of X-ray irradiation while control samples remained untreated. After 7 days colonies were counted manually.

Proliferation assays were performed based on the Sulforhodamine beta (SRB) assay. MEFs were seeded in 6-well plates (5×10^5 cells / well) and the next day adherent cells irradiated with 2, 4 or 6 Gy X-ray irradiation using the RS320, described above. Cells were trypsinized and seeded in triplicate in 12 well plates (1.5×10^4 cells per well) in 1 mL medium allowed to grow for one to six days. Subsequently, medium was removed and cells were fixed with 1 mL 10% trichloroacetic acid overnight at 4°C. Plates were washed five times with tap water and dried. Then cells were incubated in 500 µl 0.5% SRB in 1% acetic acid for 20 minutes at RT. Plates were washed four times with 1% acetic acid and air-dried. SRB was dissolved in 500 µl 10 mM Tris solution and absorbance was measured at 560 nm using a GloMax®-Multi Detection System (Promega).

Microarray analysis

Standard procedures were used to obtain total RNA (Qiagen) from the liver of 3-months old WT and DNA repair deficient mice. Synthesis of double stranded cDNA and biotin labeled cRNA was performed according to the instructions of the manufacturer (Affymetrix). Fragmented cRNA preparations were hybridized to full mouse genome oligonucleotide arrays (Affymetrix, mouse expression 430 V2.0 arrays), using a hybridization Oven 640 (Affymetrix), washed, and subsequently scanned on a GeneChip Scanner 3000 (Affymetrix). Initial data extraction and normalization within each array was performed by means of the GCOS software (Affymetrix). Data intensities were Log transformed and normalized within and between arrays by means of the quantile normalization method as previously described (25). Two-tailed pair wise analysis of variance was used by means of the Spotfire Decision Site software package 7.2 v10.0 (Spotfire Inc, Mass) to extract the statistically significant data from each of the 4 individual microarrays obtained for each genotype. The criteria for significance were set at $P\leq0.05$ and a positive or negative 1.2-fold change.

Gene Ontology classification and network analysis of all significant gene entries were subjected to GO classification (http://www.geneontology.org). Significant over-representation of GO-classified biological processes was assessed by comparing the number of pertinent genes in a given biological process to the total number of the relevant genes printed on the array for that particular biological process (Fisher exact test, $P\leq0.05$, False detection rate (FDR) ≤0.1) using the publicly accessible software Ease (26). Network analysis was performed through the use of Ingenuity Pathways Analysis, “a web-delivered application that enables biologists to discover, visualize and explore therapeutically relevant networks significant to their experimental results, such as gene expression array data sets (QIAGEN Inc, (27))”.

Quantitative RT-PCR

RT-PCR was performed as described before (28). In short, all reactions were run using the PerfeCTa® MultiPlex qPCR SuperMix (Quanta Biosciences, Inc., Gaithersburg, MD, USA), with primer and probe sets for target genes. Cycling parameters were 2 min at 95°C, then 45 cycles of 10 s at 95°C and 60 s at 60°C. Ct values were normalized to a HPRT1 internal control and converted to transcript quantity using standard curves.

Immunofluorescence

Fixed cells were washed with PBS and permeabilized using Triton buffer (0.1% Triton X-100 in PBS, 2x 10 min). Blocking was done for 30 minutes in PBS+ (0.5% BSA and 0.15% Glycin). Cells were incubated with primary antibody diluted in PBS+ for at least 2 hours at RT and washed with Triton buffer (2x 10 min) and PBS+ (1x short). Subsequently the cells were incubated with the secondary antibody for 1 hour in the dark. Primary antibodies used in this study are: 53BP1 (Novus Biologicals). Secondary antibodies used were conjugated to Alexa488 (Life Technologies).

Microscopy

To capture stained cells, a Leica SP5 confocal microscope was used. For each experiment 5 images were acquired using a 40x objective (NA = 1.25) and the appropriate laser lines and emission filters (DAPI/Atto Azide 390; ex. 405 nm – em. 435-480, Alexa 488; ex. 488 nm – em. 500-550 nm, Alexa 594; ex. 561 nm – em. 570-630 nm). For image analysis, z-projections were made and cell nuclei were analysed for 53BP1 foci number and area using homemade ImageJ scripts. In short, cell nuclei were segmented using the DAPI signal by auto-thresholds. Within the segmented nuclei, segmentation masks were made for individual foci using auto-thresholds and the watershed tool (29). The mean area and number of the segmented foci were measured via the measure option of ImageJ.

RESULTS

DNA-PK$_{CS}$ and RAD54 mutations have synergistic effect on IR sensitivity

To investigate the interplay between HR and NHEJ dependent DSB repair, we chose for an experimental set up in which we could detect possible differences between Wild-Type (WT) mice with deficiencies in non-essential gene involved in NHEJ and HR. DSB repair deficiency was achieved either by deletion of *DNA-PK$_{CS}$* (NHEJ) or *RAD54* (HR). To analyze the consequences of combined NHEJ and HR deficiency, we used mice where both genes were disrupted.

We previously found that while *RAD54*$^{-/-}$ mice were not IR hypersensitive, *DNA-PK* mutant mice (*scid*) which were in addition *RAD54* deficient were hypersensitive to IR compared to single *scid* mice (20). Therefore, we first analyzed the IR sensitivity of single *DNA-PK$_{CS}$*$^{-/-}$ and

double DNA-$PK_{CS}^{-/-}$ $RAD54^{-/-}$ mutant mice. While all *DNA-*$PK_{CS}^{-/-}$ single mutant mice survived a single exposure to 2 Gy, all *DNA-*$PK_{CS}^{-/-}$*RAD54*$^{-/-}$ mice died after irradiation with 2 Gy γ-radiation, within a period of 13 days (Figure 1A). A single exposure to 3 Gy of γ-radiation resulted in earlier death of all *DNA-*$PK_{CS}^{-/-}$*RAD54*$^{-/-}$ mice compared to *DNA-*$PK_{CS}^{-/-}$ mice of which 50% did not survive the treatment after 16 days (Figure 1B).

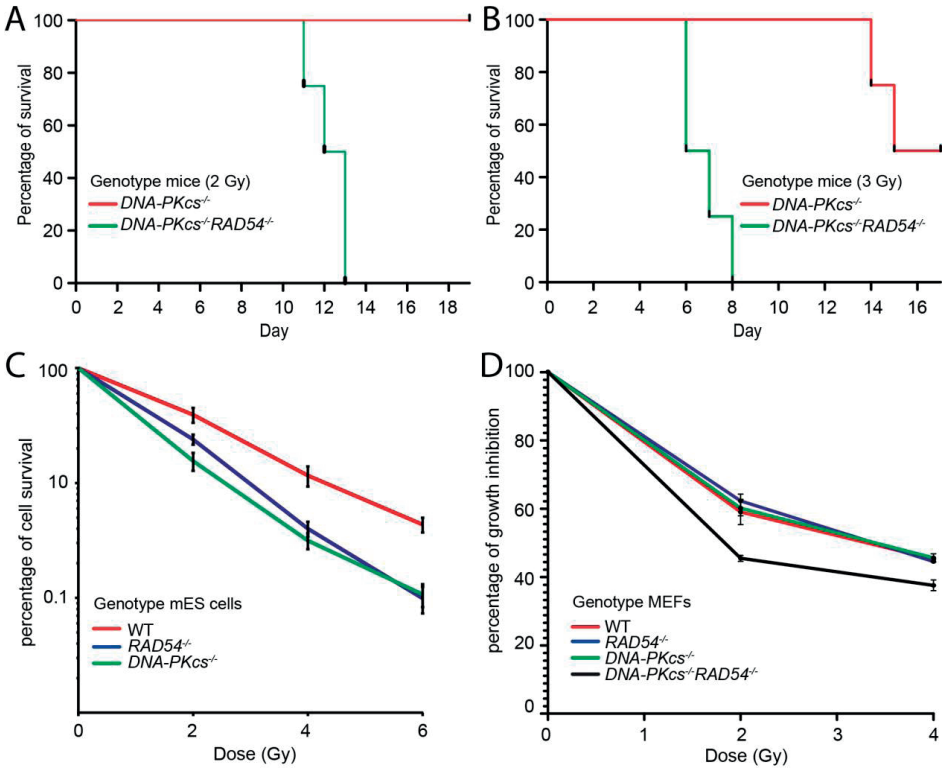

Figure 1. *DNA-*PK_{CS} and *RAD54* mutations have synergistic effect on IR sensitivity in mice.
DNA-$PK_{CS}^{-/-}$ and DNA-$PK_{CS}^{-/-}$RAD54$^{-/-}$ mice were irradiated with 2 **(A)** or 3 **(B)** Gy and tested for survival. The curves represent 5 mice per group. Red and green are represented by indicated genotypes. **(C)** Clonogenic survival of mES cells with indicated genotypes. **(D)** Proliferation assay (SRB) of MEFs with indicated genotypes. Cells were irradiated and grown for 6 days, the SRB assay measures the amount of protein present after 6 days in culture.

To investigate the IR sensitivity of embryonic cells we compared mES cells with either disrupted *RAD54* or *DNA-*PK_{CS}. We observed a 2.5 fold increased IR sensitivity both in *RAD54*$^{-/-}$ and *DNA-*$PK_{CS}^{-/-}$ mES cells compared to WT (Figure 1C). Differentiation of human induced pluripotent or ES cells decreases DNA damage repair by HR (30). We wanted to analyze whether this phenomenon could explain the difference in IR sensitivity between *RAD54* deficient mES cells and *RAD54* deficient adult mice. Using isolated mouse embryonic fibroblasts (MEFs) we performed

proliferation assays to assess the IR sensitivity of differentiated cells deficient in *RAD54*, *DNA-PK$_{CS}$* or both. We found that *DNA-PK$_{CS}^{-/-}$RAD54$^{-/-}$* MEFs show growth inhibition compared to all other genotypes (Figure 1D). IR sensitivity of fibroblasts in this proliferation assay was found in MEFs isolated from *DNA-PK$_{CS}^{-/-}$RAD54$^{-/-}$* adult mice, which showed the highest IR sensitivity in overall survival. We conclude that both HR and NHEJ contribute to IR protection in mES cells. In addition, IR sensitivity of MEFs and adult mice is only observed by deletion of both HR in a NHEJ deficient background, suggesting that HR switches from main DSB repair pathway in mES cells to a back-up role in differentiated cell types.

CDKN1A is upregulated in *DNA-PK$_{CS}$* and *DNA-PK$_{CS}$RAD54* deficient mice

We compared the transcriptional responses in untreated WT and DSB deficient mice to analyze whether and which molecular processes are differentially affected in untreated DSB repair deficient animals. To this end, mRNA expression levels were determined in the liver of three months old WT and DNA repair deficient mice. We selected genes that were significantly differentially expressed between WT and DNA repair deficient mice. We found 589 probe sets, which showed a more than 1.2-fold change in gene expression at a FDR of 0.05, yielding 246 unique probes that were used for further molecular pathways discovery analysis in Ingenuity Pathway Analysis (IPA).

IPA network analysis showed that one of the most extensively affected genetic networks in livers of *DNA-PK$_{CS}^{-/-}$RAD54$^{-/-}$* mice was centered on the *CDKN1A* gene (Figure S1). The *CDKN1A* gene encodes for the p21 protein, a p53-regulated DNA damage response gene (31). Comparing this network to both *DNA-PK$_{CS}^{-/-}$* and *RAD54$^{-/-}$* mice showed upregulation of *CDKN1A* in livers of *DNA-PK$_{CS}^{-/-}$* mice but not in livers of *RAD54$^{-/-}$* mice (Figures S2 and S3). *CDKN1A* was significantly upregulated in *DNA-PK$_{CS}^{-/-}$* and *DNA-PK$_{CS}^{-/-}$RAD54$^{-/-}$* livers, with higher levels of expression in *DNA-PK$_{CS}^{-/-}$RAD54$^{-/-}$* compared to *DNA-PK$_{CS}^{-/-}$* mice (Supplemental table 1). We conclude that inactivation of DNA-PK$_{CS}$ leads to upregulation of p21 in the liver. Although deletion of RAD54 alone did not lead to p21 upregulation in the liver, the deletion of RAD54 in a *DNA-PK$_{CS}^{-/-}$* background did lead to increased upregulation of p21 (Figure 2A).

To confirm these results we performed quantitative reverse transcription PCR (RT-qPCR) cDNA, generated from isolated RNA that was used for previous mRNA expression analysis. We found similar results as the mRNA expression analysis; deletion of DNA-PKcs alone led to upregulation of p21 expression while deleting RAD54 alone did not, unless RAD54 was deleted in a *DNA-PK$_{CS}^{-/-}$* background (Figure 2B). We conclude that the DNA damage response was upregulated in the livers of *DNA-PK$_{CS}^{-/-}$* mice compared to WT and *RAD54$^{-/-}$* mice possibly due to the deficiency in the ability to repair endogenous DNA damage. Even the very low levels of endogenous DSBs in unirradiated conditions are sufficient to activate the p21 response, suggesting that this may be a highly sensitive marker for DNA damage.

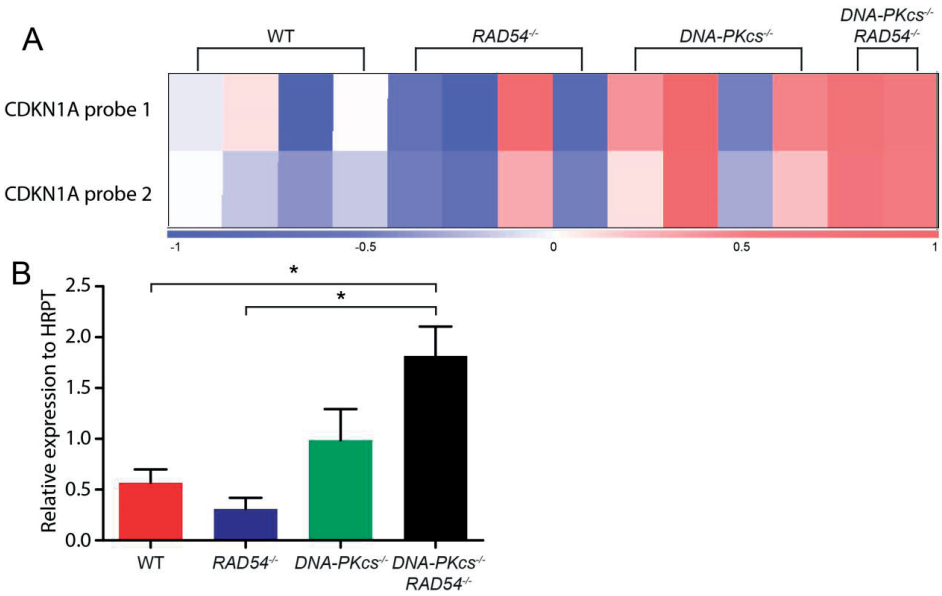

Figure 2. ***CDKN1A* is upregulated in *DNA-PK$_{cs}$* and *DNA-PK$_{cs}$RAD54* deficient mice. (A)** OmniViz heatmap showing the differential expression of CDKN1A, measured with two different probes, between indicated genotypes in untreated mice livers. Gene expression levels: red, upregulated genes compared to the geometric mean; blue, downregulated genes compared to the geometric mean. Color intensity correlated with the degree of change. **(B)** Quantitative RT-PCR analysis of gene expression in untreated mice livers of indicated genotypes. Values were normalized using *HPRT* as standard. The mean values represent at least three mice of similar genotypes (error bars express the SE).

CDKN1A expression as readout for IR sensitivity in DNA repair mutant mice

Since we found expression of the *CDKN1A* gene upregulated in DSB DNA repair deficient mice, we subsequently wanted to evaluate *CDKN1A* expression levels *in vivo* in mice of various repair deficient backgrounds using *CDKN1A*-luciferase reporter mice (23). The reporter construct was directed to the end of exon 3 of the endogenous p21 locus where a sequence, which encodes for T2A-β-gal-T2A-luciferase, was inserted. This insertion led expression of p21, β-gal and luciferase from the one engineered allele. DSB DNA repair deficient mice were crossed with *CDKN1A*-luciferase reporter mice, which led to both hetero- and homozygous animals for the reporter loci. For further experiments, we selected DSB DNA repair animals that were homozygous for the p21 reporter loci. As a control for background luminescence, we used WT mice without any reporter loci, which showed no bioluminescent signal upon injection of luciferin. Consistent with the previous finding, we observed increased endogenous p21-luciferase expression in both untreated *DNA-PK$_{cs}^{-/-}$* and *DNA-PK$_{cs}^{-/-}$RAD54$^{-/-}$* mice compared to WT and *RAD54$^{-/-}$* mice (Figure 3A).

It has been shown that exposing p21-reporter mice to different doses of IR, *in vivo* DNA damage induction can be monitored, non-invasively and dose-dependent, using luciferase as marker

for p21 expression (23). To evaluate DNA damage induced by IR, DNA DSB repair deficient mice expressing the p21-reporter construct were irradiated with a single dose of 2 Gy. For both wild type and *RAD54*$^{-/-}$ mutant mice, the p21 expression increased within 4 hours after irradiation and returned to background levels 24 hours after irradiation (Figure 3A). Interestingly, for both *DNA-PK*$_{CS}$$^{-/-}$ and *DNA-PK*$_{CS}$$^{-/-}$*RAD54*$^{-/-}$ mutant mice the p21 expression was higher at 4 hours after irradiation, compared to WT and *RAD54*$^{-/-}$. In addition, p21 expression did not decline after 24 hours in *DNA-PK*$_{CS}$$^{-/-}$ and *DNA-PK*$_{CS}$$^{-/-}$*RAD54*$^{-/-}$ mutant mice.

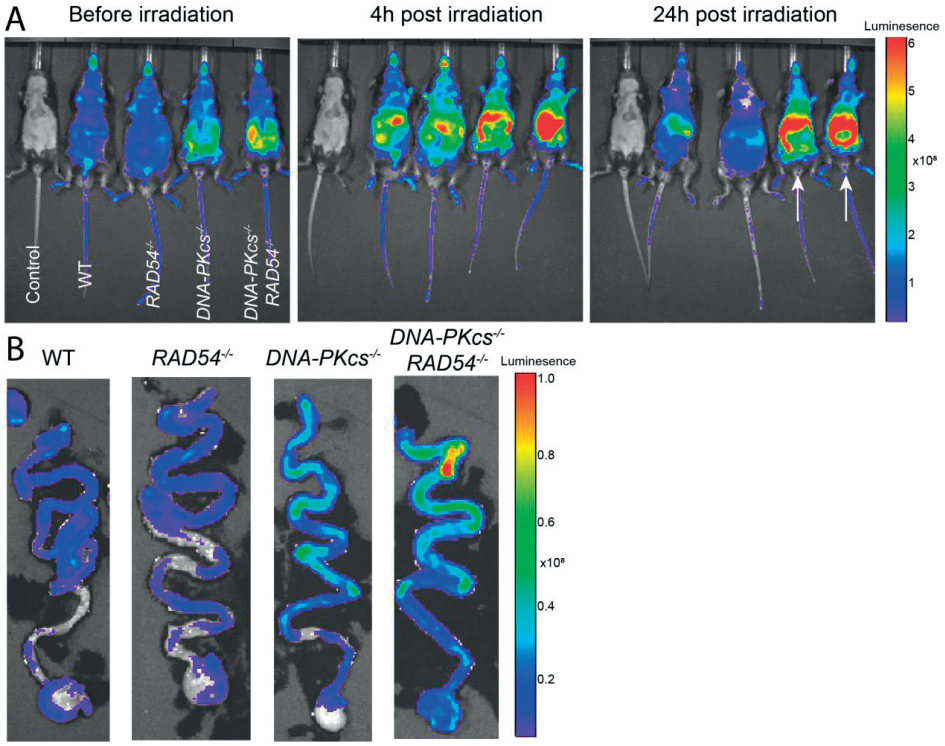

Figure 3. *CDKN1A* expression as readout for radio sensitivity in DNA repair mutant mice.
Bioluminescent imaging of p21-reporter mice crossed with indicated genotypes. **(A)** Mice were irradiated using µCT imaging and were imaged for bioluminescent signal before irradiation, 4 hours post irradiation, and 24 hours post irradiation. Genotype order was the same for every time-point. **(B)** Ex-vivo images of the small intestine 24 hours after irradiation.

Tissue absorbance of bioluminescent signal is a limiting factor for deep-tissue imaging using this technique. Therefore, the observed bioluminescent signal probably originates from organs directly under the skin, such as the intestinal tract. Indeed, ex vivo scanning showed high luciferase expression in *DNA-PK*$_{CS}$$^{-/-}$ and *DNA-PK*$_{CS}$$^{-/-}$*RAD54*$^{-/-}$ mutant intestinal tracts after 24 hours, similar as the whole body scans (Figure 3B). We conclude that mice lacking DNA-PK$_{CS}$ or RAD54 and DNA-PK$_{CS}$ show increased expression of p21 in untreated conditions and sustained expres-

sion after IR, consistent with our previous finding of p21 upregulation in livers of *DNA-PK$_{CS}^{-/-}$* and *DNA-PK$_{CS}^{-/-}$RAD54$^{-/-}$* mice. In addition, p21 expression in *DNA-PK$_{CS}^{-/-}$* and *DNA-PK$_{CS}^{-/-}$RAD54$^{-/-}$* mice is high in the intestinal tract and does not decline after 24 hours, probably due to residual DNA damage.

Impaired 53BP1 foci disappearance in MEFs cells lacking *DNA-PK$_{CS}$*

The upregulated and sustained p21-mediated stress response in *DNA-PK$_{CS}^{-/-}$ and DNA-PK$_{CS}^{-/-}$ RAD54$^{-/-}$* mice is most likely directly related to the IR sensitivity and the hypersensitivity of the respective genotypes. We speculated that the DNA might contain increased levels of spontaneous or residual DSBs. In order to investigate this directly, we analyzed MEFs of the four genotypes and for three genotypes of mES cells, for their endogenous 53BP1 foci and IR induced foci.

MEFs were analyzed for the number of 53BP1 foci in untreated conditions and 2, 6, 18, 30, and 72 hours after IR. We observed that the number of 53BP1 foci increased after IR and decreased over time in both WT and *RAD54$^{-/-}$* cells. Interestingly, the number of 53BP1 foci decreased much more slowly in MEFs lacking DNA-PK$_{CS}$ than WT and *RAD54$^{-/-}$* MEFs (Figure 4A).

In order to quantify the number of foci, we used automated ImageJ scripts to process confocal images and analyze 53BP1 foci per μm^2 of the nucleus. We found no significant differences in the endogenous number of 53BP1 foci between the four genotypes. Treatment with IR increased the number of 53BP1 foci in WT and *RAD54$^{-/-}$* MEFs, which after 72 hours reached similar number of 53BP1 foci as the endogenous condition. However, the course of IR induced number of 53BP1 foci was drastically different when DNA-PK$_{CS}$ was disrupted (Figure 5A). In both *DNA-PK$_{CS}^{-/-}$* and *DNA-PK$_{CS}^{-/-}$RAD54$^{-/-}$* MEFs, the IR induced number of 53BP1 foci was significantly higher compared to other genotypes. In addition, in *DNA-PK$_{CS}^{-/-}$* and *DNA-PK$_{CS}^{-/-}$ RAD54$^{-/-}$* MEFs the number of 53BP1 foci did not decrease to their respective endogenous levels after 72 hours. These results correlate with the observation of the sustained p21 expression after IR in both *DNA-PK$_{CS}^{-/-}$* and *DNA-PK$_{CS}^{-/-}$RAD54$^{-/-}$* adult mice.

In addition, mES cells were analyzed for the number of 53BP1 foci in untreated conditions and 2, 6, 8, 18 and 24 hours after IR. We observed that the number of 53BP1 foci increased after IR and decreased over time in WT cells. Interestingly, the number of 53BP1 foci decreased with slower kinetics in mES cells lacking RAD54 or DNA-PK$_{CS}$ than in WT cells (Figure 4B).

Again, the number of 53BP1 foci was quantitatively analyzed per μm^2 of the nucleus. Similar as the MEFs, we found no significant difference in the endogenous number of 53BP1 foci for all three genotypes. IR treatment of WT mES cells showed an increase in the number of 53BP1 foci, which returned to similar numbers as untreated conditions after 24 hours (Figure 5B). *DNA-PK$_{CS}^{-/-}$* mES cells showed less initial 53BP1 foci after IR compared to both WT and *RAD54$^{-/-}$* mES cells. *RAD54$^{-/-}$* mES cells also show a delayed reduction of 53BP1 foci, compared to WT cells. We conclude that both DNA-PK$_{CS}$ and RAD54 have a role in the reducing the number of 53BP1

foci in mES cells, while DNA-PK$_{CS}$ showed to have this role in MEFs and not RAD54. In addition, as deduced from 53BP1 foci kinetics in mES cells, RAD54 deficiency alone already affected DSB repair, which correlates with the suggestion of a larger role of HR in undifferentiated cells (30).

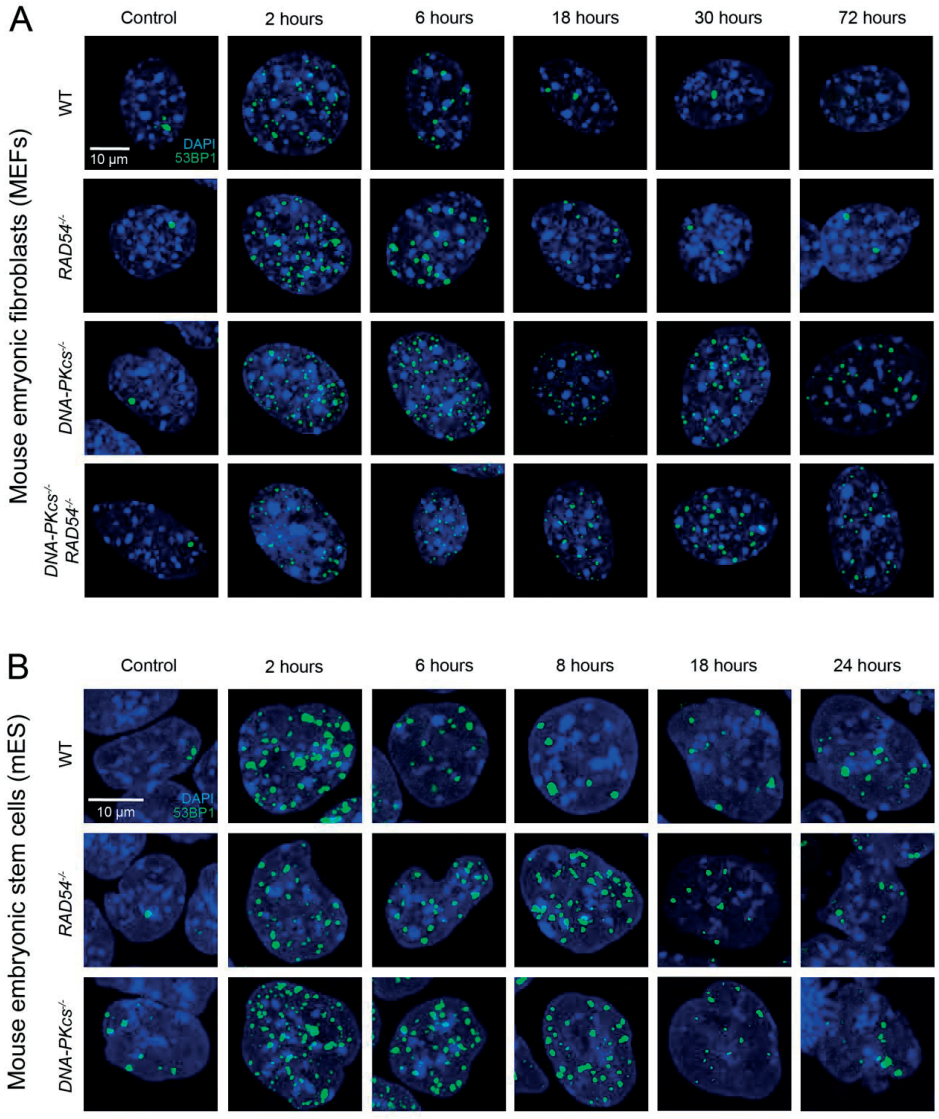

Figure 4. Overview of MEFs and mES cells 53BP1 foci disappearance over time.
MEFs and mES were irradiated with 2 Gy X-ray irradiation and incubated to recover for indicated time. Cells were stained for endogenous 53BP1 (green) and DAPI (blue). Scale bar indicates 10 µm.

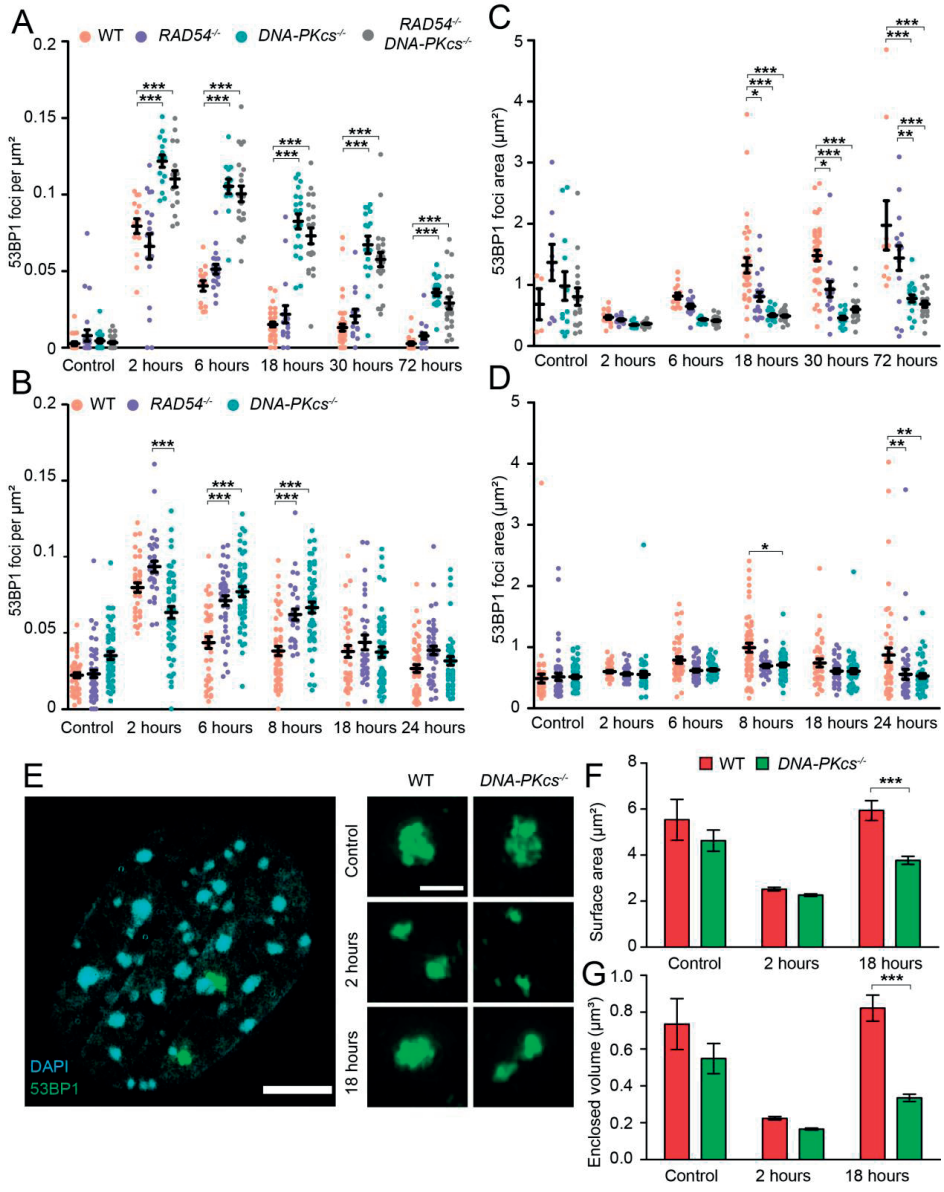

Figure 5. Impaired 53BP1 foci disappearance in MEFs and mES cells deficient for *DNA-PK$_{cs}$*.
Quantification of 53BP1 foci per µm^2 MEF nuclei (A) and average 53BP1 focus size (C). Quantification of 53BP foci per µm^2 mES nuclei (B) and average 53BP1 focus size (D). Per assay >50 nuclei were analyzed. Error bars indicate SEM. (E) SIM image of a WT MEF stained for 53BP1 (green) and DAPI (blue), including representative images of 53BP1 foci in WT and DNA-PK$_{CS}^{-/-}$ MEFs at control conditions, 2 and 18 hours after irradiation. Scale bars represent 5 µm on the left and 0.5 µm on the right. (F) Quantification of the surface area of 53BP1 in 3D. (G) Quantification of the enclosed volume of 53BP1 in 3D. For the quantification >100 53BP1 foci were analyzed. Error bars indicate SEM.

53BP1 foci growth is delayed or absent in DNA repair deficient MEFs and mES cells

Whilst investigating foci disappearance, we noticed that the size of 53BP1 foci was increased at later time points and was different between genotypes (Figure 4A and B). We used automated ImageJ scripts to process confocal images and quantitatively analyzed differences in 53BP1 foci size (μm^2) at the same time points as we analyzed the number of 53BP1 foci. In MEFs, the size of 53BP1 foci in unirradiated conditions showed no significant difference between the genotypes. Interestingly, IR decreased the size of 53BP1 foci for all genotypes, following by an increase over time which was only observed in WT and, to a lesser extent, in *RAD54*$^{-/-}$ MEFs (Figure 5C). MEFs lacking DNA-PK$_{CS}$ did not show any significant increase of 53BP1 foci size up to 72 hours.

Presented confocal images were analyzed by using maximal projections, not harboring possible information in the z-direction. Structured Illumination Microscopy (SIM) is a super-resolution technique which has a higher resolution. By comparing 3D structures of 53BP1 foci in WT and *DNA-PK$_{CS}$*$^{-/-}$ MEFs we observed decrease of size after IR and the absence of size increase in *DNA-PK$_{CS}$*$^{-/-}$ MEFs (Figure 5E). In order to analyze the shape of these structures more quantitatively, we calculated the surface area and enclosed volume of the 3D objects. Both the surface area and enclosed volume of 53BP1 foci decreased after irradiation (Figure 5F and G). In addition, both values reached control values in WT MEFs while in *DNA-PK$_{CS}$*$^{-/-}$ MEFs it did not.

The increase of 53BP1 foci size showed a different course in mES cells. We observed a slight increase in size in WT mES cells within 24 hours (Figure 5D). Both *RAD54*$^{-/-}$ and *DNA-PK$_{CS}$*$^{-/-}$ mES cells showed no significant difference in 53BP1 foci size increase until 24 hours post IR, compared to WT.

DISCUSSION

We explored the roles of HR and NHEJ in IR protection by combining HR mutant (RAD54-/-) with NHEJ mutant (DNA-PKCS-/-) mice and cells. We found that the p21 stress response was endogenously elevated in the liver tissue of DNA-PKCS-/- mice and even higher in DNA-PKCS-/-RAD54-/- mice. Moreover, after IR, the p21 stress response in both DNA-PKCS-/- and DNA-PKCS-/-RAD54-/- mice was hyper activated and sustained. We showed that 53BP1 foci dissolution and growth in both MEFs and mES cells lacking DNA-PKCS was impaired. These findings indicate that a combination of NHEJ and HR, in which the extent of each pathway is dependent cell type or genetic background, controls IR protection.

Prominent role of HR as back-up DNA damage repair mechanism in differentiated cells and adult mice

The IR hypersensitivity of *DNA-PK$_{CS}$*$^{-/-}$*RAD54*$^{-/-}$ mice compared to *DNA-PK$_{CS}$*$^{-/-}$ mice phenocopies the synergistic effect of a combined *RAD54* mutation with the *scid* mutation. The *scid* mice

are homozygous for a defect in the mouse homologue of the human *PRKDC*-gene, which leads to an inactive DNA-PK_{CS} protein (32). Thus, the inactivation of DNA-PK_{CS} as in *scid* mice leads to similar IR sensitivity compared to *DNA-PK_{CS}-/-* mice. Interestingly, the phenotype of single mutant *DNA-PK_{CS}* mice is much milder compared to the inactivation of KU80 or LIG4. The loss of KU80 leads to small animal sizes and early death, while loss of LIG4 results in late embryonic death (20-22). In addition, disrupting either KU80 or LIG4 in combination with RAD54 has been reported to cause large amounts of endogenous yH2AX foci (21,22). Interestingly, we did not observe endogenous differences between WT or mutant MEFs and mES cells in number of 53BP1 foci. The absence of endogenous foci in *DNA-$PK_{CS}^{-/-}$RAD54$^{-/-}$* MEFs could implicate a partial role of DNA-PK_{CS} in repair of DSBs arising in S/G2-phase in which KU80 and LIG4 have larger roles. Indeed, DNA-PK_{CS} is reported to be relatively dispensable in the ligation of blunt signal ends in V(D)J recombination (33). Moreover, KU80 has a role in DNA-end protection and LIG4 in ligation of DNA-ends, while DNA-PK_{CS} has been described to have a more 'facilitating' role, mostly tethering NHEJ factors for increased efficiency (34). Apparently, tethering of NHEJ factors is not crucial in the repair of endogenous DNA damage, revealing a less severe effects of DNA-PK_{CS} loss.

Although we did not observe endogenous elevated DNA damage levels between mutant cells, we found differences in IR sensitivity between mutant MEFs and mES cells. We observed that *DNA-$PK_{CS}^{-/-}$RAD54$^{-/-}$* MEFs showed increased IR sensitivity compared to other genotypes. This finding could be compared with the hyper sensitivity of adult mice, suggesting that introducing HR deficiency in a NHEJ deficient background eliminates the back-up role of HR. Taken together, these reports and the observations in this work are suggesting a that HR functions as a back-up DNA damage repair mechanism in differentiated cells and adult mice.

Role for DNA-PK_{CS} in 53BP1 foci induction and dissolution during DNA DSB repair

Disrupted DNA-PK_{CS} leads to more foci per cell after 2 hours, compared to all other genotypes, and impaired dissolution in both MEFs and mES cells. Both *DNA-$PK_{CS}^{-/-}$* and *DNA-$PK_{CS}^{-/-}$RAD54$^{-/-}$* MEFs showed a 2-fold higher induction of initial 53BP1 foci and had not reached similar number of 53BP1 foci as control after 72 hours, while *RAD54$^{-/-}$* MEFs was comparable with WT. The many emerging studies examining the kinetics of DSB repair provided insightful information on DSB repair pathway use (35). For example, it was reported that in the G2-phase of the cell cycle the fast NHEJ pathway repairs 70% of IR-induced DSB. In addition, in G1 up to 80% of the DSBs is thought to be repaired by NHEJ (34). Although Ku has a crucial function as protection of DNA-ends (36), the assembly of the DNA-PK complex ensures tethering of other NHEJ factors. The tethering of NHEJ core-protein is dependent on the kinase activity of DNA-PK_{CS} and thought to contribute to efficient DSB repair by NHEJ (37,38). Therefore, the depletion of DNA-PK_{CS} could decrease the efficiency of NHEJ, making the depletion of DNA-PK_{CS} not as impactful as depletion of Ku (39). The impaired efficiency of NHEJ by DNA-PK_{CS} depletion could explain the impaired 53BP1 foci resolving of *DNA-$PK_{CS}^{-/-}$* and *DNA-$PK_{CS}^{-/-}$RAD54$^{-/-}$* MEFs and *DNA-$PK_{CS}^{-/-}$* ES cells.

Additionally, 53BP1 foci growth in both *DNA-PK$_{CS}^{-/-}$* and *DNA-PK$_{CS}^{-/-}$RAD54$^{-/-}$* MEFs was significantly impaired compared to *RAD54$^{-/-}$* and WT MEFs. DSB foci growth is caused by chromatin decondensation or expansion of chromatin signaling (34). ATM initiates the IR-induced chromatin signaling cascade to phosphorylate H2AX. However, in ATM-deficient cells phosphorylation of H2AX still occurs mediated by DNA-PK$_{CS}$ (40). In addition, ATM also has an important role in phosphorylating KAP1, driving local chromatin decondensation as result of ionizing radiation exposure. Interestingly, both phosphorylation of KAP1 and chromatin decondensation was diminished in *DNA-PK$_{CS}^{-/-}$* HCT116 cells, while ATM inhibition had no additional effect (41-43). These reports suggest an active role for DNA-PK$_{CS}$ in the initial amplification of chromatin signaling and decondenstation. Recruitment of 53BP1 is a consequence of H2AX phosphorylation, mediated by the RNF8 ubiquitination cascade, and could therefore be impaired in a *DNA-PK$_{CS}^{-/-}$* background (44). Collectively, the impaired 53BP1 foci growth in *DNA-PK$_{CS}^{-/-}$* cell lines could be the cause of inefficient ATM-dependent chromatin signaling or KAP1-dependent chromatin decondensation.

Analysis of the p21 response in DNA DSB repair deficient mice

The p53 tumor suppressor protein mediates the transcriptional regulation of p21. Hence, in response of DNA damage, p21 expression is upregulated. The p21 protein has a central role in determining cellular responses to cellular results, mainly by inhibitory control over the cell cycle (31). We investigated the *in vivo* p21 expression following IR using p21-reporter mice, which showed endogenous elevated p21 expression in mice lacking DNA-PK$_{CS}$. Moreover, we found that p21 expression was hyper activated and sustained after IR in *DNA-PK$_{CS}^{-/-}$* and *DNA-PK$_{CS}^{-/-}$RAD54$^{-/-}$* mice, mainly in the highly proliferative intestinal tract. This correlates with the observation of impaired 53BP1 dissolution in *DNA-PK$_{CS}^{-/-}$* MEFs and mES. Interestingly, the introduction of RAD54 mutations had no additive effect on the impaired DSB repair in *DNA-PK$_{CS}^{-/-}$* MEFs. This seems contradictory to adult mice, where RAD54 deletion was synergistic for IR resistance and induced higher p21 expression. A possible reason could be that the role of RAD54 in genome maintenance is differential between tissues. Consistent with this, we found that RAD54 depletion in mES cells did cause impaired 53BP1 foci resolving, which could be extrapolated to the IR sensitivity of *RAD54$^{-/-}$* embryo's (20).

It is interesting to speculate that IR protection is differentially regulated between tissues. An abundance of work has been documented on how high-dose IR affects mice, which showed that the gastrointestinal (GI) system is the most affected, leading to the survival of 6-8 days (45). We observed a maximum of 8 days of survival after 3 Gy in an *DNA-PK$_{CS}^{-/-}$RAD54$^{-/-}$* background (Figure 1). In addition, the combination of KU80 and RAD54 deficiency showed similar survival after 0.2 Gy (21). Moreover, IR induced sustained p21 expression in the GI of *DNA-PK$_{CS}^{-/-}$* and *DNA-PK$_{CS}^{-/-}$RAD54$^{-/-}$*, suggesting unrepaired DNA damage (Figure 3B).

Together with our finding that RAD54 might have a larger role in embryonic cells compared to differentiated cells in DSB repair, suggest that the embryonic crypt villi in the GI have a limiting

role in IR protection. This would explain the synergistic effect of *RAD54* depletion in adult mice in a NHEJ background, making embryonic cells in the GI highly sensitive for IR.

In conclusion, we demonstrate that the p21 response is a highly sensitive DNA damage marker, able to detect endogenous DNA damage in mice deficient for NHEJ. In differentiated cells, only NHEJ is required for efficient 53BP1 foci dissolution and growth, while in stem cells both NHEJ and HR are required. Our data are consistent with a prominent role for HR in undifferentiated cell types, switching to the background during differentiation of cells. Together, our findings suggest that cell type or genetic background determines the extent of which NHEJ or HR partakes in repair of IR induced DSBs

ACKNOWLEDGEMENTS

We would like to thank Dr. F. Alt for the *DNA-PKCS-/-* mES cell lines, Dr. G. Taccioli for *DNA-PKCS* deficient mice. In addition, we would like to thanks Stijn de Jong for his contribution on quantifying 53BP1 foci. This work was supported with imaging equipment provided by the Applied Molecular Imaging Erasmus MC facility (AMIE). This project was funded by Technologie stichting STW, project number 13577.

REFERENCES

1. Shibata, A. and Jeggo, P.A. (2014) DNA double-strand break repair in a cellular context. *Clin Oncol (R Coll Radiol)*, **26**, 243-249.
2. Hoeijmakers, J.H. (2009) DNA damage, aging, and cancer. *N Engl J Med*, **361**, 1475-1485.
3. Jackson, S.P. and Bartek, J. (2009) The DNA-damage response in human biology and disease. *Nature*, **461**, 1071-1078.
4. Panier, S., Ichijima, Y., Fradet-Turcotte, A., Leung, C.C.Y., Kaustov, L., Arrowsmith, C.H. and Durocher, D. (2012) Tandem Protein Interaction Modules Organize the Ubiquitin-Dependent Response to DNA Double-Strand Breaks. *Molecular Cell*, **47**, 383-395.
5. Huen, M.S.Y., Grant, R., Manke, I., Minn, K., Yu, X., Yaffe, M.B. and Chen, J. (2007) RNF8 Transduces the DNA-Damage Signal via Histone Ubiquitylation and Checkpoint Protein Assembly. *Cell*, **131**, 901-914.
6. Mattiroli, F., Vissers, J.H., van Dijk, W.J., Ikpa, P., Citterio, E., Vermeulen, W., Marteijn, J.A. and Sixma, T.K. (2012) RNF168 ubiquitinates K13-15 on H2A/H2AX to drive DNA damage signaling. *Cell*, **150**, 1182-1195.
7. Panier, S. and Boulton, S.J. (2014) Double-strand break repair: 53BP1 comes into focus. *Nat Rev Mol Cell Bio*, **15**, 7-18.
8. Ochs, F., Somyajit, K., Altmeyer, M., Rask, M.B., Lukas, J. and Lukas, C. (2016) 53BP1 fosters fidelity of homology-directed DNA repair. *Nature Structural and Molecular Biology*, **23**, 714-721.
9. Gottlieb, T.M. and Jackson, S.P. (1993) The DNA-Dependent Protein-Kinase - Requirement for DNA Ends and Association with Ku Antigen. *Cell*, **72**, 131-142.
10. Ciccia, A. and Elledge, S.J. (2010) The DNA Damage Response: Making It Safe to Play with Knives. *Molecular Cell*, **40**, 179-204.
11. Yannone, S.M., Khan, I.S., Zhou, R.Z., Zhou, T., Valerie, K. and Povirk, L.F. (2008) Coordinate 5' and 3' endonucleolytic trimming of terminally blocked blunt DNA double-strand break ends by Artemis nuclease and DNA-dependent protein kinase. *Nucleic Acids Res*, **36**, 3354-3365.
12. Ahnesorg, P., Smith, P. and Jackson, S.P. (2006) XLF interacts with the XRCC4-DNA ligase IV complex to promote DNA nonhomologous end-joining. *Cell*, **124**, 301-313.
13. Lieber, M.R. (2010) The mechanism of double-strand DNA break repair by the nonhomologous DNA end-joining pathway. *Annu Rev Biochem*, **79**, 181-211.
14. Wyman, C. and Kanaar, R. (2006) DNA Double-Strand Break Repair: All's Well that Ends Well. *Annual Review of Genetics*, **40**, 363-383.
15. Densham, R.M. and Morris, J.R. (2019) Moving Mountains-The BRCA1 Promotion of DNA Resection. *Front Mol Biosci*, **6**, 79.
16. Chen, H., Lisby, M. and Symington, L.S. (2013) RPA coordinates DNA end resection and prevents formation of DNA hairpins. *Mol Cell*, **50**, 589-600.
17. Liu, J., Doty, T., Gibson, B. and Heyer, W.D. (2010) Human BRCA2 protein promotes RAD51 filament formation on RPA-covered single-stranded DNA. *Nat Struct Mol Biol*, **17**, 1260-1262.
18. Renkawitz, J., Lademann, C.A., Kalocsay, M. and Jentsch, S. (2013) Monitoring homology search during DNA double-strand break repair in vivo. *Mol Cell*, **50**, 261-272.
19. Essers, J., Hendriks, R.W., Swagemakers, S.M., Troelstra, C., de Wit, J., Bootsma, D., Hoeijmakers, J.H. and Kanaar, R. (1997) Disruption of mouse RAD54 reduces ionizing radiation resistance and homologous recombination. *Cell*, **89**, 195-204.

20. Essers, J., van Steeg, H., de Wit, J., Swagemakers, S.M., Vermeij, M., Hoeijmakers, J.H. and Kanaar, R. (2000) Homologous and non-homologous recombination differentially affect DNA damage repair in mice. *EMBO J*, **19**, 1703-1710.
21. Couedel, C., Mills, K.D., Barchi, M., Shen, L., Olshen, A., Johnson, R.D., Nussenzweig, A., Essers, J., Kanaar, R., Li, G.C. *et al.* (2004) Collaboration of homologous recombination and nonhomologous end-joining factors for the survival and integrity of mice and cells. *Genes Dev*, **18**, 1293-1304.
22. Mills, K.D., Ferguson, D.O., Essers, J., Eckersdorff, M., Kanaar, R. and Alt, F.W. (2004) Rad54 and DNA Ligase IV cooperate to maintain mammalian chromatid stability. *Genes Dev*, **18**, 1283-1292.
23. McMahon, M., Frangova, T.G., Henderson, C.J. and Wolf, C.R. (2016) Olaparib, Monotherapy or with Ionizing Radiation, Exacerbates DNA Damage in Normal Tissues: Insights from a New p21 Reporter Mouse. *Mol Cancer Res*, **14**, 1195-1203.
24. Bazalova M, G.E. (2016) MicroCT dose and image quality for in vivo microCT systems. *Unpubl. data*.
25. Peeters, P.J., Fierens, F.L., van den Wyngaert, I., Goehlmann, H.W., Swagemakers, S.M., Kass, S.U., Langlois, X., Pullan, S., Stenzel-Poore, M.P. and Steckler, T. (2004) Gene expression profiles highlight adaptive brain mechanisms in corticotropin releasing factor overexpressing mice. *Brain Res Mol Brain Res*, **129**, 135-150.
26. Hosack, D.A., Dennis, G., Sherman, B.T., Lane, H.C. and Lempicki, R.A. (2003) Identifying biological themes within lists of genes with EASE. *Genome Biol*, **4**.
27. Kramer, A., Green, J., Pollard, J., Jr. and Tugendreich, S. (2014) Causal analysis approaches in Ingenuity Pathway Analysis. *Bioinformatics*, **30**, 523-530.
28. Kabacik, S., Ortega-Molina, A., Efeyan, A., Finnon, P., Bouffler, S., Serrano, M. and Badie, C. (2011) A minimally invasive assay for individual assessment of the ATM/CHEK2/p53 pathway activity. *Cell Cycle*, **10**, 1152-1161.
29. Soille, P. and Vincent, L. (1990) Determining Watersheds in Digital Pictures Via Flooding Simulations. *P Soc Photo-Opt Ins*, **1360**, 240-250.
30. Mujoo, K., Pandita, R.K., Tiwari, A., Charaka, V., Chakraborty, S., Singh, D.K., Hambarde, S., Hittelman, W.N., Horikoshi, N., Hunt, C.R. *et al.* (2017) Differentiation of Human Induced Pluripotent or Embryonic Stem Cells Decreases the DNA Damage Repair by Homologous Recombination. *Stem Cell Reports*, **9**, 1660-1674.
31. Warfel, N.A. and El-Deiry, W.S. (2013) p21WAF1 and tumourigenesis: 20 years after. *Curr Opin Oncol*, **25**, 52-58.
32. Blunt, T., Finnie, N.J., Taccioli, G.E., Smith, G.C., Demengeot, J., Gottlieb, T.M., Mizuta, R., Varghese, A.J., Alt, F.W., Jeggo, P.A. *et al.* (1995) Defective DNA-dependent protein kinase activity is linked to V(D)J recombination and DNA repair defects associated with the murine scid mutation. *Cell*, **80**, 813-823.
33. Jung, D. and Alt, F.W. (2004) Unraveling V(D)J recombination; insights into gene regulation. *Cell*, **116**, 299-311.
34. Shibata, A. and Jeggo, P.A. (2020) Roles for the DNA-PK complex and 53BP1 in protecting ends from resection during DNA double-strand break repair. *J Radiat Res*, **61**, 718-726.
35. Lobrich, M. and Jeggo, P. (2017) A Process of Resection-Dependent Nonhomologous End Joining Involving the Goddess Artemis. *Trends Biochem Sci*, **42**, 690-701.
36. Walker, J.R., Corpina, R.A. and Goldberg, J. (2001) Structure of the Ku heterodimer bound to DNA and its implications for double-strand break repair. *Nature*, **412**, 607-614.
37. Wang, J.L., Duboc, C., Wu, Q., Ochi, T., Liang, S.K., Tsutakawa, S.E., Lees-Miller, S.P., Nadal, M., Tainer, J.A., Blundell, T.L. *et al.* (2018) Dissection of DNA double-strand-break repair using novel single-molecule forceps. *Nature Structural & Molecular Biology*, **25**, 482-+.

38. Wu, Q. (2019) Structural mechanism of DNA-end synapsis in the non-homologous end joining pathway for repairing double-strand breaks: bridge over troubled ends. *Biochem Soc Trans*, **47**, 1609-1619.
39. Riballo, E., Kuhne, M., Rief, N., Doherty, A., Smith, G.C.M., Recio, M.J., Reis, C., Dahm, K., Fricke, A., Krempler, A. *et al.* (2004) A pathway of double-strand break rejoining dependent upon ATM, artemis, and proteins locating to gamma-H2AX foci. *Molecular Cell*, **16**, 715-724.
40. Lu, H., Saha, J., Beckmann, P.J., Hendrickson, E.A. and Davis, A.J. (2019) DNA-PKcs promotes chromatin decondensation to facilitate initiation of the DNA damage response. *Nucleic Acids Res*, **47**, 9467-9479.
41. Stiff, T., O'Driscoll, M., Rief, N., Iwabuchi, K., Lobrich, M. and Jeggo, P.A. (2004) ATM and DNA-PK function redundantly to phosphorylate H2AX after exposure to ionizing radiation. *Cancer Res*, **64**, 2390-2396.
42. Meyer, B., Voss, K.O., Tobias, F., Jakob, B., Durante, M. and Taucher-Scholz, G. (2013) Clustered DNA damage induces pan-nuclear H2AX phosphorylation mediated by ATM and DNA-PK. *Nucleic Acids Research*, **41**, 6109-6118.
43. Savic, V., Yin, B., Maas, N.L., Bredemeyer, A.L., Carpenter, A.C., Helmink, B.A., Yang-Lott, K.S., Sleckman, B.P. and Bassing, C.H. (2009) Formation of Dynamic gamma-H2AX Domains along Broken DNA Strands Is Distinctly Regulated by ATM and MDC1 and Dependent upon H2AX Densities in Chromatin. *Molecular Cell*, **34**, 298-310.
44. Schultz, L.B., Chehab, N.H., Malikzay, A. and Halazonetis, T.D. (2000) p53 Binding protein 1 (53BP1) is an early participant in the cellular response to DNA double-strand breaks. *Journal of Cell Biology*, **151**, 1381-1390.
45. Booth, C., Tudor, G., Tudor, J., Katz, B.P. and MacVittie, T.J. (2012) Acute gastrointestinal syndrome in high-dose irradiated mice. *Health Phys*, **103**, 383-399.

SUPPLEMENTAL FIGURES

Supplemental Table 1. Expression fold change of *CDKN1A* relative to WT.

Genotype	Fold change probe 1	p-value	Fold change probe 2	p-value
RAD54-/-	-1.00	0.9985	1.04	0.8620
DNA-PKCS-/-	1.85	0.1793	1.54	**0.0436**
DNA-PKCS-/-RAD54-/-	2.15	**0.0158**	1.85	**0.0067**

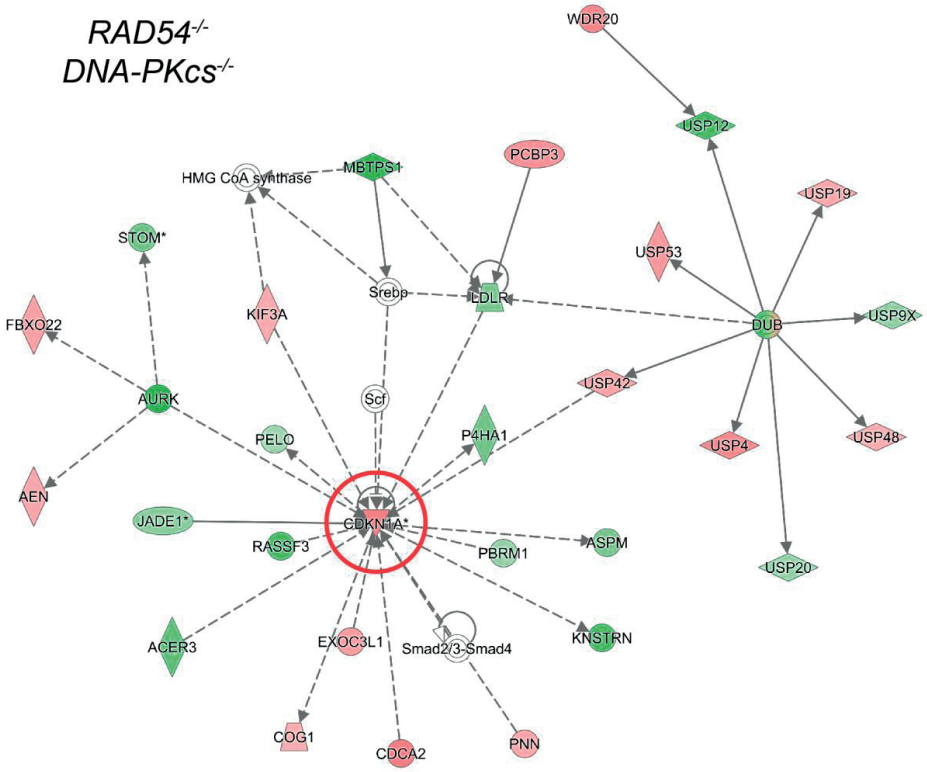

Supplemental figure 1. Ingenuity Pathway Analysis top network in *DNA-PKCS-/-RAD54-/-* mice. Gene expression log ratios: red, upregulated; green, downregulated. Color intensity correlated with the degree of change.

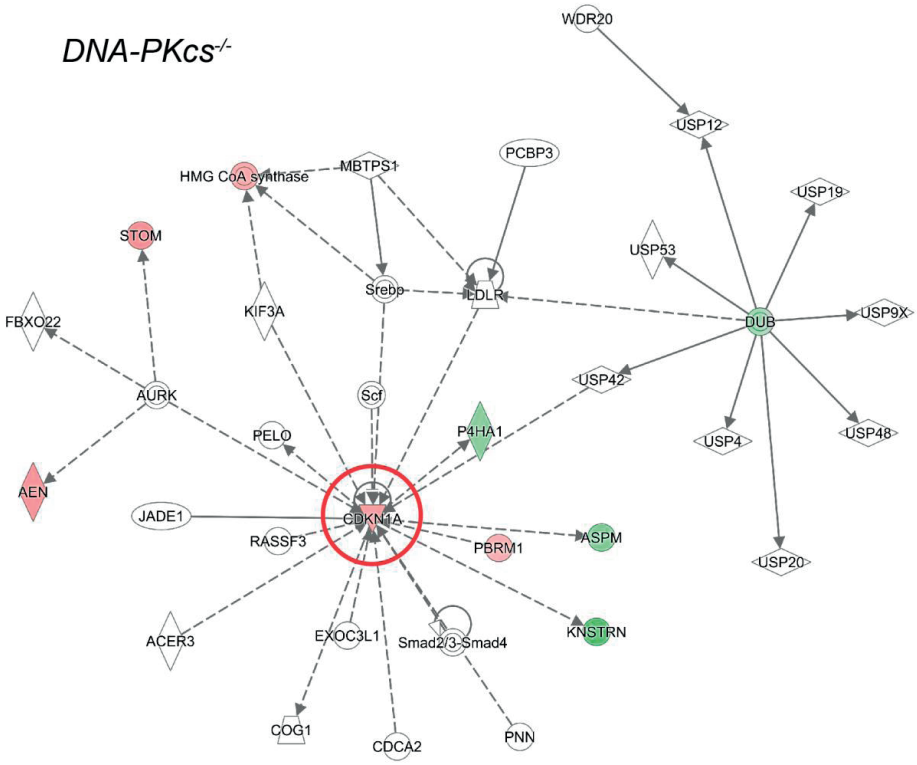

Supplemental figure 2. Ingenuity Pathway Analysis top network in *DNA-PKCS-/-* mice. Gene expression log ratios: red, upregulated; green, downregulated. Color intensity correlated with the degree of change.

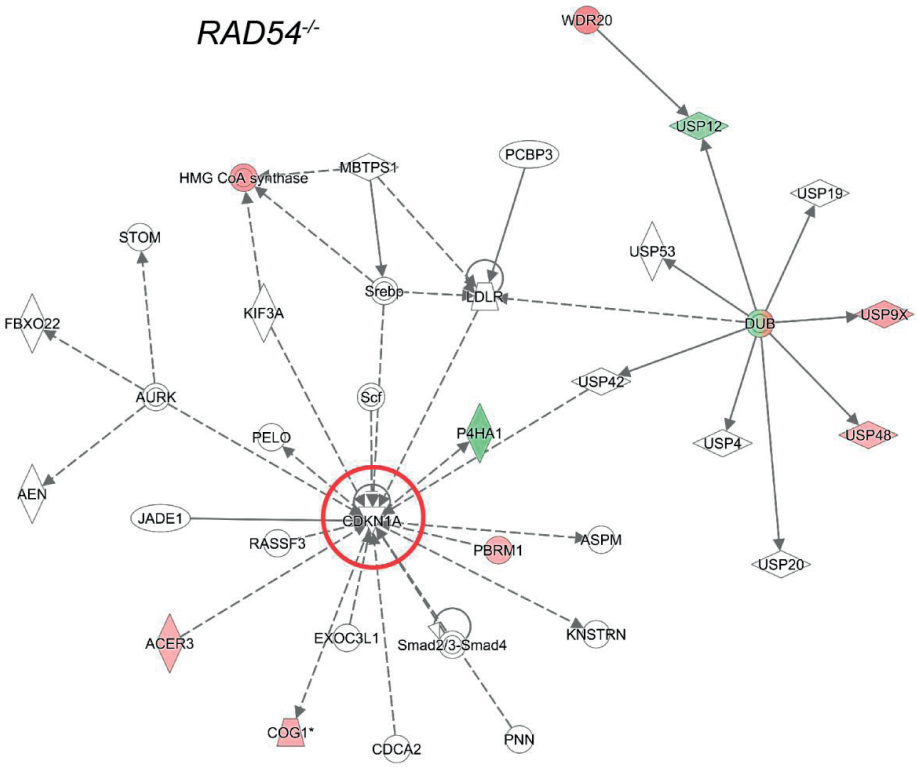

Supplemental figure 3. Ingenuity Pathway Analysis network around CDKN1A in *RAD54-/-* mice. Gene expression log ratios: red, upregulated; green, downregulated. Color intensity correlated with the degree of change.

3

Large Field Alpha Irradiation Setup for Radiobiological Experiments

Stefan J. Roobol [1,2,3], Jasper J.M. Kouwenberg [4], Antonia G. Denkova [5], Roland Kanaar [1,2] and Jeroen Essers [1,6,7,*]

[1]Department of Molecular Genetics, Erasmus University Medical Center, Rotterdam, 3000 CA, The Netherlands

[2]Oncode Institute, Erasmus University Medical Center, Rotterdam, 3000 CA, The Netherlands

[3]Department of Radiology & Nuclear Medicine, Erasmus University Medical Center, Rotterdam, 3000 CA, The Netherlands

[4]Department of Radiotherapy, Erasmus University Medical Center, Rotterdam, 3015 GD, The Netherlands

[5]Department of Radiation Science and Technology, Delft University of Technology, Delft, 2629 JB, The Netherlands

[6]Department of Radiation Oncology, Erasmus University Medical Center, Rotterdam, 3000 CA, The Netherlands

[7]Department of Vascular Surgery, Erasmus University Medical Center, Rotterdam, 3000 CA, The Netherlands

* Correspondence: j.essers@erasmusmc.nl;

Methods and Protoc. 2019, 2, 75

ABSTRACT

The use of alpha particles irradiation in clinical practice has gained interest in the past years, for example with the advance of radionuclide therapy. The lack of affordable and easily accessible irradiation systems to study the cell biological impact of alpha particles hampers broad investigation. Here we present a novel alpha particle irradiation set-up for uniform irradiation of cell cultures. By combining a small alpha emitting source and a computer-directed movement stage, we established a new alpha particle irradiation method allowing more advanced biological assays, including large-field local alpha particle irradiation and cell survival assays. In addition, this protocol uses cell culture on glass cover-slips which allows more advanced microscopy, such as super-resolution imaging, for in-depth analysis of the DNA damage caused by alpha particles. This novel irradiation set-up provides the possibility to perform reproducible, uniform and directed alpha particle irradiation to investigate the impact of alpha radiation on the cellular level.

Keywords: alpha particle; irradiation; microscopy; DSB; 53BP1; DNA damage; FNTD; dosimetry; external irradiation;

INTRODUCTION

Understanding the impact of alpha particles on biological material, such as DNA, is of utmost importance to verify and optimize future radionuclide therapy. Current studies in radiobiology focus on different radiation types with respect to the biological harm that different isotopes can induce in cellular systems. However, the exact biological effects of alpha particles, in the context of DNA damage, is still poorly understood. The high linear energy transfer (LET) of alpha particles, compared to beta- and gamma- irradiation, induces more cell death, which results in high relative biological effectiveness (RBE) [1]. This effectiveness is due to the short distance between individual ionization caused by alpha particles [2,3]. In addition, the highly ionizing path of alpha particles induces clusters of double stranded breaks (DSBs) in the DNA along a straight track (10–20 DSBs per 10 µm track length) [4]. Therefore, the use of alpha particle emitting radionuclides, conjugated to antibodies or clonogenic survival peptides shows great promise improving radiotherapy in the clinic, through specific targeting and by exploiting the short path length to limit damage of healthy tissue [5-8].

The development of experimental alpha particle irradiation has seen a lot of attention in the past [9-17]. These studies mainly focused on dosimetry and bystander effects. More recent setups show increased complexity in radiation procedures but great promise in experimental radiobiology [1822]. However, the active surface of commercially available alpha particle sources (e.g., from Eckert and Ziegler) are often smaller in diameter than culture dishes, thereby precluding quantitative cell colony formation assays, and require optimized protocols for alpha-track irradiation [22,23]. To allow an uniform alpha irradiation of large fields of cells using a small source a novel irradiation setup was developed [24]. Here we describe the procedure for large field irradiation using a relatively small alpha particle emitting ^{241}Am source. In addition, this procedure was used for a novel method for alpha radiation (micro-) dosimetry using fluorescent nuclear track detectors (FNTDs) [16,24,25]. Using computer directed irradiation on cell populations cultured in Mylar dishes allows elaborate cell population assays, compared to previously reported methods [4,9-15,17-23,26,27]. Moreover, the irradiation procedure has been adjusted for cell culture on glass-coverslips, allowing to avoid the Mylar-based culture conditions and the possibility for super-resolution imaging. With the use of glass coverslips, repair proteins of several DSB-repair pathways can be studied in high resolution using techniques such as stochastic optical reconstruction microscopy (STORM) or structured illumination microscopy (SIM) [28]. With the use of the right materials and conditions this protocol could yield fast and reliable answers to biological questions regarding alpha particle induced DSBs or cell survival after irradiation with alpha particles. The setup was validated using immunofluorescence in combination with the use of SIM as super resolution technique and clonogenic survival assays were carried out, which demonstrate the effective irradiation of larger areas of cells.

EXPERIMENTAL DESIGN

This protocol was developed in need of biological assays using alpha particle irradiation. In this study we used U2OS cells as model cell culture and irradiated the cells using alpha particles emitted by a ^{241}Am source. The active surface of the source was controlled by an in house built automated stage for precise dosimetry during irradiation (Figure 1). By culturing cells on Mylar, a very thin foil, the alpha particles were able to reach the cells, allowing the cells to be irradiated from beneath whilst in their normal culture medium. In addition, this protocol describes a procedure to irradiate U2OS cells cultured on glass coverslips by alpha particles. This technique allowed super resolution imaging on irradiated cells.

This protocol is divided in several steps required to achieve the goals stated above. First, the preparation of custom-made Mylar dishes. Second, culturing U2OS cells using Mylar dishes or glass coverslips. Third, the irradiation procedure for both a large field of cells or only a specific area on the coverslip. Irradiated cells can be used for conventional clonogenic survival assays or immunohistochemistry.

Materials

- Acetone (Sigma-Aldrich, Zwijndrecht, The Netherlands, Cat. No. 154598-1L)
- Ethanol absolute (VWR Chemicals, Paris, France, Cat. No. 83813.360)
- Sterile Distilled Water
- Dulbecco's Phosphate-buffered saline, pH 7.4 (PBS, Sigma-Aldrich, Cat. No. D8537-500ML)

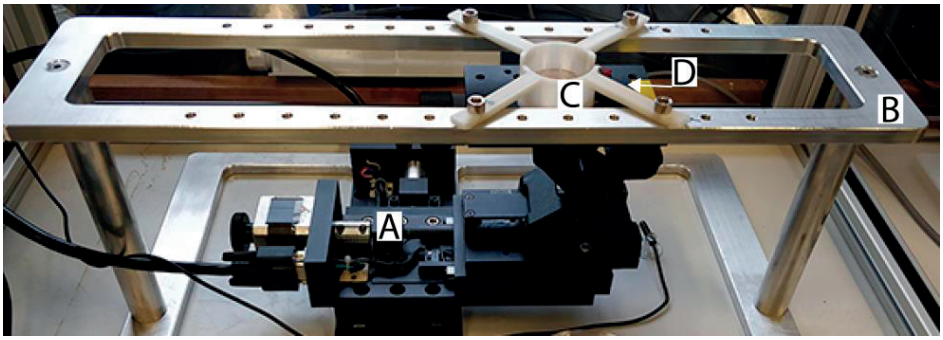

Figure 1. Overview of the automated external alpha particle irradiation set-up. (**A**) Two motorized linear stages connected to the Motion controller and the PC. (**B**) Aluminum frame as frame for the device (Design S1). (**C**) Culture dish holder (Design S2). (**D**) Radioactive source collimator (Design S3).

- Dulbecco's Modified Eagle Medium (DMEM, Gibco, Thermo Fisher, Waltham, MA, USA, Cat. No. 11965092)
- Fetal Bovine Serum (Capricorn Scientific, Ebsdorfergrund, Germany, Cat. No. FBS-12A)
- Penicillin/streptomycin (Gibco, Thermo Fisher, Cat. No. 15140122)

- 0.05% (w/v) Trypsin 0.53 EDTA solution (Sigma-Aldrich, Cat. No. T3924-500ML
- Vectashield with DAPI (Vector Laboratories, Burlingame, CA, USA, Cat. No. H-1200)
- HEPES Buffer (Lonza, Portsmouth, NH, USA, Cat. No. 17-737E, pH: 6.98 – 7.3, Counter ion: NaCl)

Equipment

- Pipette 1 mL (Gilson, Den Haag, The Netherlands, Cat. No. F123602)
- Laboratory tweezers (Fine Science Tools, Heidelberg, Germany, Cat. No. 11252-00)
- Alpha particle emitting ^{241}Am source of 1.1 cm in diameter with an activity of 409.6 kBq (Czech Metrological Institute, Jihlava, The Czech Republic)
- Polyster plain film (Mylar), 1.9 µm thickness (Birkelbach Kondensatortechnik, Erndtebrueck, Germany, Cat. No. PTPL)
- Cardboard (any type will suffice, dimensions at least: 50 × 50 cm)
- Adhesive tape (any type will suffice)
- Lumox 35 dishes (Sarstedt, Nümbrecht, Germany, Cat. No. 94.6077.333)
- 10 cm culture dishes (Greiner Bio-One, Alphen aan den Rijn, The Netherlands, Cat. No.664160)
- Sandpaper (any type will suffice)
- Sanyo MCO-17AIC Copper Alloy CO2 Incubator (Marshall Scientific, Hampton, NH, United States, Cat. No. SANYOMCO)
- Microscope slide coverslips with 10 mm ø or smaller (Thermo Fisher Scientific, Cat. No. CB00100RA020MNT0)
- Disposable Scalpels - Sterile (Swann-Morton, Sheffield, United Kingdom, Cat. No. 0503)
- UV-irradiation set-up (Erasmus MC, Rotterdam, The Netherlands, Homemade)
- 2× Motorized linear stages, resolution: 0.625 µm (Optics-Focus, Beijing, China, Cat. No. MOX-02-50)
- Manual laboratory jack, resolution: 0.01 mm (Optics-Focus, Cat. No. 8MAJ60)
- Motion Controller (Optics-Focus, Cat. No. MOC-01-1-220)
- Metal frame (TU Delft, Delft, The Netherlands, Homemade, Design S1)
- 3-D printed Dish holder of ABS plastic(TU Delft, Homemade, Design S2)
- 3-D printed Collimator of ABS plastic (TU Delft, Homemade, Design S3)
- Large Polymethyl Methacrylate box to case the whole set-up and for heating, volume of 0.22 m^3 (TU Delft, Homemade)
- Thin washers (Modelfixings.co.uk, Nottingham, United Kingdom, Cat. No. MF-SHW71301)
- Computer running MatLab (MathWorks, Natick, MA, USA)
- Compact Hairdryer (BaByliss, Paris, France, Cat. No. D212E)
- ThermoControl 2 (Lucky Reptile, Waldkirch, Germany, Cat. No. LR62121)

PROCEDURE

Calibration of the Irradiation Stage (Recalibrate This Once a Month). Time for Completion: 30 min

1. Bolt the culture dish holder and the collimator on the aluminum frame (Figure 1B, Design S1-3).
2. Align the centers of the collimator and the dish holder. The alignment can be judged visually when the collimator is raised to the level of the culture dish holder. Store the x, y-coordinates of the linear stages (Figure 1A) in the control software after alignment.
3. Adjust the gap between upper rim (e.g., the bottom of the culture dish, Figure 1C) and the top of the collimator to the appropriate size (2.8 mm) using the laboratory jack and a caliper (Figure 1D). Measure the gap size near each leg of the culture dish holder to check for a possible tilt. Remove this tilt by raising the legs using thin non-corroding washers so that the measured gaps near the legs are equal.

⚠ **CRITICAL STEP:** When the dish holder has not been removed, steps 2 and 3 can be skipped. A monthly check of the gap size and culture dish holder tilt is in this case sufficient.

4. Place the circular ^{241}Am source in the holder with collimator and bolt the assembly on the laboratory jack on the linear stages (Figure 2).
5. Cover the whole set-up with the large Perspex box and place the Compact Hairdryer inside connected to the ThermoControl 2 for temperature control. Set the ThermoControl 2 to 37 °C.

Mylar Dish Preparation. Time for Completion: 3 h

1. Stretch the Mylar on the piece of cardboard, fix edges using tape. Make sure there are no apparent damages on the Mylar surface before use.
2. Remove the factory applied foil and scour the bottom of the Lumox dishes using sandpaper. Wash both the scoured dish and lid of the Lumox dish and dry before the next step.
3. Pour a small volume of acetone into a glass dish. Dip the scoured and cleaned Lumox ring in the acetone and keep in place for 10 s. Remove the ring from the acetone and move over to

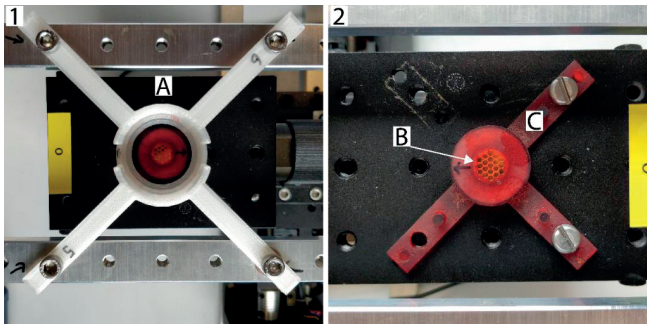

Figure 2. Top view of the irradiation set-up. Panel 1: (**A**) Top view with dish and source collimator in place. The source is aligned in the middle of the culture dish holder (Design S2). Panel 2: (**B**) Radioactive surface protected by gold inside the source collimator. (**C**) 3-D printed source collimator (Design S3).

the stretched Mylar. Press the ring firmly on the, undamaged, Mylar and hold for 30 s. Let dry for at least 2 h.

⚠ **CRITICAL STEP**: Do not move the ring while pressing on the Mylar, this could cause leakage later on. Make sure the Mylar surface inside the Lumox ring is damage free.

4. Add 1 mL 70% ethanol to the dish to check for possible leaking spots. Aspirate the Ethanol if the Mylar dish is not leaking.
5. Carefully cut the Mylar around the Mylar dish (minimum of 0.5 cm away from the edge) and store the Mylar dishes in 10 cm tissue culture dishes (2 per 10 cm dish).
6. Sterilization of Mylar Dishes can be done by UV (~ 140 J/m^2) irradiation or 70% ethanol wash (minimum 3 times). Always wash with sterile PBS or sterile MQ water.

⏸ **PAUSE STEP**: The protocol can be paused here for a maximum of 3 days. Store the Mylar dishes at 4 °C and keep moist with PBS.

Cell Culture. Time for Completion: 30 min

Depending on the type of experiment, seeding of cells should be done by either procedure 3.3.1 or 3.3.2. For field irradiation (e.g., for clonogenic survival) procedure 3.3.1 should be used. For immunofluorescence or experiments where coverslips are a requirement procedure 3.3.2 should be used.

⚠ **CRITICAL STEP:** Culture should be near 90% confluence to yield sufficient number of irradiated cells.

3.3.1. Seed The U2OS Cells at A Concentration of 100,000−200,000 Cells in A Mylar Dish in 2 mL of Medium. Culture Cells Overnight, Covering the Mylar Dishes Using the Lids of The LUMOX Dishes.

⚠ **CRITICAL STEP**: Growing other types of cells on Mylar could provide difficulty in attachment. Solutions to possible attachment problems are coating with laminin, gelatin or polylysine. In case of severe attachment problems, users could consider glow-discharged carbon coating [29].

3.3.2. Seed U2OS Cells in a 6-wells Plate with Glass Coverslips (10 mm ø or smaller) in the Wells. Culture Cells for 24 h in the 6-wells Plate.

⚠ **CRITICAL STEP:** Be sure that the used coverslips are 10 mm ø or smaller.

Irradiation Procedure

Time of Completion: Depends on the required dose. For example: 2 Gray on a Mylar dish is 02:30 h and 2 Gray on a coverslip is 8 min. Workflow: The script is used to cover 19 positions under the Mylar dish for complete irradiation coverage of the dish. The timing of each position is entered in the program by the user and determines the dose deposited at that position. After each position has been irradiation (e.g., for 240.1 s) the collimator is redirected back to its original position and the irradiation is complete. Depending on the type of experiment, irradiation of cells should be done by either procedure 3.4.1. or 3.4.2. For field irradiation (e.g., for clonogenic survival) procedure 3.4.1. should be used. For immunofluorescence or experi-

ments where cover slips are a requirement procedure 3.4.2. should be used. Figure 3 shows a schematic overview of the irradiation procedures.

Irradiation of Cells Grown in the Mylar Dish

1. Turn on the computer and stage controller. Open MatLab script "Automated irradiation stage.m" in MatLab and press run.
2. Turn on the heating in the irradiation box and wait for it to reach to 37 °C. Add 20 µL/mL

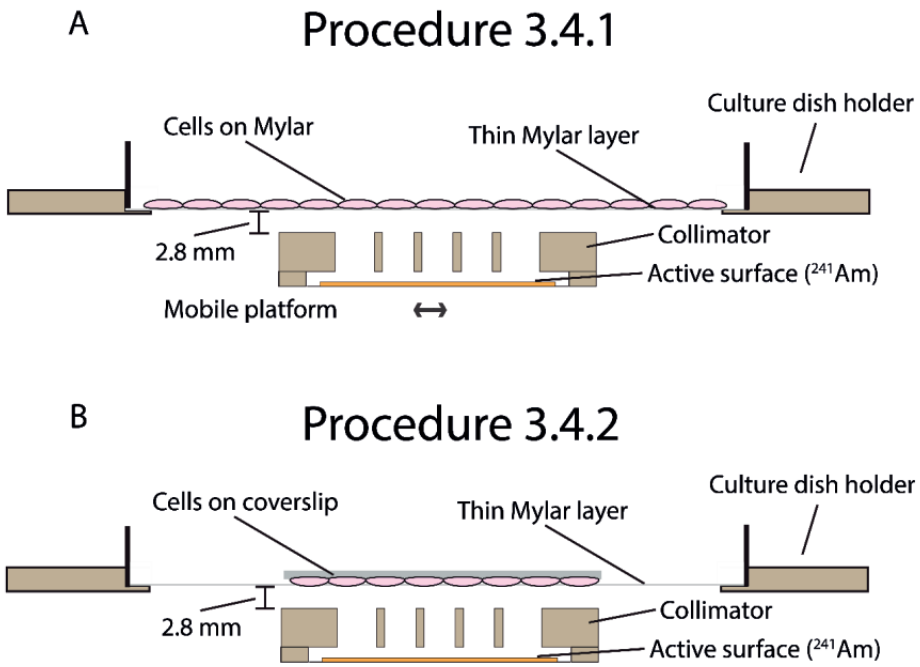

Figure 3. Schematic side views of both irradiation procedures. (**A**) Procedure 3.4.1 is meant for large field irradiation. Cells are grown in Mylar dishes. During the irradiation the active surface is mobile and irradiates the whole area covered with cells. (**B**). Procedure 3.4.2 is meant for coverslip irradiation. In this procedure the active surface is stationary and irradiates the coverslip.

HEPES (20 mm) buffer to each Mylar dish.

3. Carefully place the Mylar dish in the dish holder. All Mylar dishes should have their lids on at all times.

⚠ **CRITICAL STEP:** make sure the dish is level in the holder. A skewed positioning will affect the dose on the cells.

4. Start the irradiation sequence in the controller software. Use Table 1 to calculate the irradiation time (in seconds) to fill in your time per irradiation point. Example: 1 Gy requires 240.1 s (4 min) of irradiation per position.

5. Once the irradiation sequence is completed, carefully remove the Mylar dish from the irradiation setup. Depending on the type of sequential experiments, cells can now be trypsinized for further experimentation.

⚠ **CRITICAL STEP:** Cells have been in a variable temperature and non-buffered area for multiple h due to the irradiation time. This can affect the robustness of cells in general. Use control samples which undergo the same conditions as the experimental samples.

Table 1. Characteristics of the described ^{241}Am source and current setup. Adapted from [24]. Used for calculating the irradiation time.

Characteristic	Value
Area of active surface (mm^2)	11
Source fluence at cell position (particles/s /cm^2)	15966
Half-life (days)	157800
Distance between the active surface and mylar (mm)	5.0 (± 0.1)
Distance between collimator and Culture dish holder (mm)	2.8 (± 0.1)
Irradiation time per point (s/Gy)[1]	240.1 (± 5.9%)

[1] Calculated in an 8 µm layer of water above a 1.4 µm Mylar sheet, irradiated in 2017 using the described ^{241}Am source.

Irradiation of Cells Grown on A Glass Cover Slip

1. Turn on the computer and stage controller. Open MatLab script "Automated irradiation stage.m" in MatLab and press run.
2. Turn on the heating in the irradiation box and wait for it to reach to 37 °C.
3. Remove the cover slip from the medium and wash with PBS. Try to remove as much as PBS as possible using paper tissues and put the cover slip up-side-down exactly in the center of the Mylar dish.

⚠ **CRITICAL STEP:** Be sure that the cells are facing down and are in between the Mylar and the glass cover slip.

4. Carefully place the Mylar dish in the dish holder.
5. Calculate your irradiation time using Table 1 and click on 'Move to center' in the MatLab irradiation window.
6. Start timing using a stopwatch when the movement stage stops in the center and click on 'Move to corner' when the appropriate amount of minutes have passed to stop irradiation.
7. Once the irradiation is completed, carefully remove the Mylar dish from the irradiation setup. Add 500 µL PBS in the Mylar dish to 'lift' the coverslip from the Mylar dish and carefully remove the coverslip.
8. Return the coverslip back to the medium. The coverslip can now be used for further experimentation.

EXPECTED RESULTS

The described protocol has been validated using both clonogenic survival (whole dish irradiation) and super resolution microscopy (coverslip irradiation). By irradiating U2OS cells with alpha-particle and X-ray irradiation we compared the differences in cell survival and the differences in 53BP1 immunohistochemistry labeling.

Mylar Dish Irradiation for Clonogenic Survival

Using point-source irradiation allows in-depth analysis of DSBs induced by alpha particles while field-irradiation will allow experiments on larger number of cells for colony survival or immunoblotting. A great difficulty for alpha particle irradiation is to assure that every cell has received the same dose. Our field-irradiation set up has been designed to possibly counter this problem. For validation of the Mylar dish irradiation a comparison of survival was made between X-ray or alpha particle irradiated samples. Alpha particle irradiated was done as described in this protocol. X-ray irradiation was done using the RS320 (Xstrahl Life Sciences, Surrey, United Kingdom), a selfcontained cabinet, with a dose rate of 1.6554 Gy/min. Alpha particle irradiated cells showed severe decreased survival compared to X-ray irradiation cells (Figure 4). This severe effect confirms the effectiveness of the alpha particle irradiation protocol on cells growing on Mylar. In addition, assays showed low variation between three independent experiments.

Coverslip Irradiation for Super Resolution Microscopy

The imaging of cells affected by alpha particle irradiation can be done by conventional epifluorescent microscopes, but advanced confocal and super-resolution imaging techniques could

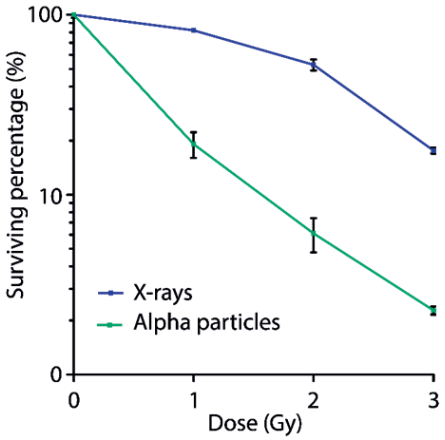

Figure 4. Clonogenic survival curve for U2OS cells irradiated using the alpha particle irradiation or X-rays. U2OS cells were seeded in Mylar dishes and treated with 1, 2 or 3 Gy of irradiation using both alpha particles or X-ray. Cells were trypsinized and seeded in triplicate. Colonies allowed to grow for 7 days (n = 3).

provide more information. Due to the fact that DSBs induced by alpha particles could be present in multiple focus planes, we recommend acquiring 3D-images of affected cells to fully grasp the biological impact of alpha particles. Due to the possibility to use glass cover-slips, super resolution microscopy can be realized. To validate the irradiation of cells grown on glass coverslips, the DSB marker 53BP1 was used to investigate the differences between alpha particle and X-ray induced DSBs. After irradiation 53BP1 was marked using immunofluorescence and samples were imaged using SIM for detailed analysis (Figure 5). SIM imaging was performed on a Zeiss Elyra PS1 microscopy with an Andor iXon DU 885 EMCCD camera (Carl Zeiss AG, Oberkochen, Germany). The raw images were reconstructed into a high-resolution 3D-dataset using the Zeiss 2012 PS1 ZEN software. Reconstruction was done using default settings. 53BP1 foci showed similar structures in both alpha particle (Figure 5A) and X-ray irradiated samples (Figure 5B). In addition, quantification of the foci area revealed larger 53BP1 foci in alpha particle irradiated cells compared to X-ray irradiated cells (Figure 5C). These results show confirmation of cells irradiated by alpha-particles using the described protocol.

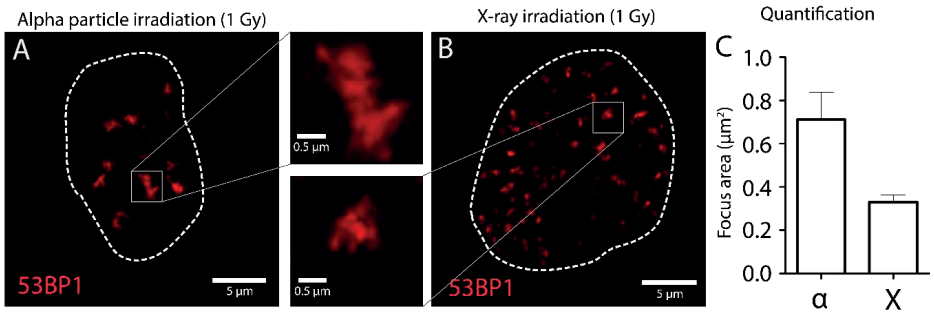

Figure 5. Nanoscopic analysis of DSBs in U2OS cells. U2OS are irradiated using external alpha particle irradiation (**A**) or X-ray (**B**), fixed after 1 h and stained for 53BP1 as DSB marker. SIM imaging was used for nanoscopic analysis of 53BP1 foci. Foci were quantified using ImageJ (**C**). Enlarged figures show 53BP1 foci in close up.

Supplemental Materials: The following are available online; Design S1: Metal frame, Design S2: Culture dish holder, Design S3: Collimator and the MatLab script

Author Contributions: Conceptualization, S.J.R., J.E.; Methodology, S.J.R., J.J.M.K. and J.E.; Software, J.J.M.K; Validation, S.J.R. and J.J.M.K.; Formal analysis, S.J.R. and J.J.M.K.; Investigation, S.J.R. and J.J.M.K.; Resources, S.J.R. and J.J.M.K.; Data curation, S.J.R.; Writing—original draft preparation, S.J.R.; Writing—review and editing, S.J.R., J.J.M.K., J.E., R.K. and A.G.D.; Visualization, S.J.R.; Supervision, J.E., R.K. and A.G.D.

Funding: This research was funded by STW, grant number: 13577.

Acknowledgments: We would like to thank Pim van den Bersselaar and Irene van den Bent for their help validating this protocol.

Conflicts of Interest: The authors declare no conflict of interest.

REFERENCES

1. Task Group on Radiation Quality Effects in Radiological Protection, C.o.R.E.I.C.o.R.P. Relative biological effectiveness (RBE), quality factor (Q), and radiation weighting factor (w(R)). A report of the International Commission on Radiological Protection. *Ann. ICRP*. **2003**, *33*, 1– 117.
2. Pouget, J.P.; Navarro-Teulon, I.; Bardiès, M.; Chouin, N.; Cartron, G.; Pèlegrin, A.; Azria, D. Clinical radioimmunotherapy--the role of radiobiology. *Nat. Rev. Clin. Oncol.* **2011**, *8*, 720– 734.
3. Willers, H.; Allen, A.; Grosshans, D.; McMahon, S.J.; von Neubeck, C.; Wiese, C.; Vikram, B. Toward A variable RBE for proton beam therapy. *Radiother. Oncol.* **2018**, *128*, 68–75.
4. Aten, J.A.; Stap, J.; Krawczyk, P.M.; van Oven, C.H.; Hoebe, R.A.; Essers, J.; Kanaar, R. Dynamics of DNA double-strand breaks revealed by clustering of damaged chromosome domains. *Science*, **2004**, *303*, 92–95.
5. de Kruijff, R.; Wolterbeek, H.; Denkova, A. A Critical Review of Alpha Radionuclide TherapyHow to Deal with Recoiling Daughters? *Pharmaceuticals*, **2015**, *8*, 321–336.
6. Dekempeneer, Y.; Keyaerts, M.; Krasniqi, A.; Puttemans, J.; Muyldermans, S.; Lahoutte, T.; D'huyvetter, M.; Devoogdt, N. Targeted alpha therapy using short-lived alpha-particles and the promise of nanobodies as targeting vehicle. *Expert. Opin. Biol. Ther.* **2016**, *16*, 1035–1047.
7. Kratochwil, C.; Bruchertseifer, F.; Giesel, F.L.; Weis, M.; Verburg, F.A.; Mottaghy, F.; Kopka, K.; Apostolidis, C.; Haberkorn, U.; Morgenstern, A. 225Ac-PSMA-617 for PSMA-Targeted alpha-Radiation Therapy of Metastatic Castration-Resistant Prostate Cancer. *J Nucl Med*, **2016**, *57*, 1941–1944.
8. Pandya, D.N.; Hantgan, R.; Budzevich, M.M.; Kock, N.D.; Morse, D.L.; Batista, I.; Mintz, A.; Li, K.C.; Wadas, T.J. Preliminary Therapy Evaluation of (225)Ac-DOTA-c(RGDyK) Demonstrates that Cerenkov Radiation Derived from (225)Ac Daughter Decay Can Be Detected by Optical Imaging for In Vivo Tumor Visualization. *Theranostics,* **2016**, *6*, 698–709.
9. Inkret, W.C.; Eisen, Y.; Harvey, W.F.; Koehler, A.M.; Raju, M.R. Radiobiology of alpha particles. I. Exposure system and dosimetry. *Radiat. Res.* **1990**, *123*, 304–310.
10. Goodhead, D.T.; Bance, D.A.; Stretch, A.; Wilkinson, R.E. A versatile plutonium-238 irradiator for radiobiological studies with alpha-particles. *Int. J. Radiat. Biol.* **1991**, *59*, 195–210.
11. Metting, N.F.; Koehler, A.M.; Nagasawa, H.; Nelson, J.M.; Little, J.B. Design of a benchtop alpha particle irradiator. *Health. Phys*. **1995**, *68*, 710–715.
12. Zarris, G.; Georgakilas, A.G.; Sakelliou, L.; Sarigiannis, K.; Sideris, E.G. alpha and gammairradiation of aqueous DNA solutions. *Radiat. Meas.* **1998**, *29*, 611–617.
13. Soyland, C.; Hassfjell, S.P. A novel 210Po-based alpha-particle irradiator for radiobiological experiments with retrospective alpha-particle hit per cell determination. *Radiat. Environ. Biophys*. **2000**, 39, 125–130.
14. Søyland, C.; Hassfjell, S.P.; Steen, H.B. A new alpha-particle irradiator with absolute dosimetric determination. *Radiat. Res.* **2000**, *153*, 9–15.
15. Neti, P.V.S.V.; De Toledo, S.M.; Perumal, V.; Azzam, E.I.; Howell, R.W. A multi-port low-fluence alpha-particle irradiator: Fabrication, testing and benchmark radiobiological studies. *Radiat. Res*. **2004**, *161*, 732–738.
16. Gaillard, S.; Pusset, D.; De Toledo, S.M.; Fromm, M.; Azzam, E.I. Propagation distance of the alphaparticle-induced bystander effect: The role of nuclear traversal and gap junction communication. *Radiat. Res*. **2009**, *171*, 513–520.
17. Esposito, G.; Antonelli, F.; Belli, M.; Campa, A.; Simone, G.; Sorrentino, E.; Tabocchini, M.A. An alpha-particle irradiator for radiobiological research and its implementation for bystander effect studies. *Radiat. Res*. **2009**, *172*, 632–642.

18. Seideman, J.H.; Stancevic, B.; Rotolo, J.A.; McDevitt, M.R.; Howell, R.W.; Kolesnick, R.N.; Scheinberg, D.A. Alpha Particles Induce Apoptosis through the Sphingomyelin Pathway. *Radiat. Res.* **2011**, *176*, 434–446.
19. Babu, J.; Shinde, S.G.; Kumar, S.; Ali, M.; Vasumathy, R.; Kumar, A.; Kolekar, R.V.; Kumar, M.; Nema, P.K.; Bhagwat, P.V. et al. Dosimetry and radiobiological studies of automated alpha-particle irradiator. *J. Environ. Pathol. Toxicol. Oncol.,* **2013**, *32*, 263–273.
20. Lee, K.M.; Lee, U.S.; Kim, E.H. A practical alpha particle irradiator for studying internal alpha particle exposure. *Appl. Radiat. Isot*. **2016**, *115*, 304–311.
21. Nawrocki, T.; Tritt, T.C.; Neti, P.V.; Rosen, A.S.; Dondapati, A.R.; Howell, R.W. Design and testing of a microcontroller that enables alpha particle irradiators to deliver complex dose rate patterns. *Phys. Med. Biol.* **2018**, *63*, 245022.
22. Thompson, J.M.; Elliott, A.; D'Abrantes, S.; Sawakuchi, G.O.; Hill, M.A. Tracking down AlphaParticles: The Design, Characterisation and Testing of a Shallow-Angled Alpha-Particle Irradiator. *Radiat. Prot. Dosim.* **2019**, *183*, 264-269.
23. Stap, J.; Krawczyk, P.M.; Van Oven, C.H.; Barendsen, G.W.; Essers, J.; Kanaar, R.; Aten, J.A. Induction of linear tracks of DNA double-strand breaks by alpha-particle irradiation of cells. *Nat. Methods*. **2008**, *5*, 261–266.
24. Kouwenberg, J.J.M.; de Pooter, J.A.; Wolterbeek, H.T.; Denkova, A.G.; Bos, A.J.J. Alpha radiation dosimetry using Fluorescent Nuclear Track Detectors. *Radiat. Meas.,* **2018**, *113*, 25– 32.
25. Kouwenberg, J.J.M.; Wolterbeek, H.T.; Denkova, A.G.; Bos, A.J.J. Fluorescent nuclear track detectors for alpha radiation microdosimetry. *Radiat. Oncol*. **2018**, *13*, 107.
26. Krawczyk, P.M.; Eppink, B.; Essers, J.; Stap, J.; Rodermond, H.; Odijk, H.; Zelensky, A.; Bree, C.V.; Stalpers, L.J.; Buist, M.R. Mild hyperthermia inhibits homologous recombination, induces BRCA2 degradation, and sensitizes cancer cells to poly (ADP-ribose) polymerase-1 inhibition. *Proc. Natl. Acad. Sci. U. S. A.* **2011**, *108*, 9851–9856.
27. Nilsson, J.; Bauden, M.P.; Nilsson, J.M.; Strand, S.E.; Elgqvist, J. Cancer Cell Radiobiological Studies Using In-House-Developed alpha-Particle Irradiator. *Cancer. Biother. Radiopharm.* **2015**, *30*, 386–394.
28. Sigal, Y.M.; Zhou, R.; Zhuang, X. Visualizing and discovering cellular structures with superresolution microscopy. *Science*. **2018**, *361*, 880–887.
29. Stap, J.; Van Marle, J.; Van Veen, H.A.; Aten, J.A. Coating of coverslips with glow-discharged carbon promotes cell attachment and spreading probably due to carboxylic groups. *Cytometry*. **2000**, *39*, 295–299.

4

Comparison of High- and Low-LET Radiation-Induced DNA Double-Strand Break Processing in Living Cells

Stefan J. Roobol [1,2,3], Irene van den Bent [1], Wiggert A. van Cappellen [4], Tsion E. Abraham [4], Maarten W. Paul [1], Roland Kanaar [1,2], Adriaan B. Houtsmuller [4], Dik C. van Gent [1,2] and Jeroen Essers [1,5,6,*]

[1]Department of Molecular Genetics, Erasmus University Medical Center, 3015 GD Rotterdam, The Netherlands

[2]Oncode Institute, Erasmus University Medical Center, 3015 GD Rotterdam, The Netherlands

[3]Department of Radiology & Nuclear Medicine, Erasmus University Medical Center, 3015 GD Rotterdam, The Netherlands

[4]Optical Imaging Center (OIC), Erasmus University Medical Center, 3015 GD Rotterdam, The Netherlands

[5]Department of Vascular Surgery, Erasmus University Medical Center, 3015 GD Rotterdam, The Netherlands

[6]Department of Radiation Oncology, Erasmus University Medical Center, 3015 GD Rotterdam, The Netherlands

*****Correspondence: j.essers@erasmusmc.nl;*

Int. J. Mol. Sci. 2020, 21, 6602

ABSTRACT

High-linear-energy-transfer (LET) radiation is more lethal than similar doses of low-LET radiation types, probably a result of the condensed energy deposition pattern of high-LET radiation. Here, we compare high-LET α-particle to low-LET X-ray irradiation and monitor double-strand break (DSB) processing. Live-cell microscopy was used to monitor DNA double-strand breaks (DSBs), marked by p53-binding protein 1 (53BP1). In addition, the accumulation of the endogenous 53BP1 and replication protein A (RPA) DSB processing proteins was analyzed by immunofluorescence. In contrast to α-particle-induced 53BP1 foci, X-ray-induced foci were resolved quickly and more dynamically as they showed an increase in 53BP1 protein accumulation and size. In addition, the number of individual 53BP1 and RPA foci was higher after X-ray irradiation, while focus intensity was higher after α-particle irradiation. Interestingly, 53BP1 foci induced by α-particles contained multiple RPA foci, suggesting multiple individual resection events, which was not observed after X-ray irradiation. We conclude that high-LET α-particles cause closely interspaced DSBs leading to high local concentrations of repair proteins. Our results point toward a change in DNA damage processing toward DNA end-resection and homologous recombination, possibly due to the depletion of soluble protein in the nucleoplasm. The combination of closely interspaced DSBs and perturbed DNA damage processing could be an explanation for the increased relative biological effectiveness (RBE) of high-LET α-particles compared to X-ray irradiation.

Keywords: DNA double-strand breaks; high linear energy transfer; alpha particles; homologous recombination; live-cell microscopy; nonhomologous DNA end-joining

INTRODUCTION

Double-strand breaks (DSBs) are considered the most dangerous type of DNA damage, as they lead to cell death or mutations if left unrepaired [1]. Recognition of DSBs is the first step toward repair. The first response of the cell is to initiate a highly complex DNA damage response (DDR), in which lesions are identified and marked, thereby initiating DNA repair pathways [2,3]. Activation of DNA repair pathways involves the modification of histones, leading to specific histone marks. This information eventually results in chromatin remodeling [4]. As a result, the histone modifications flanking the DSB are expanded, which leads to the recruitment of DNA damage response proteins like p53-binding protein 1 (53BP1), which can be visualized as nuclear foci [5]. The accumulation of 53BP1 requires the direct recognition of a DSB-specific histone code (H4-K20me2 [6]) and can, therefore, be used as a surrogate marker for DSBs. In addition, 53BP1 influences the DNA repair pathway choice by antagonizing long-range DNA end-resection [4].

There are two major pathways by which DSBs can be repaired, nonhomologous end-joining (NHEJ) and homologous recombination (HR) [7], each of which comprises a number of subpathways. The most direct way to repair DSBs is via the NHEJ pathway, which is active throughout the cell cycle. After DSBs are recognized, DNA ends are processed and eventually rejoined by DNA ligase IV [8]. In the S/G2 phases of the cell cycle, HR is active as an additional repair mechanism. In these phases of the cell cycle, the sister chromatid serves as a template for repair [9]. During HR, the DSB ends are resected by 5'–3' exonucleases, and single-stranded DNA is stabilized by RPA [10]. Replacement with recombination protein RAD51 facilitates the search for the homologous sister chromatid and error-free repair [11,12].

Different DSB repair pathways have evolved because not all breaks are equal, with the difference between the repair of one-ended and two-ended breaks being the most obvious; however, the chemical nature of DNA ends also demands different end-processing factors [7]. By altering radiation types, this difference can be assessed [13]. Differences in ionizing radiation (IR)-induced DSBs are mostly the result of radiation with high or low linear energy transfer (LET). The LET of IR describes the amount of energy which is deposited per unit of length in the material it passes through, for example, tissue [14]. X-ray and gamma irradiation are characterized by a low-LET, inducing sparse and mostly single-strand DNA breaks (SSBs). In contrast, high-LET α-particles or heavy ions result in very localized DNA damage containing a large amount of DSBs [15–18]. The difference in LET has a direct effect on the DDR of the treated cells. High-LET IR mostly induces fewer but larger DSB foci per unit of dose, suggesting multiple DSBs in one focus [19]. In addition, the nuclear DSB focus resolution is slow after high-LET IR compared to low-LET IR, indicating that DSBs are processed in a different way and/or with different kinetics [20,21].

Most current knowledge was gathered in formaldehyde-fixed cells and immunostaining of DSB foci at various time-points. However, fixed samples provide limited options to obtain information regarding the spatial-temporal behavior of individual DSB foci. The implementation

of live-cell imaging overcomes these limitations [19,22–25]. Dynamic live-cell imaging offers a more dynamic view of DSB processing, including the mobility of surrounding chromatin [26].

A previous study showed that α-particle-induced 53BP1 foci are more persistent and larger, and show high mobility compared to X-ray irradiation-induced 53BP1 foci [19]. To determine the kinetics and mechanism of DSB processing after high-LET α-particle irradiation compared to low-LET X-ray irradiation, we repeated the experiment, increased the timeframe, and investigated DSB repair protein behavior. We observed 53BP1 foci disappearing within a few hours after X-ray irradiation, and the remaining foci showed an increase in size and intensity. In contrast, α-particle-irradiated cells showed mainly persistent foci, and remaining foci did not show any changes in size or intensity. In addition, by combining immunostaining for 53BP1 and RPA (indicative for resection), we found that α-particle-induced foci contained multiple DSBs that tend to have a relatively high probability of resection.

RESULTS

Focus Segmentation for Comparison of DSB Processing between High- and Low-LET Irradiation

To study the progression of DSB foci over time, live-cell microscopy provides an abundance of information compared to fixed time-point analysis, such as real-time mobility [25]. Using U2OS cells which stably expressed 53BP1-GFP, we analyzed 53BP1-GFP focus dynamics after irradiation with X-rays or α-particles. Irradiated cells were imaged using confocal microscopy. Images were taken 20 min apart over a 17 h time period post irradiation. These image sequences were subjected to an image processing pipeline to extract the real-time changes of 53BP1-GFP foci.

First, cell nuclei were segmented and subjected to a stabilizing correction to compensate for any changes in nucleus orientation or shape. This ensured analysis of focus dynamics independent of cellular movement (Movie S1). Subsequently, images were further processed by separating neighboring foci, using the watershed tool in ImageJ (see Section 4). This provided a dataset of single 53BP1-GFP foci, which could be followed over time (Figure 1A).

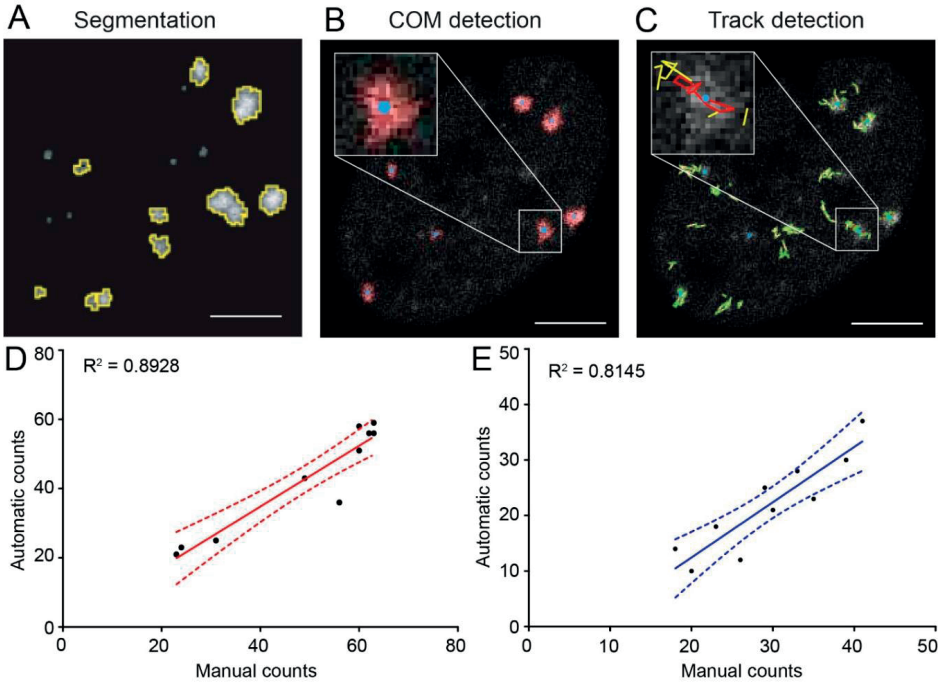

Figure 1. Overview of focus segmentation and focus track analysis. U2OS cells stably expressing p53-binding protein 1 (53BP1)-GFP were irradiated with 2 Gy of α-particle or X-ray irradiation. (**A**) ImageJ scripts were using for focus segmentation. (**B**) Center of mass (COM) per focus was calculated. (**C**) Center of mass was linked to consecutive frames (if COM was ≤0.7 μm). Tracks are indicated in red (active track at this time-point) or yellow (past track not active at this time-point). Scale bar indicates 5 μm. Segmentation of foci was correlated to manual counts of foci for both α-particle irradiation (**D**) and X-ray irradiation (**E**). For both treatments, three nonconsecutive frames were counted in 10 random nuclei. The averages of these counts are shown.

The segmentation of foci in each consecutive frame allowed tracking of individual 53BP1-GFP foci in time. With the use of an algorithm, on the basis of a threshold of 0.7-μm change, the individual foci were linked together between consecutive frames, which formed focus tracks in time. The linking process was based on the distance between the center of mass (COM) points of the focus in consecutive frames (Figure 1B,C). Focus tracks generated from α-particle-irradiated and X-ray-irradiated cells were analyzed. In order to evaluate the quality of our segmentation method, we analyzed the correlation between manual and script-based counting measurements of 10 random cell nuclei. The correlation plots showed good correlation for α-particle-irradiated cells (R^2 = 0.89) and X-ray-irradiated cells (R^2 = 0.82) (Figure 1D,E). Using this newly developed semi-automated analysis, we compared the DSB processing dynamics, marked by 53BP1-GFP, of α-particle-irradiated cells with X-ray-irradiated cells.

α-Particle-Induced 53BP1-GFP Foci Are Slowly Resolved

The formation and resolving of 53BP1 foci can be used as a surrogate marker to determine the kinetics of DSB repair [4]. To investigate the kinetics of DSB repair in live cells, we analyzed focus tracks to measure how individual foci appeared or disappeared and changed position, size, or intensity after irradiation. First, by measuring how many foci are present at certain time-points, we determined the number of foci per nucleus over time.

At the start of imaging, 15 min after irradiation, both treatments showed a similar number of 53BP1-GFP foci per nucleus. In addition, after both treatments, the number of 53BP1-GFP was significantly higher compared to nontreated cells in which an average of 2.3 ± 0.15 53BP1-GFP foci per nucleus were observed in the investigated timeframe. However, in α-particle-irradiated cells, this number doubled after 2 h to 14 foci per nucleus. In contrast, X-ray-irradiated cells showed a reduction in foci per nucleus from 2 h after irradiation onward down to three foci per nucleus. Moreover, the number of foci per nucleus in α-particle-irradiated cells did not decline until 13 h after irradiation and was significantly higher compared to X-ray-irradiated cells between 200 and 960 min after irradiation (Figure 2A). By following the individual foci over time, we could determine how long a focus was visible after appearance. This was quantified and referred to as the duration of the focus track (Figure 2B). The focus tracks were binned into groups with durations of 20–80, 100–160, 180–240, 260–320, and 340–400 min. We found that, for both treatments, most of the segmented foci were visible between 20 and 80 min. Interestingly, α-particle-irradiated cells had more focus tracks which were observed for a longer time than X-ray-irradiated cells.

The Mobility of 53BP1-GFP Foci Is Similar after High- and Low-LET Irradiation

Increased mobility of chromatin surrounding DNA damage has been reported and was suggested to affect DNA repair [27]. As we observed that DSB focus resolving was different in α-particle-irradiated cells compared to X-ray-irradiated cells, we were interested if chromatin mobility might have been affected as well. To compare chromatin mobility, we directly measured the mobility of 53BP1-GFP foci upon treatment of the cells with the different irradiation qualities. By using the same binned groups as before, we investigated differences between foci which were visible for a short or long period of time.

First, we determined the mean square displacement (MSD) which was plotted per track duration group (Figure 2C–F and Figure S1). The curvature of an MSD plot can indicate whether the mobility of foci is apparent diffusion (linear line) or confined motion (curved plot). We observed no difference in mobility of 53BP1-GFP foci when we compared α-particle-irradiated cells to X-ray-irradiated cells.

The curvature of tracks which were shorter than 100 min showed a linear MSD plot, while tracks which were longer than 100 min showed a curved MSD plot. Moreover, the curvature of MSD plots was more apparent with increasing focus track length (Figure S1).

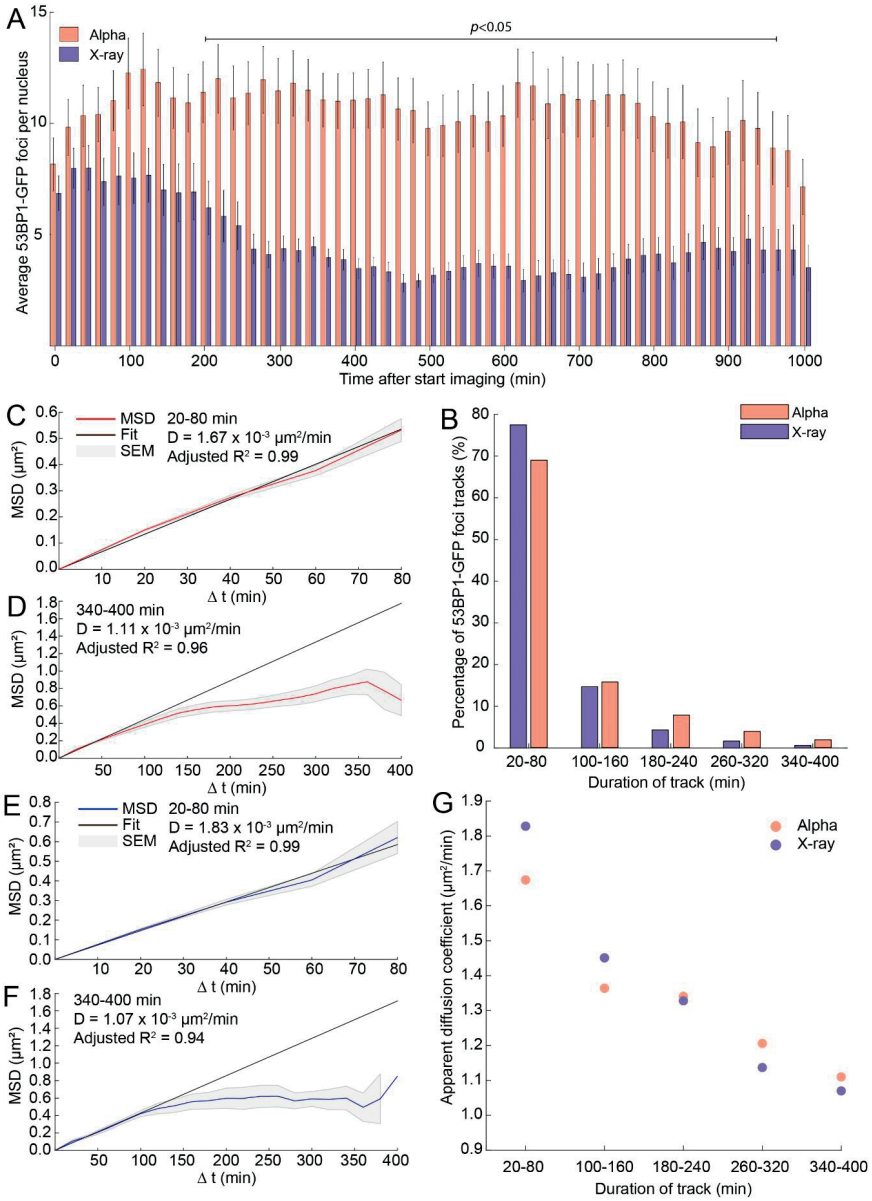

Figure 2. 53BP1-GFP focus resolving after α-particles is slow compared to X-rays. (**A**) Average number of 53BP1-foci per cell over time. Foci in α-particle-irradiated (2 Gy) cells are depicted in red and those in X-ray-irradiated (2 Gy) cells are depicted in blue. All time-points between the indicated bar are significant differences between X-ray- and α-particle-irradiated cells (ANOVA, $p < 0.05$). Error bars indicate the standard error of the mean (SEM). (**B**) Percentage of detected 53BP1-GFP focus tracks that were present in α-particle-irradiated cells (red) or X-ray-irradiated cells (blue) for indicated time. (**C**–**F**) Mean square displacement (MSD) curves of the binned track lengths. α-particle-irradiated cells are depicted using a red line (**C**,**D**) and X-ray-irradiated cells are shown in blue (**E**–**G**). The average apparent diffusion coefficient of 53BP1-GFP foci, which was based on the fit on the first four time intervals.

The slope of MSD curves defines the apparent diffusion coefficient or rate of movement. By fitting all the MSD curves on the first time intervals, we compared the diffusion coefficients between different track lengths. We observed no significant differences in the apparent diffusion coefficient of 53BP1-GFP foci after both treatments (Figure 2G). Interestingly, with increasing track length, the diffusion coefficient declined, showing that foci which were followed for a short time moved faster compared to foci which

were followed for a longer time. These results suggest that there is no significant difference in mobility of 53BP1-GFP foci after X-ray or α-particle irradiation. However, short-lived foci seemed to show more diffusive behavior while long-lived foci showed confined motion.

53BP1-GFP Protein Concentration and Focus Size Increase after X-ray Irradiation

Focus characteristics such as the intensity of 53BP1-GFP and focus size potentially reveal how DSB processing progresses over time [28]. In addition, focus size might give an indication of the extent of DNA damage. Pixel intensity can be used as a measure of the amount of fluorescent molecules, present at sites of DNA damage [29]. Therefore, we calculated the average pixel intensity within 53BP1-GFP foci.

The average pixel intensity of 53BP1-GFP foci showed similar values at the start of imaging, for both treatments. After 400 min, an increase in intensity of 53BP1-GFP foci was observed in X-ray-irradiated cells, but not in α-particle-irradiated cells (Figure 3A). The large difference in focus intensity and increased error bars could have been caused by a change in population distributions of the analyzed foci. Therefore, we generated distribution plots of the average pixel intensity at the start of imaging (0 min), and after 300 min, 600 min, and 900 min (Figure 3B–E). Indeed, we observed a gradual shift toward higher average pixel intensities of foci induced by X-rays (Figure S2). Interestingly, at 900 min after irradiation, two clear populations were present, which did not arise in the α-particle-irradiated cells (Figure 3E).

Average pixel intensity indicates differences in 53BP1-GFP molecules present per volume, but does not reflect the area in which the chromatin might be damaged. Therefore, we analyzed the area of individual foci over time. We observed that X-ray-induced 53BP1-GFP foci showed a sudden growth after 500 min, increasing from 0.8 to 1.3 μm^2 (Figure 3F and Figure S3). Interestingly, the foci in α-particle-irradiated cells were initially larger compared to foci in X-ray-irradiated cells (1.1 vs.

0.8 μm^2), but showed little or no increase in size over time.

The increase in focus size does not necessarily imply that the intensity of 53BP1-GFP increases at a similar rate. For example, when a focus increases in size but no additional 53BP1 is recruited, this focus decreases in average pixel intensity. Indeed, we observed a linear increase in average pixel intensity per focus from the start of imaging after X-ray irradiation, but focus growth only occurred after 500 min. Multiplying the average pixel intensity by the focus area leads to the total amount of 53BP1-GFP present in the focus. Using this parameter, the focus

growth can be related to the corresponding intensity, indicating whether more protein is recruited to the visible focus or not.

The initial amount of 53BP1-GFP per focus was similar for both α-particle- and X-ray-irradiated cells. However, the amount of 53BP1-GFP in X-ray-induced foci showed an increase over time (Figure 3G and Figure S4). For α-particle-induced foci, the amount of 53BP1-GFP showed no change until later than 900 min, where the amount slightly decreased, possibly due to fluorescent bleaching. We conclude that 53BP1-GFP foci increase more in intensity and size after X-ray irradiation than after α-particle irradiation.

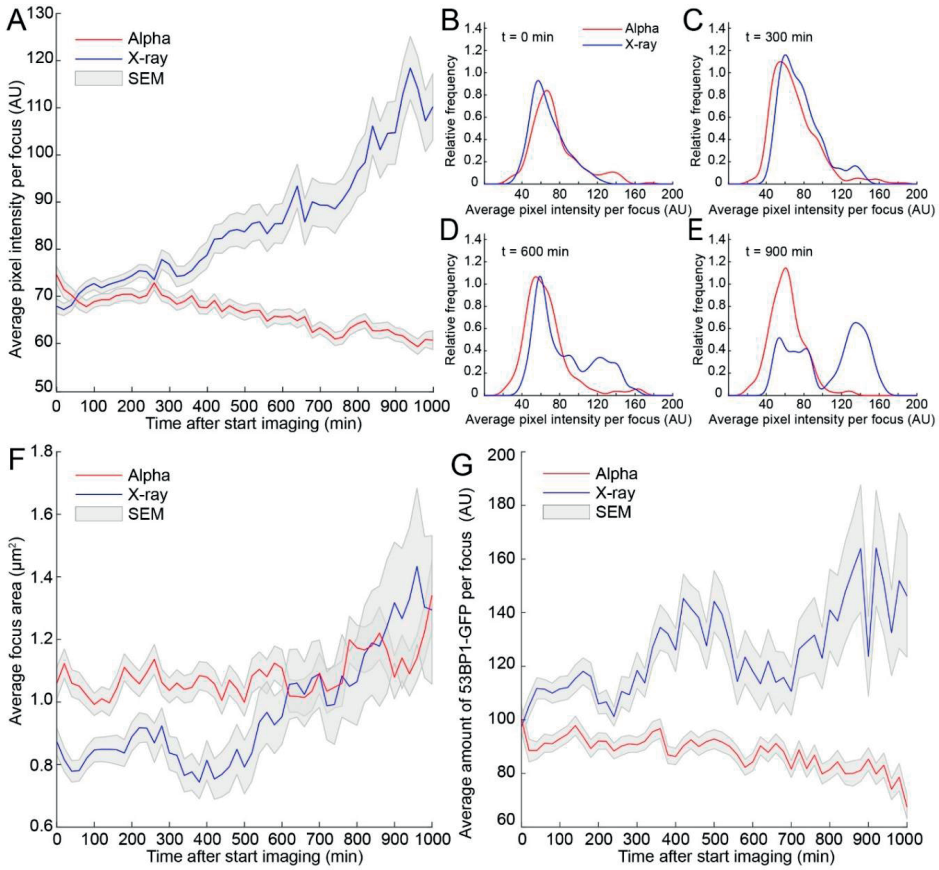

Figure 3. 53BP1-GFP protein accumulation and focus size increase after X-ray irradiation. (**A**) Average 53BP1-GFP intensity per focus (average pixel intensity) over time after treatment using α-particle (red) or X-ray (blue) irradiation (2 Gy). (**B**–**E**) Overview of focus population distribution at 0, 300, 600, and 900 min after the start of imaging. Graphs shown kernel density estimations with the area under the curve being equal to the area of the histogram. The 0 AUs are the consequence of the smoothing procedure used for density estimations. (**F**) Average 53BP1-GFP focus area trough time. The average of foci induced by α-particles (red) or foci induced by X-ray (blue). (**G**) Total amount of 53BP1-GFP (product of focus area and pixel intensity) on foci through time after α-particle (red) or X-ray (blue) irradiation. SEM is indicated in gray.

Dose-Dependent Characteristics of Foci in EdU-Positive Cells after Both Treatments

The differences in foci intensity and size over time after X-ray or α-particles could be related to differences in DNA damage load. Therefore, we performed a dose gradient experiment using both α-particle and X-ray irradiation, ranging from 0.5 to 6 Gy and fixed cells 1 h post irradiation. In addition, to investigate functional protein and minimize the interference of overexpression constructs, cells were stained for endogenous 53BP1 and RPA as markers for DSBs and resection, respectively (Figure 4A,B). Quantification of both 53BP1 and RPA was done by creating a segmentation mask using standard thresholds (see Section 4). The segmentation provided the number of foci, and the signal within the mask could be used to determine the average pixel intensity of a focus.

The number of 53BP1 foci per cell increased in a dose-dependent manner for both treatments (Figure 4C). X-ray irradiation resulted in more 53BP1 foci per cell compared to α-particle-irradiated cells for all doses. Interestingly, 53BP1 focus intensity decreased in a dose-dependent manner after α-particle irradiation compared to little to no change after X-ray irradiation (Figure 4D). Moreover, the intensity of 53BP1 foci was fourfold higher after induction by α-particles than X-rays at a dose of 0.5 Gy.

Subsequently, we investigated the reason for the differences in protein recruitment after α-particle and X-ray irradiation. We considered that different DSB repair pathways might be activated. In addition, the extent of resection at the DNA ends determines what pathway is activated for DSB repair. Therefore, we quantified RPA foci in EdU-positive cells to investigate possible differences in resection events.

In X-ray-irradiated cells the number of RPA foci per cell increased significantly at a dose of 4.5 Gy and higher (Figure 4A,E). In addition, the average RPA focus intensity showed a dose-dependent increase, only at a dose of 4.5 or higher (Figure 4F). This suggests that, at this dose and above, DSBs seemed to be more susceptible to resection after X-ray irradiation. Interestingly, after α-particle irradiation, the number of RPA foci per cell did not increase until the dose of 5.5 Gy (Figure 4E). However, the average RPA intensity of foci induced by α-particles showed an increase at 4 Gy, the dose at which the number of foci increased in X-ray irradiated cells (Figure 4F).

The high accumulation of 53BP1 and RPA protein in a single focus after α-particle irradiation suggests that there is more extensive resection or that multiple DNA ends are present in one focus.

α-Particle-Induced 53BP1 Foci Show Multiple Individual Resection Events

Subsequently, we investigated whether the observed RPA foci colocalized with the 53BP1 foci. The location of RPA and 53BP1 foci showed differences after α-particle or X-ray irradiation (Figure 5A). RPA foci induced by X-rays did not colocalize with 53BP1 foci and appeared mutually exclusive, while, after α-particle irradiation, we observed mixed 53BP1/RPA foci. To quantify

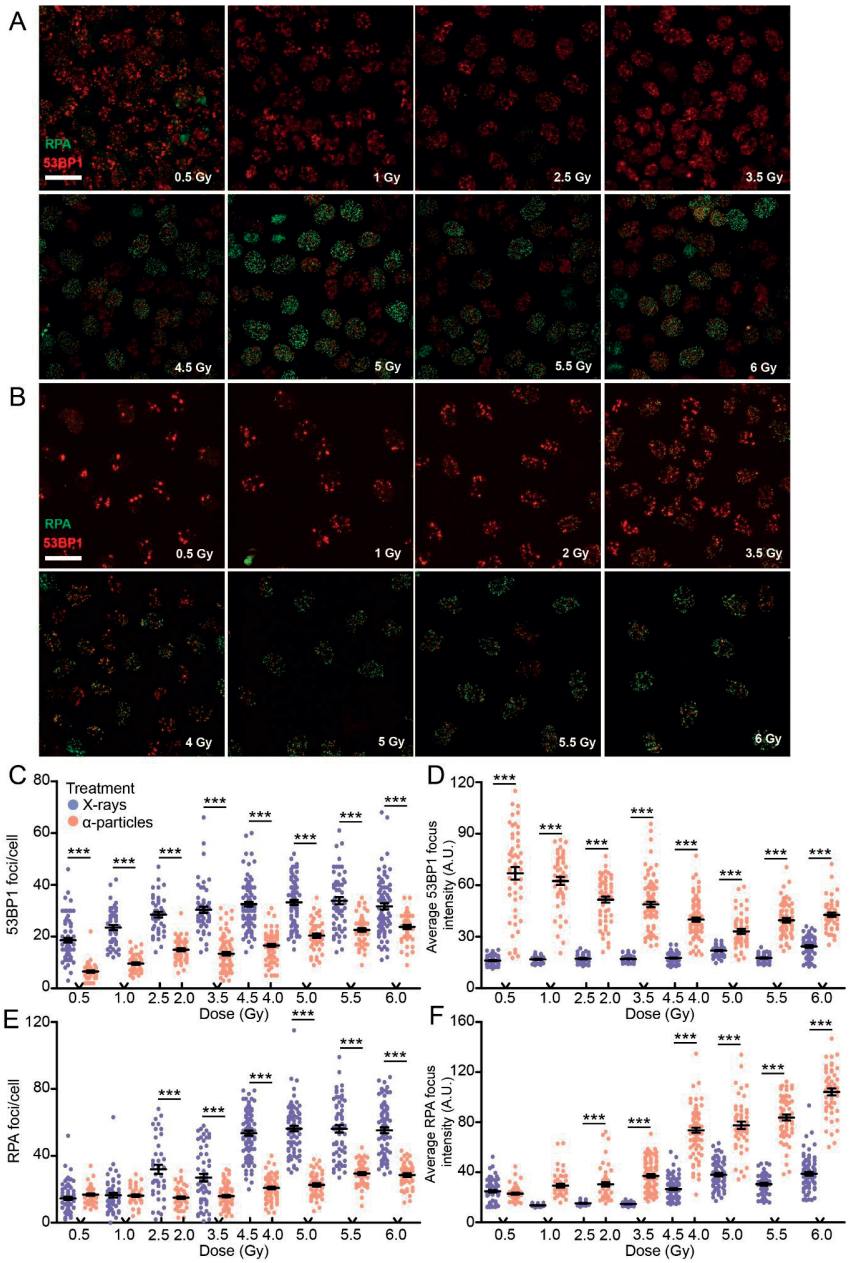

Figure 4. Focus kinetics of 53BP1 and RPA are dose- and radiation type-dependent. Overview of 53BP1 and RPA staining after X-ray (**A**) and α-particle (**B**) irradiation using a dose gradient. Cells were fixed 1 h after irradiation. Quantification of 53BP1 foci per EdU-positive cell (**C**) and intensity (**D**). Quantification of RPA foci per EdU-positive cell (**E**) and intensity (**F**). More than 100 EdU-positive cells were analyzed in two independent experiments. Data points in the plot indicate single nuclei treated with X-ray irradiation (purple) or α-particles (orange). Error bars indicate SEM. Black bars indicate the mean. The statistical differences are indicated by asterisks (***, $p < 0.001$) and determined by ANOVA followed by Tukey's multiple comparison test.

this observation, we used the segmentation mask of 53BP1 foci to measure the pixel intensity of RPA within these foci. The average pixel intensity of RPA colocalizing with 53BP1 foci was significantly higher after α-particle treatment than after X-ray irradiation (Figure 5B).

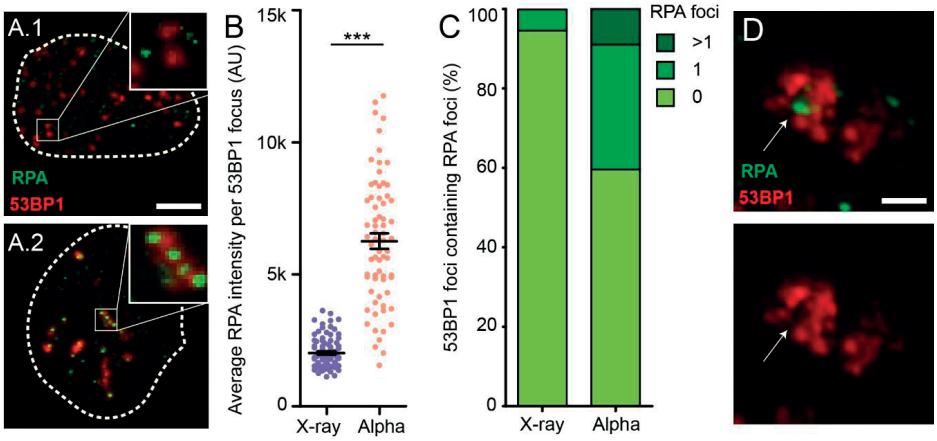

Figure 5. Multiple individual resection events after α-particle irradiation. Representative confocal images of induced 53BP1 and RPA foci by X-ray (**A.1**) or α-particles (**A.2**). Scale bar indicates 5 µm. (**B**) Quantification of RPA focus intensity. (**C**) Percentage of 53BP1 foci colocalizing with 0, 1, or >1 RPA foci. In total, 15 EdU-positive cells were analyzed using structured illumination microscopy for each treatment. (**D**) Representative images of 53BP1 exclusion at RPA foci after α-particle irradiation. Scale bar indicates 0.8 µm. Per assay, >100 EdU positive cells were analyzed. Error bars indicate SEM. The statistical differences are indicated by asterisks (***, $p < 0.001$) and determined by student's *t*-test.

With the use of structured illumination microscopy (SIM), we obtained higher-resolution images, doubled in the *x*-, *y*-, and *z*-axis, to zoom in on individual 53BP1 foci. Using the same segmentation masks of 53BP1 as above, we identified individual RPA foci within a 53BP1 focus. We observed 40% of α-particle-induced 53BP1 foci with one or more colocalizing RPA foci, compared to 5% of the X-ray-induced foci (Figure 5C). Moreover, none of the 53BP1 foci in X-ray-irradiated cells had more than two RPA foci. Notably, the enhanced resolution of SIM revealed exclusion of 53BP1 at RPA foci at the nanoscale level (Figure 5D). These results suggest that multiple individual DNA ends are present in one focus after α-particle irradiation, of which one or more can be resected followed by RPA protein accumulation.

DISCUSSION

Cellular survival is impacted more after receiving high-LET radiation types compared to low-LET radiation. The increased biological effectiveness of high-LET radiation is thought to be the result of the highly condensed energy deposition pattern. To study how cells cope with high- or low-

LET radiation types, we compared α-particle irradiation (high LET) to X-ray irradiation (low LET) using live-cell imaging. We observed differential processing of DSBs after α-particle irradiation compared to X-ray irradiation. Cells treated with α-particles show slow DSB repair and differences in 53BP1-GFP accumulation and focus growth. Endogenous focal accumulation of the proteins 53BP1 and RPA was much higher after α-particles than X-rays. The high accumulation of these markers in α-particle-irradiated cells suggests multiple individual resection events within single DSB foci.

Our observations highlight a substantial difference in DSB processing after X-ray irradiation compared to α-particle irradiation. Employing live-cell imaging to compare α-particle- to X-ray-irradiated cells revealed large differences in the processing of 53BP1-GFP foci. We found that foci induced by α-particles (a) are eliminated more slowly compared to X-ray-induced foci, (b) show no average pixel intensity increase over time, in contrast with X-ray-induced foci, (c) are initially larger than X-ray-induced foci but show no increase in size, which is prominent in X-ray induced foci, and (d) accumulate larger amounts of 53BP1-GFP in foci than X-ray-induced foci.

The repair of induced DSBs in α-particle-irradiated cells appears to be minimal and slow, while X-ray-induced DSBs are repaired quickly, most likely via NHEJ [30]. However, repair via NHEJ can be divided into a fast (in euchromatin) and slow (in heterochromatin) component [31,32]. The slow component of NHEJ repair involves local chromatin decondensation, regulated by factors such as 53BP1, ATM, and KAP-1 [18,31,33].

Chromatin decondensation could be the factor which causes a delay in DSB processing, which we observed after X-ray irradiation (Figure 3F). Additionally, chromatin decondensation could widen the area around DSBs, a possible explanation for 53BP1 focus size increase. Interestingly, during DSB focus enlargement, we observed an increase in 53BP1-GFP intensity per focus. This is contradictory to our argument of chromatin widening, which would be expected to result in a dilution of GFP signal. However, this is not necessarily true; fast resolution of 53BP1 foci in the early phase of DSB repair would result in increasing free 53BP1 in the nucleus, which could then relocate to the remaining slowly repaired DSBs, thereby increasing focus intensity. Indeed, we observed an increase in the total amount of 53BP1-GFP per focus in X-ray-irradiated cells, suggesting relocalization of 53BP1-GFP (Figure 3G).

Chromatin condensation and decondensation in response to DNA damage leads to large-scale reorganization of chromatin fibers [26]. The consequence of chromatin (de)condensation is the accessibility of many factors. Additionally, the loosening of chromatin could alter chromatin mobility. Numerous reports showed that DNA damage increases the mobility of chromatin and the induced DSBs, as elaborately reviewed in [26] and [34]. The highly condensed energy pattern of high-LET irradiation reduces efficient DNA repair and causes the chromosomal reorganization to be disrupted [18,35]. Another report showed higher DSB mobility after α-particle irradiation when compared with X-ray irradiation, using similar live-cell techniques to those in our study [19]. We observed no apparent difference in chromatin mobility between α-particle or X-ray irradiation. A possible explanation could be the difference between the 20-min interval

(this report) and the 1-min interval [19]. Chromatin motion at different time scales can be different [36]. Therefore, comparing 20-min intervals to 1-min intervals would not be correct. To compare DSB mobility in our setting to other mobility studies within the chromatin, we should consider shorter time intervals. The difficulty lies in keeping the possibility to image for several hours; 1-min intervals for several hours could induce photo bleaching. A possible

way to overcome this difficulty is to capture multiple frames with a short interval, every so often. This would capture the mobility of DSB foci whilst keeping the possibility to image for several hours.

We observed that most 53BP1 foci disappeared in time after X-ray irradiation, but not after α-particle irradiation, suggesting that high-LET DSBs are not repaired in the timeframe (17 h) of this experiment. The remaining question relates, therefore, to the cause of this delay of focus resolving compared to X-ray-induced damage.

Clustered or complex DNA damage is suggested to be an important cause of the increased biological effectiveness of high-LET radiation, and both terms are used to describe multiple types of DNA damage in close vicinity [17,37–39]. We observed multiple independent resection events, marked by RPA, localizing to single 53BP1 foci. These structures are best described as “closely interspaced DSBs”, leading to increased biological effectiveness when not properly repaired [23,40]. Indeed, super-resolution techniques previously uncovered “nanoclusters” in previously thought single DSB foci [37]. Closely interspaced DSBs would explain why we observed a relatively low number of 53BP1 and RPA foci, which have in turn high intensity. In addition, we could speculate that closely interspaced DSBs cause hyper-resection, causing a lack of repair in the G1 phase with no HR factors available, leading to persistent DSBs. Another possibility in G1 phase would be slow resection-dependent NHEJ, leading to microhomology-mediated end-joining [41].

53BP1 is active in a delicate balancing act to regulate the extent of resection in the S and G2 phases of the cell cycle. 53BP1 pool depletion by high-dose X-ray irradiation would limit the DNA end protection and lead to increased DNA resection [42,43]. Indeed, we found that the number and intensity of RPA foci increased with increasing X-ray dose, indicating that more resected DNA is present. In addition, 53BP1 intensity decreased with increasing α-particle dose, mimicking the 53BP1 depletion at high X-ray dose. The 53BP1 depletion is suggested to be caused by an abundance of DSBs, causing insufficient 53BP1 binding. Interestingly, the retention of 53BP1 is efficient up to 20–40 DSBs simultaneously, and exceeding this number may result in failing NHEJ and increased HR-directed repair [44]. Low α-particle dose could reach these numbers due to closely interspaced DSBs as a result of the condensed energy deposition pattern of high-LET radiation. Indeed, 53BP1 foci intensity decreased while RPA intensity increased after α-particle irradiation, suggesting impaired 53BP1 retention leading to resection (Figure 5). Interestingly, we observed a substantial increase in the number of RPA foci at a similar dose for X-ray and α-particle irradiation, suggesting that susceptibility to resection is not radiation type-dependent. However, the high RPA focus intensity after α-particles and

colocalization with 53BP1, which is not observed after X-rays, might be an explanation for the difference in biological effectiveness between X-rays and α-particles.

The discussed results could be summarized in a working model in combination with the recent reports of 53BP1 exhaustion (Figure 6). We argue that the available 53BP1 pool is sufficient after 2 Gy of X-ray irradiation, leading to full coverage of the DNA ends and efficient DSB repair via NHEJ. At the later time-points, most DSBs are repaired, leading to increased numbers of 53BP1 molecules available for growth of the few remaining foci. However, the 53BP1 pool is insufficient at similar α-particle dose due to closely interspaced DSBs, leading to insufficient amounts of 53BP1 to cover all DNA ends, which allows resection. 53BP1 depletion becomes prominent and most DSBs are resected only at higher doses. In the S/G2 phase, this leads to HR-directed repair, whereas, in the G1 phase, repair would result in persistent DSBs.

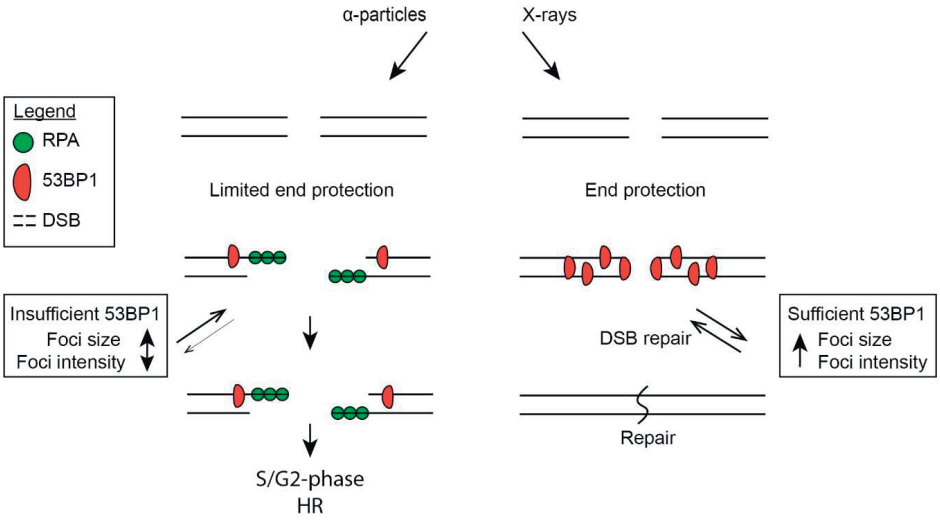

Figure 6. Working model of the role of radiation type in double-strand break (DSB) repair pathway choice. Both X-ray irradiation and α-particle irradiation induce DSBs. The DNA ends induced by X-ray irradiation are protected by 53BP1 and are repaired by the nonhomologous end-joining (NHEJ) machinery. Repair of DSBs reintroduces 53BP1 back into the general pool and causes the remaining foci to recruit more 53BP1, leading to an increase in focus intensity. Repair via the slow component of NHEJ involves chromatin decondensation, leading to focus growth. On the other hand, after α-particle irradiation, the 53BP1 pool is insufficient, thereby limiting end protection and leading to resection. Resection in the S/G2 phase would activate homologous recombination (HR)-directed repair.

In conclusion, our results indicate that the condensed energy deposition pattern of high-LET α-particles induces closely interspaced DSBs. The abundance of multiple DSBs in close vicinity throughout the cell nucleus leads to 53BP1 protein insufficiency and ineffective DNA end protection. This cascade of events might be an explanation of the increased biological effectiveness of high-LET α-particle irradiation, compared to low-LET X-ray irradiation.

MATERIALS AND METHODS

Cell Culture

U2OS cells were cultured in Dulbecco's modified Eagle medium (DMEM) supplemented with 1% penicillin/streptomycin (PS) and 10% fetal calf serum (FCS). Cells were incubated at 37 °C in a water-saturated atmosphere with 5% CO_2. The 53BP1-GFP U2OS cell line was previously described and characterized [45]. In short, full-length m53BP1 was cloned into a pEGFP-C1 vector and transfected into U2OS cells.

X-ray and α-Particle Irradiation

Irradiated cells were cultured on round glass coverslips (diameter: 18 mm). X-ray irradiation was performed using the RS320 (Xstrahl Live Sciences), a self-contained cabinet, with a dose rate of 1.6554 Gy/min and working voltage of 195 kV and 10 mA. Alpha irradiation was performed as described before [46]. In brief, coverslips containing cultured cells were washed with PBS and placed upside down (cells facing down) on a Mylar dish. The Mylar dish was placed in the irradiation set-up with the cells facing down to the ^{241}Am source. The center area of the coverslip was subsequently irradiated using alpha particles passing vertically through the cells, with the requested dose. In this study, the a-particles had an LET of 115 ± 10 keV/µm [47].

Immunofluorescence

Cells were washed with ice-cold PBS 1 h post irradiation. For RPA staining, cells were extracted with cold CSK buffer (10 mM HEPES-KOH, pH 7.9, 100 mM NaCl, 300 mM sucrose, 3 mM $MgCl_2$, 1 mM EGTA, 0.5% (*v*/*v*) Triton X-100) and cold CSS buffer (10 mM Tris, pH 7.4, 10 mM NaCl, 3 mM $MgCl_2$, 1% (*v*/*v*) Tween-20, 0.5% (*w*/*v*) sodium deoxycholate) for 5 min each before fixation in 4% PFA in PBS for 30 min at room temperature. Fixed cells were washed two times in PBS plus 0.1% Triton X-100 and washed 30 min in blocking solution (0.5% BSA plus 0.15% glycine in PBS). Primary rabbit anti-53BP1 (1:1000, Novus Biologicals, Centennial, CO, USA), mouse anti-RPA (1:1000, Calbiochem, San Diego, CA, USA), and mouse anti-γH2AX (1:1000, Millipore, Burlington, MA, USA) antibodies were diluted in blocking solution, and cells were incubated at 4 °C overnight. Hereafter, cells were washed two times for 10 min with PBS plus 0.1% Triton X-100 and washed shortly in blocking solution. Secondary antibodies Alexa Fluor goat anti-rabbit 594 and goat anti-mouse 488 (1:1000, ThermoFisher Scientific, Waltham, MA, USA) were diluted in blocking solution, and cells were incubated for 1 h at room temperature. S-phase cells were detected by EdU incorporation (10 µM, Merck, Darmstadt, Germany). Cells were labeled with EdU 30 min before fixation, which was detected using a Click-IT reaction according to the manufacturer's protocol (Invitrogen, Waltham, MA, USA).

Confocal (Live-Cell) Imaging

To capture the progression of 53BP1-GFP foci, live-cell confocal microscopy was performed using a Leica SP5 confocal microscope. Immediately after irradiation (2 Gy for both X-ray and α-particles), coverslips were placed in a live-cell chamber and filled with prewarmed medium. The live-cell chamber was placed in a PeCon small chamber incubator with 37 °C, 5% CO_2 regulation. Images of randomly selected groups of cells were acquired using a 40× HCX PL APO CS (NA = 1.25) oil objective at an interval of 20 min. GFP signal was detected using a laser line of 488 nm and emission filter of 500–550 nm. Three independent experiments were conducted capturing three distinct groups of cells at every experiment, for both treatments and for non-treated conditions.

To image the stained samples, a Leica SP5 confocal microscope was used. For each experiment, five images were acquired using a 40× HCX PL APO CS objective (NA = 1.25) and the appropriate laser lines and emission filters (DAPI/Atto Azide 390; excitation 405 nm, emission 435–480 nm, Alexa 488; excitation 488 nm, emission 500–550 nm, Alexa 594; excitation 561 nm, emission 570–630 nm). For image analysis, *z*-projections were made. Immunostained 53BP1 and RPA foci were quantified using ImageJ scripts (https://imagej.nih.gov/ij/download.html). In short, EdU-positive cells were segmented using auto-thresholds. Within the segmented nuclei, segmentation masks were made for individual foci using auto-thresholds and the watershed tool [48]. The mean intensity, area, and number of the segmented foci were measured using ImageJ.

Super Resolution Microscopy

Structured illumination microscopy (SIM) imaging was performed on a Zeiss Elyra PS1 with an

Andor iXon DU 885 EMCCD camera (Carl Zeiss AG, Oberkochen, Germany) and 63× Plan Apochromat DIC oil lens (NA = 1.4) using 488- and 561-nm diode lasers with 100-ms exposure times. Samples were illuminated with a spatial line pattern that was shifted in five phases and rotated in five orientations.

The raw images were reconstructed into a high-resolution three-dimensional (3D) dataset using the Zeiss 2012 PS1 ZEN software. RPA foci in SIM images were quantified manually.

Image Processing

Image sequences from live-cell experiments were analyzed in ImageJ using maximum-intensity projections. Using the 53BP1-GFP nuclear signal, cell nuclei were segmented for individual analysis. To minimize the translational and rotational motion of nuclei, a stabilizing correction was used on the basis of rigid body transformations (StackReg plugin by Philippe Thévenaz, Biomedical Imaging Group, Swiss Federal Institute of Technology Lausanne, https://imagej.net/StackReg). Single-image sequences containing single cells were subsequently analyzed to isolate and measure the 53BP1-GFP foci within nuclei. The first timeframe ($t = 0$) image containing the maximum projection of the *z*-stacks was duplicated and Gaussian-blurred with $\sigma = 1$. To segment foci within the nucleus, a lower threshold was manually set on this smoothed image

of the first timeframe (with the upper threshold always being 255). Using the threshold option in ImageJ, an appropriate threshold was chosen, visually comparing an adjustable threshold image to the original input image. A visually accepted threshold led to an automatically calculated factor, depicted in Equation (1).

$$factor = \frac{Manually\ set\ lower\ threshold - Cell\ mean\ intensity\ at\ t = 0}{Cell\ standard\ deviation\ of\ mean\ intensity\ at\ t = 0} \quad (1)$$

The threshold used on each consecutive timeframe ($t \geq 1$) subsequently differed according to Equation (2).

$$Threshold(t) = Cell\ mean\ intensity\ (t) + factor \times Cell\ standard\ deviation\ of\ mean\ intensity\ (t) \quad (2)$$

The factor was held constant for each frame of the same cell but could differ between cells to reach optimal 53BP1-GFP focus segmentation. If 53BP1-GFP foci were adherent due the threshold, the Watershed tool was used for foci separation [48]. The mean intensity, area, and coordinates of the center of mass of the segmented foci were measured using ImageJ.

Image Analysis

An algorithm was developed in MatLab to link individual foci between consecutive timeframes to form a focus track over time. The center of mass from one focus was compared to all the centers of mass from the foci in the consecutive timeframe. Based on the distance between the center of mass of a focus in one timeframe ($t = tn$) and a center of mass of a focus in a subsequent timeframe ($t = tn + 1$), foci were linked through time if the Euclidian distance between the center of masses was below 0.7 µm in two consecutive timeframes.

The track length was calculated based on the time interval used in the live-cell imaging and the number of frames the focus was visible in the track (Equation (3)).

$$Track\ length\ (\mathrm{min}) = (number\ of\ foci\ linked\ in\ track - 1) \times time\ interval\ (= 20\ minutes) \quad (3)$$

This process continued for the total number of timeframes imaged (in this case, 51 frames), equaling 1000 min ($t = 0$ was also a frame). The Matlab code was capable of detecting the splitting or merging of foci if one focus of a timeframe was linked to two distinct foci in the consecutive frame or if two distinct foci from one timeframe linked to the same focus in the

consecutive frame, respectively. Through this process, a total of 2541 foci tracks were formed in 37 cells irradiated by α-particles and 970 foci tracks were formed in 26 cells irradiated by X-rays. Tracks were not allowed to have a gap, i.e., a focus had to be present in every consecutive frame. Additionally, tracks could start or end at any given time point in the image sequence.

Relative frequency plots were fitted by Kernel density estimates using the "fitdist" command in Matlab. The "kernel" option was applied, which fits a kernel to the data of a histogram. A smoothing bandwidth of 6, 0.3, and 220 was used for the kernel density estimations of the 53BP1 signal intensity per focus, focus area, and total 53BP1 on active foci, respectively. The area under the kernel density curve was normalized to be equal to the area of the histogram. The area of the histograms of α-particle- and X-ray-induced foci was scaled to be equal; hence, the areas under the curves were equal.

A normalization factor was determined at $t = 0$ which made the highest peak of the histogram equal to 1, and this normalization factor was applied to each distribution at later time points.

The mean square displacement was calculated via the MSDanalyzer MatLab plugin [49].

Curves were fitted with the "fit" command in MatLab from the curve-fitting toolbox. The typical MSD curve for confined motion was linearly fit on a selected portion of the curve to yield an estimate for the diffusion coefficient D. As confined motion shows only after some time has passed, the first few data points of the MSD curve indicate diffusive motion, i.e., the curve is a straight line. The fit was made on the first four data points for each category.

The mean square displacement for diffusive motion in two dimensions (2D) is given by the Equation (4).

where $d = 2$ is the dimension, and D is the diffusion coefficient.

$$MSD(t) = < r^2 > = \ 2dDt \tag{4}$$

This formula was approximated by the "fit type" command in MatLab, using independent x and dependent y with a fit method of "nonlinear least squares" and a start point in the origin. The approximation formula is shown in Equation (5), where a is calculated by Equation (6).

$$y = f(x) = \ ax \tag{5}$$

$$a = \ 4D \tag{6}$$

This made it possible to calculate the diffusion coefficient directly from the fit as a value for the variable given by Matlab.

Supplementary Materials: Supplementary materials can be found at http://www.mdpi.com/1422-0067/21/18/6602/s1.

Author Contributions: Conceptualization, S.J.R., I.v.d.B., R.K., D.C.G., and J.E.; methodology, S.J.R., I.v.d.B.,
T.E.A., and J.E.; software, I.v.d.B., W.A.v.C., and M.W.P.; validation, S.J.R., I.v.d.B., T.E.A., and M.W.P.; investigation, S.J.R. and I.B.; writing—original draft preparation, S.J.R.; writing—review and editing, I.v.d.B., W.A.v.C., M.W.P., R.K., A.B.H., D.C.v.G., and J.E.; visualization, S.J.R., D.C.v.G., and J.E.; supervision, R.K., A.B.H., D.C.v.G., and J.E. All authors read and agreed to the published version of the manuscript.

Funding: The project was funded by Technologie stichting STW, project number 13577. This research was funded by the Dutch Cancer Society and by the Gravitation program CancerGenomiCs.nl from the Netherlands Organization for Scientific Research (NWO) and is part of the Oncode Institute, which is partly financed by the Dutch Cancer Society.

Acknowledgments: We would like to thank G. van de Kamp and J. Nonnekens for critically evaluating the manuscript.

Conflicts of Interest: The authors declare no conflict of interest.

REFERENCES

1. Shibata, A.; Jeggo, P.A. DNA double-strand break repair in a cellular context. *Clin. Oncol. (R. Coll. Radiol.)* **2014**, *26*, 243–249.
2. Jackson, S.P.; Bartek, J. The DNA-damage response in human biology and disease. *Nature* **2009**, *461*, 1071–1078.
3. Ciccia, A.; Elledge, S.J. The DNA damage response: Making it safe to play with knives. *Mol. Cell* **2010**, *40*, 179–204.
4. Panier, S.; Boulton, S.J. Double-strand break repair: 53bp1 comes into focus. *Nat. Rev. Mol. Cell Bio.* **2014**, *15*, 7–18.
5. Rothkamm, K.; Barnard, S.; Moquet, J.; Ellender, M.; Rana, Z.; Burdak-Rothkamm, S. DNA damage foci: Meaning and significance. *Environ. Mol. Mutagen.* **2015**, *56*, 491–504.
6. Botuyan, M.V.; Lee, J.; Ward, I.M.; Kim, J.E.; Thompson, J.R.; Chen, J.J.; Mer, G. Structural basis for the methylation state-specific recognition of histone h4-k20 by 53bp1 and crb2 in DNA repair. *Cell* **2006**, *127*, 1361–1373.
7. Hoeijmakers, J.H.J. Genome maintenance mechanisms for preventing cancer. *Nature* **2001**, *411*, 366–374.
8. Lieber, M.R. The mechanism of double-strand DNA break repair by the nonhomologous DNA end-joining pathway. *Annu. Rev. Biochem.* **2010**, *79*, 181–211.
9. Wyman, C.; Kanaar, R. DNA double-strand break repair: All's well that ends well. *Annu. Rev. Genet.* **2006**, *40*, 363–383.
10. Chen, H.; Lisby, M.; Symington, L.S. Rpa coordinates DNA end resection and prevents formation of DNA hairpins. *Mol. Cell* **2013**, *50*, 589–600.
11. Liu, J.; Doty, T.; Gibson, B.; Heyer, W.D. Human brca2 protein promotes rad51 filament formation on rpa-covered single-stranded DNA. *Nat. Struct. Mol. Biol.* **2010**, *17*, 1260–1262.
12. Li, J.; Holzschu, D.L.; Sugiyama, T. Pcna is efficiently loaded on the DNA recombination intermediate to modulate polymerase delta, eta, and zeta activities. *Proc. Natl. Acad. Sci. USA* **2013**, *110*, 7672–7677.
13. Goodhead, D.T. Energy deposition stochastics and track structure: What about the target? *Radiat. Prot. Dosim.* **2006**, *122*, 3–15.
14. Danzker, M.; Kessaris, N.D.; Laughlin, J.S. Absorbed dose and linear energy transfer in radiation experiments. *Radiology* **1959**, *72*, 51–61.
15. Aten, J.A.; Stap, J.; Krawczyk, P.M.; Van Oven, C.H.; Hoebe, R.A.; Essers, J.; Kanaar, R. Dynamics of DNA double-strand breaks revealed by clustering of damaged chromosome domains. *Science* **2004**, *303*, 92–95.
16. Eccles, L.J.; O'Neill, P.; Lomax, M.E. Delayed repair of radiation induced clustered DNA damage: Friend or foe? *Mutat. Res. Fundam. Mol. Mech. Mutagenesis* **2011**, *711*, 134–141.
17. Hagiwara, Y.; Niimi, A.; Isono, M.; Yamauchi, M.; Yasuhara, T.; Limsirichaikul, S.; Oike, T.; Sato, H.; Held, K.D.; Nakano, T.; et al. 3d-structured illumination microscopy reveals clustered DNA double-strand break formation in widespread gammah2ax foci after high let heavy-ion particle radiation. *Oncotarget* **2017**, *8*, 109370–109381.
18. Timm, S.; Lorat, Y.; Jakob, B.; Taucher-Scholz, G.; Rube, C.E. Clustered DNA damage concentrated in particle trajectories causes persistent large-scale rearrangements in chromatin architecture. *Radiother. Oncol.* **2018**, *129*, 600–610.

19. Sollazzo, A.; Brzozowska, B.; Cheng, L.; Lundholm, L.; Scherthan, H.; Wojcik, A. Live dynamics of 53bp1 foci following simultaneous induction of clustered and dispersed DNA damage in u2os cells. *Int. J. Mol. Sci.* **2018**, *19*, 519. [CrossRef]
20. Nikitaki, Z.; Nikolov, V.; Mavragani, I.V.; Mladenov, E.; Mangelis, A.; Laskaratou, D.A.; Fragkoulis, G.I.; Hellweg, C.E.; Martin, O.A.; Emfietzoglou, D.; et al. Measurement of complex DNA damage induction and repair in human cellular systems after exposure to ionizing radiations of varying linear energy transfer (let). *Free Radic. Res.* **2016**, *50*, S64–S78.
21. Hada, M.; Georgakilas, A.G. Formation of clustered DNA damage after high-let irradiation: A review. *J. Radiat. Res.* **2008**, *49*, 203–210.
22. Neumaier, T.; Swenson, J.; Pham, C.; Polyzos, A.; Lo, A.T.; Yang, P.; Dyball, J.; Asaithamby, A.; Chen, D.J.; Bissell, M.J.; et al. Evidence for formation of DNA repair centers and dose-response nonlinearity in human cells. *Proc. Natl. Acad. Sci. USA* **2012**, *109*, 443–448.
23. Asaithamby, A.; Chen, D.J. Mechanism of cluster DNA damage repair in response to high-atomic number and energy particles radiation. *Mutat. Res.* **2011**, *711*, 87–99.
24. Jakob, B.; Splinter, J.; Durante, M.; Taucher-Scholz, G. Live cell microscopy analysis of radiation-induced DNA double-strand break motion. *Proc. Natl. Acad. Sci. USA* **2009**, *106*, 3172–3177.
25. Sung, M.H.; McNally, J.G. Live cell imaging and systems biology. *Wiley Interdiscip. Rev. Syst. Biol. Med.* **2011**, *3*, 167–182.
26. Smith, M.J.; Rothstein, R. Poetry in motion: Increased chromosomal mobility after DNA damage. *DNA Repair* **2017**, *56*, 102–108.
27. Krawczyk, P.M.; Borovski, T.; Stap, J.; Cijsouw, T.; ten Cate, R.; Medema, J.P.; Kanaar, R.; Franken, N.A.; Aten, J.A. Chromatin mobility is increased at sites of DNA double-strand breaks. *J. Cell Sci.* **2012**, *125*, 2127–2133.
28. Fernandez-Vidal, A.; Vignard, J.; Mirey, G. Around and beyond 53bp1 nuclear bodies. *Int. J. Mol. Sci.* **2017**, *18*, 2611.
29. Coffman, V.C.; Wu, J.Q. Every laboratory with a fluorescence microscope should consider counting molecules. *Mol. Biol. Cell* **2014**, *25*, 1545–1548.
30. Lees-Miller, S.P.; Meek, K. Repair of DNA double strand breaks by non-homologous end joining. *Biochimie* **2003**, *85*, 1161–1173.
31. Noon, A.T.; Shibata, A.; Rief, N.; Lobrich, M.; Stewart, G.S.; Jeggo, P.A.; Goodarzi, A.A. 53bp1-dependent robust localized kap-1 phosphorylation is essential for heterochromatic DNA double-strand break repair. *Nat. Cell Biol.* **2010**, *12*, 177–184.
32. Goodarzi, A.A.; Jeggo, P.; Lobrich, M. The influence of heterochromatin on DNA double strand break repair: Getting the strong, silent type to relax. *DNA Repair* **2010**, *9*, 1273–1282.
33. Goodarzi, A.A.; Kurka, T.; Jeggo, P.A. Kap-1 phosphorylation regulates chd3 nucleosome remodeling during the DNA double-strand break response. *Nat. Struct. Mol. Biol.* **2011**, *18*, 831–839.
34. Mekhail, K. Defining the damaged DNA mobility paradox as revealed by the study of telomeres, dsbs, microtubules and motors. *Front. Genet.* **2018**, *9*, 95.
35. Lorat, Y.; Timm, S.; Jakob, B.; Taucher-Scholz, G.; Rube, C.E. Clustered double-strand breaks in heterochromatin perturb DNA repair after high linear energy transfer irradiation. *Radiother. Oncol.* **2016**, *121*, 154–161.
36. Mine-Hattab, J.; Recamier, V.; Izeddin, I.; Rothstein, R.; Darzacq, X. Multi-scale tracking reveals scale-dependent chromatin dynamics after DNA damage. *Mol. Biol. Cell* **2017**, *28*, 3323–3332.
37. Scherthan, H.; Lee, J.H.; Maus, E.; Schumann, S.; Muhtadi, R.; Chojowski, R.; Port, M.; Lassmann, M.; Bestvater, F.; Hausmann, M. Nanostructure of clustered DNA damage in leukocytes after in-solution irradiation with the alpha emitter ra-223. *Cancers* **2019**, *11*, 1877.

38. Jezkova, L.; Zadneprianetc, M.; Kulikova, E.; Smirnova, E.; Bulanova, T.; Depes, D.; Falkova, I.; Boreyko, A.; Krasavin, E.; Davidkova, M.; et al. Particles with similar let values generate DNA breaks of different complexity and reparability: A high-resolution microscopy analysis of gammah2ax/53bp1 foci. *Nanoscale* **2018**, *10*, 1162–1179.
39. Carter, R.J.; Nickson, C.M.; Thompson, J.M.; Kacperek, A.; Hill, M.A.; Parsons, J.L. Complex DNA damage induced by high linear energy transfer alpha-particles and protons triggers a specific cellular DNA damage response. *Int. J. Radiat. Oncol. Biol. Phys.* **2018**, *100*, 776–784.
40. Asaithamby, A.; Hu, B.; Chen, D.J. Unrepaired clustered DNA lesions induce chromosome breakage in human cells. *Proc. Natl. Acad. Sci. USA* **2011**, *108*, 8293–8298.]
41. Lobrich, M.; Jeggo, P. A process of resection-dependent nonhomologous end joining involving the goddess artemis. *Trends. Biochem. Sci.* **2017**, *42*, 690–701.
42. Ochs, F.; Somyajit, K.; Altmeyer, M.; Rask, M.B.; Lukas, J.; Lukas, C. 53bp1 fosters fidelity of homology-directed DNA repair. *Nat. Struct. Mol. Biol.* **2016**, *23*, 714–721.
43. Mladenov, E.; Staudt, C.; Soni, A.; Murmann-Konda, T.; Siemann-Loekes, M.; Iliakis, G. Strong suppression of gene conversion with increasing DNA double-strand break load delimited by 53bp1 and rad52. *Nucleic Acids Res.* **2019**, *48*, 1905–1924.
44. Gudjonsson, T.; Altmeyer, M.; Savic, V.; Toledo, L.; Dinant, C.; Grofte, M.; Bartkova, J.; Poulsen, M.; Oka, Y.; Bekker-Jensen, S.; et al. Trip12 and ubr5 suppress spreading of chromatin ubiquitylation at damaged chromosomes. *Cell* **2012**, *150*, 697–709.
45. Bekker-Jensen, S.; Lukas, C.; Kitagawa, R.; Melander, F.; Kastan, M.B.; Bartek, J.; Lukas, J. Spatial organization of the mammalian genome surveillance machinery in response to DNA strand breaks. *J. Cell Biol.* **2006**, *173*, 195–206.
46. Roobol, S.J.; Kouwenberg, J.J.M.; Denkova, A.G.; Kanaar, R.; Essers, J. Large field alpha irradiation setup for radiobiological experiments. *Methods. Protoc.* **2019**, *2*, 75.
47. Kouwenberg, J.J.M.; Wolterbeek, H.T.; Denkova, A.G.; Bos, A.J.J. Fluorescent nuclear track detectors for alpha radiation microdosimetry. *Radiat. Oncol.* **2018**, *13*, 107.
48. Soille, P.; Vincent, L. Determining watersheds in digital pictures via flooding simulations. *P. Soc. Photo Opt. Ins.* **1990**, *1360*, 240–250.
49. Tarantino, N.; Tinevez, J.Y.; Crowell, E.F.; Boisson, B.; Henriques, R.; Mhlanga, M.; Agou, F.; Israel, A.; Laplantine, E. Tnf and il-1 exhibit distinct ubiquitin requirements for inducing nemo-ikk supramolecular structures. *J. Cell Biol.* **2014**, *204*, 231–245.

5

Uptake and subcellular distribution of radiolabeled polymersomes for radiotherapy

Stefan J. Roobol[1,2,3*], Thomas A. Hartjes[4,5*], Johan A. Slotman[5], Robin M. de Kruijff[6], Guzman Torrelo[6], T.E. Abraham[4,5], Frank Bruchertseifer[7], Alfred Morgenstern[7], Roland Kanaar[1,2], Dik C. van Gent[1,2], Adriaan B. Houtsmuller[4,5], Antonia G. Denkova[6], Martin E. van Royen[4,5,8$], Jeroen Essers[1,9,10$]

1. Department of Molecular Genetics, Erasmus University Medical Center, Rotterdam, The Netherlands

2. Oncode Institute, Erasmus University Medical Center, Rotterdam, The Netherlands

3. Department of Radiology & Nuclear Medicine, Erasmus University Medical Center, Rotterdam, The Netherlands

4. Department of Pathology, Erasmus University Medical Center, Rotterdam, The Netherlands

5. Optical Imaging Centre (OIC), Erasmus University Medical Center, Rotterdam, The Netherlands

6. Department of Radiation Science and Technology, Delft University of Technology, Delft, The Netherlands

7. European Commission, Joint Research Centre, Directorate for Nuclear Safety and Security, Karlsruhe, Germany

8. Cancer Treatment Screening Facility (CTSF), Erasmus University Medical Center, Rotterdam, The Netherlands

9. Department of Radiation Oncology, Erasmus University Medical Center, Rotterdam, The Netherlands

10. Department of Vascular Surgery, Erasmus University Medical Center, Rotterdam, The Netherlands

* Contributed equally to this work

$ Contributed equally to this work

Corresponding author: Jeroen Essers: j.essers@erasmusmc.nl

Nanotheranostics 2020; 4(1): 14-25.

ABSTRACT

Polymersomes have the potential to be applied in targeted alpha radionuclide therapy, while in addition preventing release of recoiling daughter isotopes. In this study, we investigated the cellular uptake, post uptake processing and intracellular localization of polymersomes. High-content microscopy was used to validate polymersome uptake kinetics. Confocal (live cell) microscopy was used to elucidate the uptake mechanism and DNA damage induction. Intracellular distribution of polymersomes in 3-D was determined using super-resolution microscopy. We found that altering polymersome size and concentration affects the initial uptake and overall uptake capacity; uptake efficiency and eventual plateau levels varied between cell lines; and mitotic cells show increased uptake. Intracellular polymersomes were transported along microtubules in a fast and dynamic manner. Endocytic uptake of polymersomes was evidenced through co-localization with endocytic pathway components. Finally, we show the intracellular distribution of polymersomes in 3-D and DNA damage inducing capabilities of ^{213}Bi labeled polymersomes. Polymersome size and concentration affect the uptake efficiency, which also varies for different cell types. In addition, we present advanced assays to investigate uptake characteristics in detail, a necessity for optimization of nano-carriers. Moreover, by elucidating the uptake mechanism, as well as uptake extent and geometrical distribution of radiolabeled polymersomes we provide insight on how to improve polymersome design.

Key words: Polymersomes, uptake, radionuclide therapy, live cell confocal microscopy, nano-carriers

INTRODUCTION

Targeted alpha therapy (TAT) is considered as treatment option for various tumours, such as bladder cancer, brain tumours, neuroendocrine tumours, and prostate cancer [1, 2]. Alpha particles have high linear energy transfer (LET) and therefore result in a higher relative biological effect (RBE), compared to low-LET radiation. The range of alpha particles is up to 100 µm in water, while it is even more limited in tissue [3]. These distances only span a few cells, thereby limiting damage to surrounding healthy tissue [4]. In current experimental therapy settings, short-lived radionuclides require rapid targeting for efficient dose delivery to target cells [5]. Long-lived radionuclides can overcome these limitations, but are often part of a longer decay chain which leads to the release of recoiling daughter isotopes. Recoiling daughter isotopes break free from their targeting vehicle, such as antibodies and peptides, and can distribute freely in the body, potentially causing harm to healthy tissue [6, 7]. This problem can be solved by the use of nano-carriers, e.g. liposomes. While the retention of the mother nuclides in liposomes is up to 98%, the retention of the recoiled daughter isotopes is less than 20% [8]. Low retention makes liposomes poor carriers of high-LET radionuclides with multiple alpha emitting isotopes in the decay chain. Nano-carriers composed of polymers, such as dendrimers, polymeric particles, nano-gels and micelles are more robust and are thereby more effective in retaining the daughter isotopes compared to other nano-carriers [9-11].

Polymersomes (PMs), formed through self-assembly of amphiphilic block copolymers, combine the possibility to counter the recoil problem and have highly versatile adjustable properties, making them attractive candidates for customized high-LET radionuclide [12, 13]. Nano-carriers are commonly known to be delivered at the tumor site via the enhanced permeability and retention (EPR) effect [14, 15]. This effect is mostly observed in rapidly growing solid tumors and their high demand for oxygen and nutrients. This high demand causes underdeveloped and leaky vasculature in and around the tumor. PM therapy can exploit this phenomenon, which allows passive PM transfer to tumor areas via the blood circulation. Variation in size could provide beneficial effects on circulation times and mechanical filtration [16]. Recent reports show that variations in charge and degree of attached polyethylene glycol (PEG) affect PM uptake, circulation time and clearance pathways [12, 16-19]. In addition, intra-tumoral injections show high retention in tumor tissue, which could indicate intracellular uptake of PMs and not accumulation in the extracellular matrix [19, 20].

Although the uptake of other nano-carriers in cells has been documented, to our knowledge, no reports show the cellular and biological uptake mechanism of PMs. Recently, several reports show the use of PMs for TAT in both *in vitro* and *in vivo* experiments, suggesting that PMs can be used in a therapeutic setting [21, 22]. The short range and high-LET of alpha particles requires prolonged localization close to the target cells, which can be reached if PMs are geographically fixed by cellular uptake. A better understanding of the precise uptake mechanism and geometrical distribution of the PMs is crucial to understand how they exert their cell-killing

effect in different cell populations. With the use of high-content, confocal (live cell) and super-resolution imaging we evaluate cellular uptake kinetics and post-uptake processing of PMs.

MATERIALS & METHODS

Polymersome preparation and characterization

PMs with average diameters of 60 and 80 nm were prepared according to the 'inverse nanoprecipitation method' [23]. In short, the amphiphilic diblock copolymers (polybutadiene-d- polyethyleneoxide ($PBd_{1800}PEO_{900}$)) were dissolved in 1 mL acetone in a 4 ml glass vial (Rotilabo®), using a Vortex-Genie 2 (Scientific industries, Inc.) to obtain a 20 mg/mL block copolymer concentration. The solution was filtered using a 0.20 µm syringe filter (PFTE, unsterile, Rotilabo®). Afterwards, 50 vol % PBS was added using an Aladdin programmable syringe pump (World Precision Instruments, LLC) and a 2 mL Injekt™ syringe (B Braun) under magnetic stirring on a Standard Stirrer (VWR®) at 300 rpm. The remaining acetone was evaporated using a Rotary Evaporation at 30 degrees for at least 15 minutes. Samples of size 400 nm were prepared according to the 'direct dissolution method' [24]. In short, 10 mg/mL block copolymer was added to a 1 mM DTPA PBS solution at pH 7.4, and stirred for a week. Subsequently, the PMs were extruded to the required diameter by passing them several times through polycarbonate filters with cut-off membrane of 400 nm. PMs used for radiolabeling were passed through a 30 cm x 0.5 cm (L x r) Sephadex G 25 M size exclusion column (Sigma-Aldrich) to remove excess DTPA.

The size and shape of the PMs were determined by Dynamic Light Scattering (DLS) and Cryogenic- Transmission Electron Microscopy (Cryo-TEM). The DLS apparatus consisted of a JDS Uniphase 633 nm 35 mW lasers, an ALV sp 125 s/w 93 goniometer, a fiber detector and a photon counter (Perkin Elmer). An ALV-500/epp correlator was used to obtain the size correlation function. Scattering cells of 3 mL with an internal diameter of 12 mm were immersed in a temperature regulated toluene bath. The intensity auto-correlation function was determined at 90 degrees. The autocorrelation function was analyzed by the Contin method [10] and the radius of the PMs was determined using Einstein-Stokes equation.

Cryo-TEM characterization was done as described before [11]. In short, 3 µL of a 10 mg/mL PMs solution was deposited on a holey carbon film (Quantifoil 2/2) supported on a TEM grid. The sample was blotted and vitrified by rapid immersion in liquid ethane (Leica EM GP version 16222032), and subsequently immersed in liquid nitrogen. A cryo-transfer holder (Gatan model 626) was used to transfer to a Jeol JEM 1400 TEM and images were acquired at an acceleration voltage of 120 keV. For diameter determination, 30-50 images were made of PM samples and measured using FIJI [25].

Fluorescent labeling and Quantification

Membrane labeling of PMs was done using a fluorescent moiety attached to a lipophilic tail with optimal excitation at 551 nm and emission at 567 nm (PKH26, Sigma-Aldrich) or with optimal excitation wavelength at 490 nm and emission at 502 nm (PKH67, Sigma-Aldrich) according to manufacturer protocol. In short, 20 µL of PMs (10 mg/mL) and 5 µL PKH-dye (working concentration of 2.5E-5 M) were separately diluted in provided Diluent C to 100 µL end volume. Hereafter, the two solutions were mixed and incubated for 10 minutes. After the 10-minute incubation step the PMs are separated from unbound PKH dye using an Exosome Spin Column (Sigma-Aldrich) according to manufacturer protocol. Columns allow buffer exchange on the PMs or to remove any low molecular weight (MW ≤ 3000) mixtures from the preparation. In short, provided spinning columns were solidified using 650 µL PBS and incubated for 10 minutes. Excess PBS was removed by centrifuging the column for 2 minutes at 750 x g. 100 µL of labeled PM solution was then added to the column and centrifuged for 2 minutes at 750 x g, leaving only labeled PMs in Diluent C solution. PKH labeled PMs were quantified by an newly developed confocal fluorescent microscopy assay (EVQuant) [26]. In short, fluorescently labeled particles were immobilized in a transparent gel and imaged using an Opera Phenix High Content Screening (HCS) System (Perkin Elmer) and analyzed using Harmony 5.4 (Perkin Elmer). Absolute concentration of in-gel immobilized particles is derived from the number of detected fluorescent particles in the calibrated volume of the imaged region.

Radioactive labeling

Elution of ^{213}Bi was performed as described before [27]. The elution mixture was composed of 0.3 mL, 0.2 M HCl and 0.3 mL 0.2 M NaI and pumped through the generator at a flowrate of 0.15 mL/min into a vial containing 0.12 mL of 4 M sodium acetate buffer.

For PM labeling, 700 µL of ^{213}Bi was added to a mixture of 10 µL 20 mM tropolone and 100 µL 100 mM Hepes. This solution was incubated for 15 min at RT allowing the ^{213}Bi to bind with tropolone. Subsequently, 200 µL 1 mM DTPA encapsulated PMs with a concentration of 1E13 fluorescently labeled PMs/mL was added to the mixture and incubated for 1 hour. Next, the activity was measured by using a NaI detector before and after the column purification of the solution to calculate the loading efficiency of the PMs. Column purification was done using a Sephadex G 25 M column (Sigma-Aldrich) to remove excess DTPA. ^{213}Bi retention was similar to previously reported labeling methods for ^{111}In and ^{225}Ac [10]. 100 µL 10 mM DTPA was added to 0.5 mL polymersomes loaded with ^{213}Bi and equilibrated for 15 minutes at room temperature. Subsequently, the solution was passed through a Sephadex PD10 column to separate the Bi-DTPA complexes from the polymersomes. The elution was portioned per mL and the ^{213}Bi activity in each eluted fraction was determined by dividing the activity detected in the polymersomes by the total activity before separation. At the dose used, no difference in size and physical characteristics was expected [28].

Cell Culture

U2OS (Human Bone Osteosarcoma), J774A.1 (Mouse Balb/c Monocyte Macrophage) and CA20948 (Rat Pancreatic Cancer) cell lines were cultured in Dulbecco's modified Eagle's medium supplemented with 1% Penicillin/Streptomycin and 10% Fetal Calf Serum. The C5Ro (Human fibroblast) cell line was cultured in Hams' F10 culture medium supplemented with 1% Penicillin/Streptomycin and 15% Fetal Calf Serum. DU145 (Prostate Cancer, CNS Metastasis) and PNT2C2 (Prostate Epithelial) cell lines were cultured in RPMI 1640 medium supplemented with 1% Penicillin/Streptomycin and 5 or 10% Fetal Calf Serum. Mouse embryonic fibroblasts (MEFs) were cultured in 50% Dulbecco's modified Eagle's medium and 50% Hams' F10 medium supplemented with 1% Penicillin/Streptomycin and 10% Fetal Calf Serum. All cells were incubated at 37 ºC in a water saturated atmosphere with 5% CO_2.

High-content microscopy

To visualize and quantify PM uptake, cells were seeded (10.000-20.000 cells per well) in 96-wells plates (Sensoplate, Greiner Bio) in duplicates and cultured for 24h. Cells were incubated with PKH26-labeled PMs of different sizes (60, 80 and 400 nm in diameter) and different concentrations (1E10, 2E10, 5E10 or 1E11 PMs/mL) for 1, 2 and 3 hours prior to fixation (4% PFA, 30 min). Cells were washed with PBS and plasma membrane was labeled using PKH67 (Sigma-Aldrich) according to the manufacturers protocol. In short, fixed cells were incubated in 50 µL Diluent C containing PKH67 (2 µL/mL). Samples were stored in 200 µL PBS containing Hoechst (1:10000) for nuclear staining. Fluorescent images were acquired using an Opera Phenix HCS system (Perkin Elmer). For each well, 25 Images were acquired using a 20x objective (NA = 0.4) and the appropriate laser lines and emission filters (Hoechst; ex. 405 nm - em. 435-480 nm, PKH67; ex. 488 nm – em. 500-550 nm and PKH26; ex. 561 nm – em. 570-630 nm. Images were analyzed by the Opera Phenix analysis software (Harmony 5.4) to quantify the number of PMs per cell.

Confocal (live cell) microscopy

To capture dynamic events of PM uptake and processing, cellular uptake of PMs was analyzed by high-speed Spinning disk microscopy (Nikon Ti-Eclipse and ROPER FRAP3D unit). To study PM uptake in living cells, we used a PNT2C2 cell line stably expressing CAAX-GFP [29]. For microtubule imaging PNT2C2 cells were transiently transfected using Tubulin-YFP (YFP-β-tubulin expression construct was kindly provided by Dr. Galjart, Erasmus University Medical Center). For PM uptake experiments, 1E11 PKH26-labeled PMs/mL were added to cells and image acquisition was started using intervals of 500/1000 ms. PM movement speed was analyzed using the TrackMate plugin in FIJI [30].

For co-localization experiments PNT2C2 cells were transiently transfected with Rab4a-YFP (early-endosomes, [31]) or incubated with LysoTracker Red (lysosomes, Invitrogen). Rab4a-YFP transfected cells were incubated with PKH26-labeled PMs and LysoTracker Red labeled cells were incubated with PKH67-labeled PMs. Cells were incubated with 1E11 PMs/mL for 30 min-

utes, washed with PBS and fixed at time points 30, 60, 90, 120, 180, 240, 300 and 360 minutes after starting PM incubation. Fluorescent laser scanning confocal microscopy (CLSM510, Zeiss) was used to capture at least 10 cells per time point for both endocytic markers.

Co-localization analysis was performed using FIJI and a customized FIJI macro. In short, in every image both PMs and endocytic compartments in transfected cells were identified and masked based on thresholding the two fluorescent channels. Subsequently, the number of PMs overlapping with endocytic compartments was divided by the total number of PMs to calculate the percentage of co-localization for each image.

To visualize the DNA-damage induced by radioactive loaded PMs, U2OS cells were transiently transfected with 53BP1-GFP (marker for DNA double-strand breaks, full length 53BP1) [32].

Transfected cells were treated with ^{213}Bi- and PKH26 labeled PMs. ^{213}Bi was used as damaging agent and PKH26 was used for visualization of PMs. Cells were treated for 3 hours, washed with PBS and fixed. Confocal microscopy (Leica SP5) was used to capture cells with and without PMs. The numbers of DNA damage clusters were manually quantified. To investigate the fate of 53BP1 clusters induced by alpha particle irradiation, U2OS cells were transiently transfected with mScarlet-53BP1. Truncated 53BP1 (t53BP1, [33]) was fused to mScarlet and inserted into a homemade PiggyBac construct. Plasmid and construct information is available on request. Transfected cells were externally irradiated using previously described methods [34]. Live cell imaging was performed on a confocal microscope (Leica SP5) overnight (16 hours). Number of cells going through mitosis was manually quantified.

Super resolution imaging and distance distribution analysis

For intracellular distribution analysis of intracellular PMs, structured illumination microscopy (SIM) was used. PNT2C2 cells were incubated with 1E10 PMs/mL for 2 hours. SIM imaging was performed on a Zeiss Elyra PS1 with an Andor iXon DU 885 EMCCD camera (Carl Zeiss AG, Oberkochen, Germany) using 488, 561 and 642 nm laser excitation with 100 ms exposure times. Samples were illuminated with a spatial line pattern that was shifted in five phases and rotated in five orientations. The raw images were reconstructed into a high-resolution 3D-dataset using the Zeiss 2012 PS1 ZEN software. Reconstruction was done using default settings.

The location of each PM in an image was determined using the find maxima algorithm in FIJI. Distribution of PM distance to the nucleus was measured for each cell using intensity profiles of the lines between the center of the nucleus and all PMs. The distance was defined as the length from the PM up to the onset of the nuclear staining. Cutoff distance was determined according to the decay chain of ^{213}Bi to ^{209}Pb, mainly emitting an alpha particle of 8 MeV [35].

RESULTS

Kinetics of polymersome uptake in different cell-types

The PMs used in our experiments are composed of polybutadiene (PBd) and polyethylene oxide (PEO) block co-polymers and were formed in solution by 'inverse nanoprecipitation' (for PMs <100 nm) or 'direct dissolution' (for PMs >100 nm). PMs were characterized by Cryo-TEM and DLS, which showed that the obtained PMs had size distributions of 60 (±8), 80 (±11) and 400(±7)

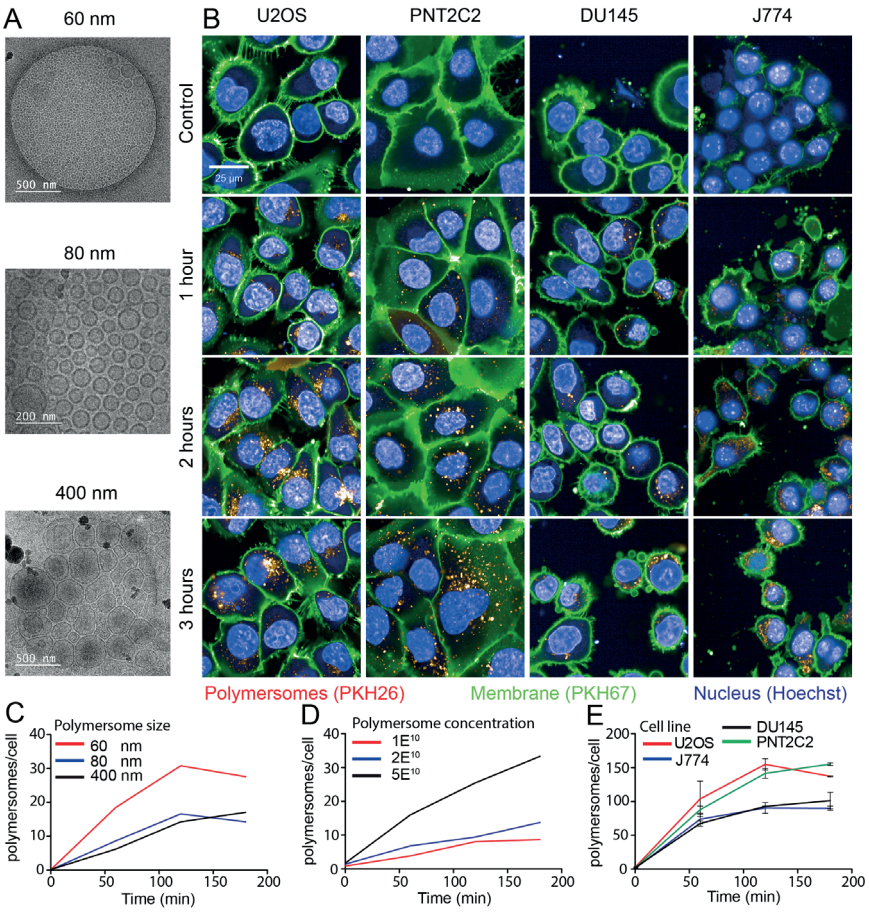

Figure 1. Uptake kinetics of polymersomes. (A) Cryo-TEM analysis of PMs dissolved in water **(B)** U2OS, PNT2C2, DU145 and J774 cells labeled with PKH67 (green) as membrane marker were incubated with 80 (±11) nm PMs labeled with PKH26 (red). Cells were fixed at indicated time points and imaged using a high-throughput Opera Phenix system. **(C)** Quantitative analysis of 60 (±8) nm (red), 80 (±11) nm (blue) and 400 (±7) nm (black) sized PM uptake in U2OS cells. **(D)** Uptake analysis of 80 (±11) nm sized PMs in PNT2C2 cells at 1 (red), 2 (blue) or 5 (black) times the original concentration used for uptake experiments. (E) Quantitative analysis of uptake in U2OS (Red), J774 (blue), PNT2C2 (green) and DU145 (black) cells incubated with 80 (±11) nm sized PMs. Error bars indicate SEM, technical replicates. N>1000 cells per condition.

nm in diameter (Figure 1A). To investigate the cellular uptake mechanism of PMs we used different cell types, U2OS (bone osteosarcoma), PNT2C2 (prostate epithelial), DU145 (prostate cancer) and J774A.1 (mouse macrophage, from now on referred to as J774). Exploiting the bi-layered membrane of PMs we employed PKH-dyes for *in vitro* fluorescent tracking. PKH-dyes are composed of intense fluorescent moieties attached to long lipophilic tails. Diffusion of the lipophilic tails in the bi-layer, leaves the fluorescent moiety exposed for PM tracking. Using both PKH26 (Excitation 551 nm/Emission 567 nm) and PKH67 (Excitation 490/Emission 502) we labeled PMs suitable for multiple color combinations. The concentration of detected PMs was measured by the recently developed nanoparticle quantification assay EVQuant [26]. The EVQuant assay revealed a labeling efficiency of up to 80% for PKH dyes and concentrations of up to 7.64E13 PMs/mL. Pilot experiments in mouse embryonic fibroblasts (MEFs) showed clustered PM influx using wide-field microscopy, from 6 hours post incubation onwards to 48 hours (Figure 2). Due to this observation we chose for earlier time points and confocal microscopy in the uptake assays for optimal quantification. For uptake experiments the cells were incubated with PMs (80±11 nm) and fixed at 1, 2 or 3 hours post incubation. No background signal at control conditions was observed and PM uptake did not affect cell morphology. Over the course of 3 hours,PMs gradually entered the intracellular compartments of all cell types (Figure 1B). Most notably, the distribution of PMs at 3 hours showed a perinuclear positioning in U2OS cells compared to a random distribution in PNT2C2 cells.

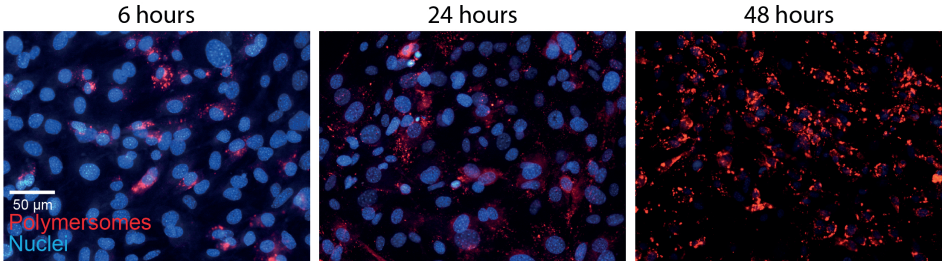

Figure 2. Polymersome uptake. MEFs were incubated with 80 (±11) nm sized PKH26 labeled PMs. Cells were fixed at indicated time points and imaged using a wide field epifluorescent microscope (Axio Imager D2, Zeiss).

To determine the influence of PM size and concentration on the uptake kinetics in different cell types we employed high-content microscopy for quantitative measurements. As differences in nano-particle size could influence cellular uptake kinetics, we first compared uptake rates of 60, 80 and 400 nm diameter PMs in U2OS cells. In a 96-well plate, 10,000 U2OS cells per well were incubated with 2E10 PKH26-labeled PMs/mL for 1, 2 and 3 hours. Cells were washed with PBS and the cell membranes and nuclei were stained by PKH67 and Hoechst, respectively. Faster uptake kinetics were observed for PMs with 60 nm in diameter compared to 80 and 400 nm. Cells incubated with 60 nm PMs reached a higher plateau level at 3 hours post addition

compared to both 80 and 400 nm sized PMs (Figure 1C). Next, various concentrations of initial stock concentrations of PMs were assessed for uptake using PNT2C2 cells using the same high-content microscopy set-up. Cells were incubated for 15, 30, 60, 90, 120 and 180 minutes with 1E10 PMs/mL, 2E10 PMs/mL, and 5E10

PMs/mL of 80 nm diameter PMs. PM uptake is linear with the concentration we used (an average of 2.5 times more PMs at 120 min, between 2E10 and 5E10 PMs/mL, Figure 1D).

Finally, to assess possible differences among cell lines, four different cell lines were incubated with 1E11 PMs/mL. Comparison between different cell lines revealed similar uptake kinetics over time for each of the four cell lines reaching a plateau after 2 hours, possible caused by cellular restrictions of further uptake. Interestingly, the U2OS and PNT2C2 cell lines and the J774 and DU145 cell lines showed a difference in plateau levels (Figure 1E). Altogether, we found that uptake of PM was 2-fold higher for 60 nm PMs compared to 80 nm and 400 nm PMs. Moreover, uptake increased linearly from 1E10 to 5E10 PMs/mL. Finally, the maximum number of PM taken up differed among cell lines.

Uptake and dynamic processing of polymersomes

In previous high-content screens we observed that PM uptake already occurs in the first 15 minutes after addition. We therefore wanted to capture the immediate response of cells after addition of PMs. To visualize the cellular membrane and transport across this membrane we used a PNT2C2 cell line which stably expresses CAAX-GFP. The CAAX-motif is a target for prenylation [36], and when attached to the GFP protein, it will target GFP to the plasma membrane. CAAX-GFP is therefore a fluorescent marker of the cell membrane, which was used for live-cell imaging of PMs entering the cytoplasmic compartment of cells. Imaging with intervals of 20 min was started immediately after additions of PMs. Interestingly, cells undergoing mitosis (the two upper cells) showed dramatically higher uptake of PMs than cells in other phases of the cell cycle (lower cells, movie S1, scale bar: 20 μm).

To shorten the time interval, we used high-speed spinning disk microscopy which allowed recording of events with minimal time intervals as short as 500 ms. Captured movies are represented using stills of several time points (Figure 3A). At t=0 s recording started, several seconds after addition of PMs. The first captured image already showed that PMs entered the cells, indicated by the white arrow. Within 28 seconds the indicated PM entered the cytoplasmic compartment and moved toward the center of the cell (t=71 s and movie S2, scale bar: 10 μm). Internalized PMs were surrounded by green signal, indicated by the yellow arrow and in the close up square. Since CAAX-GFP is localized as an integral part of the plasma membrane we explain this by assuming that internalization of PMs occurs with concurrent internalization of the cellular membrane. This indicates that uptake could occur via an endocytic pathway [37]. The short time interval imaging revealed highly dynamic and directional movement of PMs after uptake (Movie S3, scale bar: 10 μm). Directionality of intracellular movements could point to processing of PMs by cell components such as microtubules [38].

We therefore expressed Tubulin-YFP in PNT2C2 cells to image the microtubules inside PNT2C2 after PM uptake. Again, cells were incubated with PKH26-labeled PMs and spinning disk microscopy was used for imaging of microtubules. The dynamic and directional movements of internalized PKH26-labeled PMs (white arrow) localized at microtubules (Figure 3B and movie S4, scale bar: 10 µm). The linear displacement movement speeds through the cytoplasm reached intracellular velocities up to 1 µm/s (Figure 3 C and D). Interestingly, velocity showed periodic peaks over-time, indicating 'pause' steps during the process. Co-localization with microtubules and periodic movements already shown for early-endosomes generates a second indication of endocytic uptake of PMs [39].

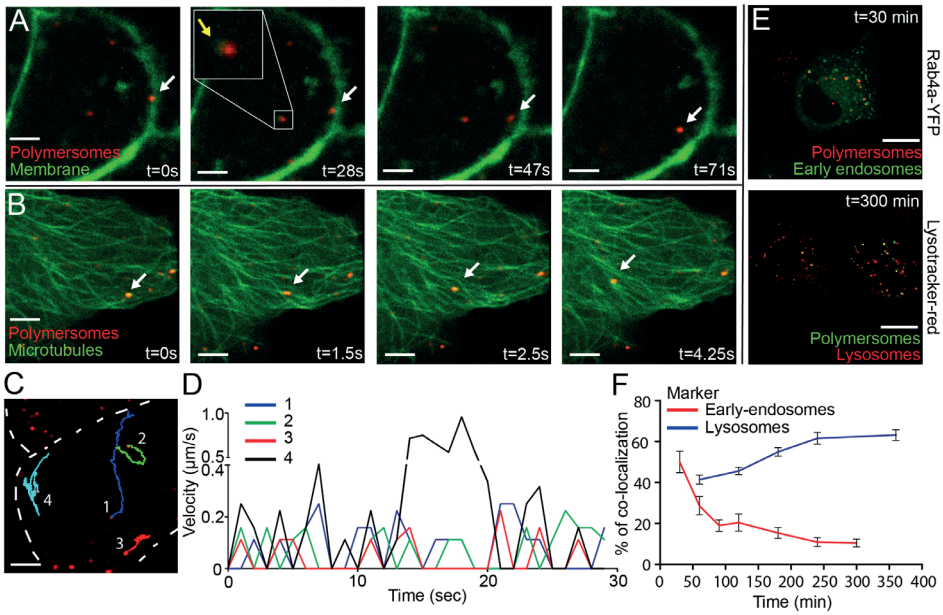

Figure 3. Rapid uptake, microtubule processing and co-localization of the endocytic pathway of polymersomes. PNT2C2 cells stably expressing either CAAX-GFP or transiently expressing Tubulin-YFP were incubated with 80 (±11) nm sized PMs (PKH26 labeled, red) and imaged using Spinning Disk Confocal Microscopy. **(A)** Stills of PM uptake, showing attachment (0s), uptake (28-47s) and intracellular processing (47-71s) of PMs, indicated by white arrows. CAAX-GFP component (in green) encircles PMs inside the cell, indicated by yellow arrows. Scale bar represents 5 µm. **(B)** Stills of PM processing. Microtubule labeled by Tubulin-YFP, green. Arrows indicate PMs moving along microtubules. T=0 represents the start of imaging. Scale bar represents 5 µm. **(C)** Representative image of 4 PMs which were tracked over-time. Cell membrane is represented by the dashed line. Scale bar represents 5 µm. **(D)** Velocity of 4 PMs over 30 seconds in a cell. PMs were tracked using Manual Tracking in FIJI. **(E)** DU145 cells (expressing Rab4a-YFP or incubated with Lysotracker-Red) were incubated with 80 (±11) nm PMs (containing PKH26 or 67) and fixed at various time points. Rab4a co-localization and Lysotracker co-localization at 30 and 300 min. Scale bar represents 25 µm. **(F)** Quantification of PM co-localization with early endosomes and lysosomes in time. Error bars indicate SEM, N=10 cells per time point.

Analysis of endocytic uptake of polymersomes

For further analysis of the intracellular fate of PMs we used co-localization studies. With the use of specific proteins or makers that label early-endosomes (Rab4a-YFP) and lysosomes (Lysotracker red) we investigated the co-localization of endocytic bodies and intracellular PMs. Rab4a-YFP expression constructs were transiently transfected into PNT2C2 cells. Rab4a-YFP (Excitation 514/Emission 525) was combined with PKH26 labeled PMs and Lysotracker red (Excitation 550/Emission 590) was combined with PKH67 labeled PMs. In a pulse-chase experiment we incubated cells with PMs (1E11 PMs/mL) for 30 minutes, washed with PBS and refreshed with complete medium. Treated cells were fixed at 30, 60, 90, 120, 180, 240 and 360 minutes after PBS-wash. At least 10 cells per time point were imaged for co-localization analysis of PMs compared to marked endocytic pathway components (Figure 3E, typical examples at 30 and 300 minutes after PBS wash). 50% of PMs (PKH26) co-localized with early-endosomes (Rab4A-YFP) at 30 minutes, which declined to 10% within 5 hours. In contrast, co-localization between Lysotracker red (lysosomes) and PKH67 labeled PMs increased to 60% within 6 hours after treatment (Figure 3F). These results showed the transition of PMs throughout the maturation of early-endosomes to lysosomes in the endocytic pathway. In addition, spinning disk microscopy of PNT2C2 cells transiently expressing Rab4a-YFP (early-endosomes) showed clear merging of Rab4a-YFP labeled organelles containing PMs, indicating fusion of early-endosomes to late-endosomes/lysosomes (Movie S5, scale bar: 10 µm). We conclude that *in vitro* uptake of PMs is mediated through the endocytic pathway, where PMs enter the cell via early-endosomes and ultimately accumulate in lysosomes.

High-resolution analysis of intracellular distribution of polymersomes

The position of PMs is highly dynamic during the processing of endosomes to lysosomes. The dynamic distribution of PMs throughout this process could greatly influence the efficiency of energy deposition of alpha particle irradiation [40]. The information of the exact distance of PMs to nuclei at certain time points could be of great use, considering the short path-length of alpha particles. With the use of Structured Illumination Microscopy (SIM) we determined the position of intracellular PMs with high precision and evaluated per nucleus the number of PMs which were in range to deposit alpha particle radiation to the nucleus. We treated PNT2C2 cells with PKH26 labeled 80 nm PMs for 2 hours, washed with PBS, fixed, and stained the nuclei with DAPI. Using 3D analysis, we drew lines between centers of nuclei and PMs (Figure 4A and movie S6). By measuring the intensity profile of the nuclear staining on the straight lines we calculated the distance between the edge of the nucleus and all PMs in a single image. We use the drop of sirDNA signal as indication of the edge of the nucleus (Figure 4B.1). Distances between the edge of the nucleus to the PM coordinate was defined as ‘distance to nucleus’. By calculating all PM to nucleus distances we generated a distance distribution (Figure 4B.2). The histogram shows that most PMs (1008 of 1091, 92%) are within the range of the supposed alpha particle path length (<40 µm, red line, median: 17.7 µm). We conclude that many PMs can contribute

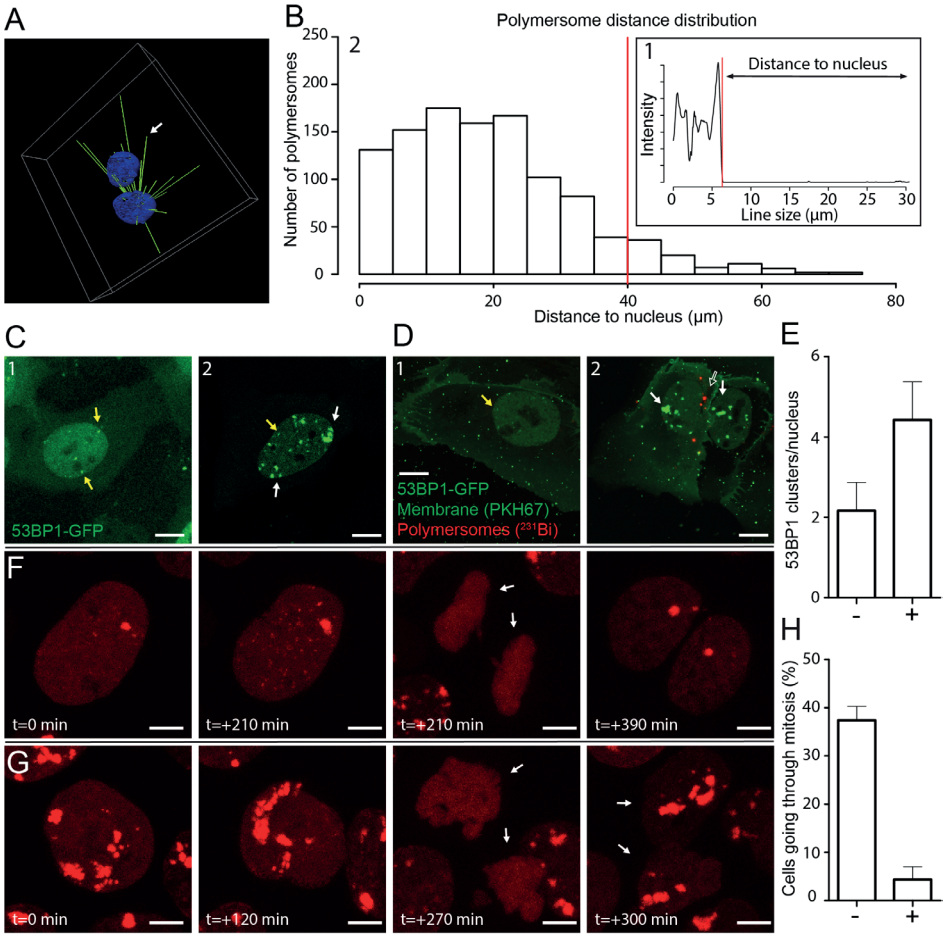

Figure 4. Polymersome distance distribution of ^{231}Bi labeled polymersomes and DNA damage induction. PNT2C2 cells were incubated for 2 hours with 80 (±11) nm sized PKH26 labeled PMs. **(A)** 3D representation of the distance calculation between PM and the center of a nucleus. White arrow indicates the position of one PM. The intensity profile on the right shows the intensity of nuclear staining measured on that straight line. Distance of PM to nucleus is the determined as the line size between the clear drop of nucleus signal to PM position. **(B)** Example of an intensity profile measured on a straight line in between a PM and the center of a nucleus. Red line indicates the threshold for the edge of the nucleus (B.1). Overall distance distribution of PMs to nucleus (N=1091). Red line shows the relevant 40 µm distance cut off (B.2). **(C)** U2OS cells expressing 53BP1-GFP as DNA-damage marker. Typical examples of U2OS cells expressing 53BP1-GFP at control levels (C.1) and after alpha-particle irradiation (C.2). Yellow arrows indicate endogenous 53BP1-GFP foci and white arrows indicate DNA damage caused by alpha-particle irradiation. **(D)** U2OS cells expressing 53BP1-GFP were incubated with PMs (empty arrow) labeled with ^{231}Bi (0.15 MBq) for 3 hours. Membrane was labeled with PKH67. Yellow arrows endogenous 53BP1-GFP foci (D1). White arrows indicate alpha-particle induced DNA damage. Empty arrow indicates radiolabeled PMs (D1). **(E)** DNA damage quantification. 7 cells without (-) or with (+) intracellular PMs (total = 14 cells) were evaluated for amount of 53BP1 foci. Error bars show SEM. Scale bar represents 10 µm. (F) U2OS cells expressing mScarlet-t53BP1 as DNA-damage marker. Typical examples of cells going through mitosis without DNA damage **(F)** and after alpha-particle irradiation (G). Arrows indicate the 2 daughter cells after mitosis. Time points indicate time in between snap shots. Scale bar represents 5 µm. (H) Quantification of mitosis. N= 38 for non-irradiated cells (-), N = 95 for irradiated cells (+) Error bars show SEM.

to effective alpha particle irradiation of cell nuclei in a 2-D setting. To test this, the efficacy with which DNA damage could be induced could be investigated using radiolabeled PMs with alpha particle emitting radionuclides.

^{213}Bi labeled polymersomes damage nearby nuclei of U2OS cells after uptake

Positioning of PMs in the cytoplasmic compartment of cells could be crucial for the effective DNA damage induction when irradiation is used. We used the DNA damage marker p53 binding protein 1 (53BP1) fused to GFP to visualize DNA damage inflicted by radioactivity in U2OS cells [41]. In addition, we used PKH26 and PKH67 to visualize PMs and the plasma membrane, respectively. Typical examples of 53BP1-GFP control conditions and after external alpha particle irradiation are used as reference to PM treated samples. A few small 53BP1-GFP clusters were present when no DNA damage is induced (yellow arrows, Figure 4C.1) compared to numerous and large 53BP1-GFP clusters after alpha particle induced DNA damage (white arrows, Figure 4C.2).

To investigate DNA damage inflicted by alpha particles, originated from radiolabeled PMs, we used ^{213}Bi as radionuclide. Radioactive labeling of PMs showed efficiencies up to 49.2% for ^{213}Bi and the activity measured was 372 kBq/mL. U2OS cells were treated with 2E12 ^{213}Bi-PMs/ml (372 kBq) for 3 hours, washed with PBS and fixed. Confocal imaging was used to determine the spatial distribution of double strand breaks (53BP1-GFP clusters) and PMs after treatment (Figure 4D). Nuclei of cells with intracellular PMs (Figure 4D.2, unfilled arrow) showed increased 53BP1-GFP clusters, compared to nuclei of cells with no intracellular PMs (Figure 4E.1). Quantification showed a 2-fold increase of 53BP1-GFP foci in the nucleus if ^{213}Bi labeled PMs are in the cytoplasmic compartment of U2OS cells (Figure 4E). These results are comparable with the external alpha particle irradiation experiments, indicating direct DNA damage induction by intracellular ^{213}Bi labeled PMs but no apparent DNA damage induction to nuclei in close vicinity. To investigate the fate of alpha particle irradiated U2OS cells at later time points we used live-cell imaging. U2OS cells transiently transfected with mScarlet-t53BP1 (a truncated version of 53BP1) were externally irradiated with alpha particles and imaged immediately. Snapshots of both non-irradiated and irradiated cells show that both go through cell division (Figure 4F and G, movie S7). Interestingly, alpha particle induced DNA damage did not prevent cell division. However, quantification showed that cells not hit by alpha particles showed significantly more dividing cells than cells that did got hit (32% vs 3.2%, Figure 4H). We conclude that ^{213}Bi-PMs induced DNA damage to U2OS nuclei when PMs were present in the cell, comparable with DNA damage when external alpha-irradiation was used. When PMs were not intracellular, no apparent induction of DNA damage was observed. Cells hit by alpha particles are possibly delayed or restricted to go through mitosis compared to cells that did not get hit. Moreover, our improved understanding of PM internalization assists in accurate prediction of nuclear DNA damage induction by radionuclide carrying PMs in targeted cells.

DISCUSSION

PMs have high potential in targeted alpha radionuclide therapy, while in addition the recoil problem of high-LET radionuclides could be solved. In this study we investigated the cellular uptake and intracellular processing of PMs to elucidate the uptake characteristics of PBd-PEO based PMs. Our work demonstrates that altering PM size and concentration affects the initial rate of uptake and overall uptake capacity. In addition, PM uptake varies between cell lines and cells undergoing mitosis have an increased PM uptake. High-speed live cell microscopy shows that PMs enter cells, co-localize with membrane components, and are transported along microtubules in a dynamic fashion. Evidence for endocytic uptake of PMs was obtained from

PM uptake and efficiency by macrophages (J774) was similar to prostate cancer cells (DU145) but less than osteosarcoma (U2OS) and prostate-epithelial (PNT2C2) cells (Figure 1B). Cell size or shape could have impact on the uptake rate and plateau levels of PM uptake. Larger cells have more surface area for PMs to enter and less membrane tension which leads to increased uptake efficiency [42]. Unexpectedly, macrophages did not show disproportionately faster or increased uptake compared to cancer or epithelial cell lines. This is in contrast to several *in vivo* reports where high levels of liver and spleen uptake was observed. Uptake in these organs is explained by the presence of macrophages, for example Kupffer cells in the liver [19, 43, 44]. A possible explanation for the difference in the data obtained *in vivo* versus the data from cultured cells could be the immortalization of J774 cells. Immortalized cell lines could acquire altered properties over time in cell culture [45]. Including primary cells, for example harvesting Kupffer cells from the liver, could provide a more realistic setting [46]. On the contrary, specific uptake by tumour-associated macrophages could induce polarization, which is thought to be beneficial for immune-therapies [47].

In addition to cell type or size, cell-cycle state could also have an impact on PM uptake. Live-cell imaging shows increased PM uptake at the point of mitosis. The alteration of the cell membrane during mitosis could allow PMs to enter the cells [48]. In addition, the change of cell shape during mitosis is accompanied by recycling membrane components to intracellular compartments [49]. The increased uptake of PMs by dividing cells suggests enhanced uptake in frequently dividing tumor cells, important for therapeutic approaches using PMs [50]. The uptake of PMs we observe in our experiments and encounter in previous literature suggests that endocytosis is the most probable pathway by which PMs enter cells [51]. Co-localization experiments confirmed that PMs enter the cell and reside in early-endosomes, eventually ending up in lysosomal compartments. In addition, intracellular processing of PMs shows co-localization with microtubules and bi-directional movement patterns and speeds of 0.2 to 1 µm/s for 4 measured PMs. The measured velocities are comparable with previously reported values of 0.6 µm/s [52, 53]. Since the PMs we employed are non-biodegradable we assumed that they remain in the cytoplasm for longer periods than we have investigated and form bulky lysosomal

compartments [54]. While we show the co-localization with endocytic compartments during PMs entry and processing, the exact endocytic pathway remains to be elucidated. The use of haploid-screening could be used to determine important genes for PMs uptake, shown in similar experiments for viral entry and chemotherapeutic sensitization [55, 56].

Aside from PM uptake, knowledge of intracellular localization is desired for (micro)dosimetry calculations. Simulations have shown that radionuclides in close vicinity of the nucleus have higher RBE compared to radionuclides at the membrane [40]. Theoretically, the amount of DNA damage is dependent on the position of the Bragg peak [57]. Radiolabeled PMs localized close to the nucleus should therefore have a higher chance to induce DNA damage due to geometric considerations. Peri-nuclear localization and lysosomal aggregation after uptake of non-biodegradable nano-carriers is suggested and described in literature [58]. This was observed in U2OS cells already 1 hour after PM addition, but not in PNT2C2 cells, which show a more random distribution (Figure 1B). Our data suggest a random distribution of multiple PMs within 40 µm of surrounding nuclei in a 2-D setting in PNT2C2 cells (Figure 4B). In addition, PMs are being trafficked throughout the cytoplasm via microtubules in the investigated time span and eventually accumulate in the lysosomes (Figures 3B and E, Movies S2 and S3). This movement and positioning is dependent on time, but also on cell type (Figure 1B, [59]). The continuous movement makes a direct correlation of PM location and the induction of DNA damage very challenging. In addition, recent work highlights the need for active targeting of PMs, especially in the presence of a tumour [60]. This could possibly change the uptake and processing dynamics of PMs, both *in vitro* and *in vivo* [61-63].

However, the analysis presented here could function as a prerequisite for the interpretation of 2-D experiments for comparison to 3-D *in vitro* systems, where radiation from neighbouring cells is much higher [21]. In addition, in current experimental set-up, the small amount of PMs translates to a small amount of alpha particles that are being emitted and a low delivered dose to cells. Using ^{213}Bi, we provided preliminary insight of possible therapeutic benefit. However, the singular alpha emission of ^{213}Bi, does not provide enough information of the benefit of intracellular PMs. ^{225}Ac, for example, has multiple alpha emissions in its decay chain. The use of ^{225}Ac has seen therapeutic potential in glioma models [21]. For future studies, the use of ^{225}Ac might be more relevant to investigate the benefit of geographically fixing radiolabeled PMs intracellularly. Moreover, our observations suggest that in a 2-D setting, most of the alpha particles go out of plane, not hitting a nucleus. This makes it hard to explain an one-to-one ratio correlation of DNA damage with the intracellular PMs responsible of emission. This demonstrates the impact of localization and uptake efficiency of PMs labeled with alpha particle emitting radionuclides.

In conclusion, PM uptake is mediated via endocytosis and is particle size, concentration, and cell type dependent. Our findings suggest that PM and, in theory, other nano-carrier uptake and processing can differ significantly between cell lines. This difference will influence the effective DNA damage induction by the radionuclides encapsulated by PMs. Analysing uptake

characteristics using the assays presented in this study will help to provide crucial information, such as DNA damage inducing capabilities and effective uptake. In addition, the assays provide techniques to study the effect of specific characteristics of nano-carriers, for later therapeutic use. Future experiments with PMs and other nano-carriers will benefit from the advanced analysis presented here and results should be considered for increased efficiency of optimization for new nano-carriers.

ABBREVIATIONS

TAT: targeted alpha therapy; LET: linear energy transfer; RBE: relative biological effect; PM: polymersome; EPR: enhanced permeability effect; PEG: polyethylene glycol; SIM: structured illumination microscopy; PBd: polybutadiene; PEO: polyethylene oxide; 53BP1: p53 binding protein 1.

SUPPLEMENTARY MATERIAL

Movie S1: Dividing cells. http://www.ntno.org/v04p0014s1.avi
Movie S2: polymersome entering. http://www.ntno.org/v04p0014s2.avi
Movie S3: Dynamic polymerome processing. http://www.ntno.org/v04p0014s3.avi
Movie S4: Microtubule colocalization. http://www.ntno.org/v04p0014s4.avi
Movie S5: Endosomal merging. http://www.ntno.org/v04p0014s5.avi
Movie S6: 3D analysis of polymersome distribution. http://www.ntno.org/v04p0014s6.avi
Movie S7: Live cell imaging of 53BP1. http://www.ntno.org/v04p0014s7.avi

ACKNOWLEDGEMENTS

We would like to thank Gabriella Tany for her contributions to the work on 231Bi labelled polymersomes and Maarten Paul and Maayke Kuijten for kindly providing the t53BP1-mScarlet construct. This project was funded by STW (project number 13577).

COMPETING INTERESTS

The authors have declared that no competing interest exists.

REFERENCES

1. Dekempeneer Y, Keyaerts M, Krasniqi A, Puttemans J, Muyldermans S, Lahoutte T, et al. Targeted alpha therapy using short-lived alpha-particles and the promise of nanobodies as targeting vehicle. Expert Opin Biol Ther. 2016; 16: 1035-47.
2. Morgenstern A, Bruchertseifer F. Development of Targeted Alpha Therapy from Bench to Bedside. J Med Imaging Radiat Sci. 2019.
3. Raju MR, Eisen Y, Carpenter S, Inkret WC. Radiobiology of alpha particles. III. Cell inactivation by alpha-particle traversals of the cell nucleus. Radiat Res. 1991; 128: 204-9.
4. Pouget JP, Navarro-Teulon I, Bardies M, Chouin N, Cartron G, Pelegrin A, et al. Clinical radioimmunotherapy--the role of radiobiology. Nat Rev Clin Oncol. 2011; 8: 720-34.
5. Kratochwil C, Giesel FL, Bruchertseifer F, Mier W, Apostolidis C, Boll R, et al. (2)(1)(3)Bi-DOTATOC receptor-targeted alpha-radionuclide therapy induces remission in neuroendocrine tumours refractory to beta radiation: a first-in-human experience. Eur J Nucl Med Mol Imaging. 2014; 41: 2106-19.
6. Song H, Hobbs RF, Vajravelu R, Huso DL, Esaias C, Apostolidis C, et al. Radioimmunotherapy of breast cancer metastases with alpha-particle emitter 225Ac: comparing efficacy with 213Bi and 90Y. Cancer Res. 2009; 69: 8941-8.
7. de Kruijff RM, Wolterbeek HT, Denkova AG. A Critical Review of Alpha Radionuclide Therapy-How to Deal with Recoiling Daughters? Pharmaceuticals (Basel). 2015; 8: 321-36.
8. Sofou S, Thomas JL, Lin HY, McDevitt MR, Scheinberg DA, Sgouros G. Engineered liposomes for potential alpha-particle therapy of metastatic cancer. J Nucl Med. 2004; 45: 253-60.
9. Discher DE, Eisenberg A. Polymer vesicles. Science. 2002; 297: 967-73.
10. Wang G, de Kruijff RM, Rol A, Thijssen L, Mendes E, Morgenstern A, et al. Retention studies of recoiling daughter nuclides of 225Ac in polymer vesicles. Appl Radiat Isot. 2014; 85: 45-53.
11. de Kruijff RM, Drost K, Thijssen L, Morgenstern A, Bruchertseifer F, Lathouwers D, et al. Improved (225)Ac daughter retention in InPO4 containing polymersomes. Appl Radiat Isot. 2017; 128: 183-9.
12. Discher BM, Won YY, Ege DS, Lee JC, Bates FS, Discher DE, et al. Polymersomes: tough vesicles made from diblock copolymers. Science. 1999; 284: 1143-6.
13. Discher DE, Ahmed F. Polymersomes. Annu Rev Biomed Eng. 2006; 8: 323-41.
14. Maeda H. Toward a full understanding of the EPR effect in primary and metastatic tumors as well as issues related to its heterogeneity. Adv Drug Deliv Rev. 2015; 91: 3-6.
15. Matsumura Y, Maeda H. A new concept for macromolecular therapeutics in cancer chemotherapy: mechanism of tumoritropic accumulation of proteins and the antitumor agent smancs. Cancer Res. 1986; 46: 6387-92.
16. Lee JS, Feijen J. Polymersomes for drug delivery: design, formation and characterization. J Control Release. 2012; 161: 473-83.
17. Mai Y, Eisenberg A. Self-assembly of block copolymers. Chem Soc Rev. 2012; 41: 5969-85.
18. Thijssen L, Schaart DR, de Vries D, Morgenstern A, Bruchertseifer F, Denkova AG. Polymersomes as nano-carriers to retain harmful recoil nuclides in alpha radionuclide therapy: a feasibility study. Radiochim Acta. 2012; 100: 473-81.
19. Wang G, de Kruijff RM, Abou D, Ramos N, Mendes E, Franken LE, et al. Pharmacokinetics of Polymersomes Composed of Poly(Butadiene-Ethylene Oxide); Healthy versus Tumor-Bearing Mice. J Biomed Nanotechnol. 2016; 12: 320-8.
20. Murdoch C, Reeves KJ, Hearnden V, Colley H, Massignani M, Canton I, et al. Internalization and biodistribution of polymersomes into oral squamous cell carcinoma cells in vitro and *in vivo*. Nanomedicine (Lond). 2010; 5: 1025-36.

21. de Kruijff RM, van der Meer A, Windmeijer CAA, Kouwenberg JJM, Morgenstern A, Bruchertseifer F, et al. The therapeutic potential of polymersomes loaded with (225)Ac evaluated in 2D and 3D in vitro glioma models. Eur J Pharm Biopharm. 2018; 127: 85-91.
22. Kruijff RM, Raave R, Kip A, Molkenboer-Kuenen J, Morgenstern A, Bruchertseifer F, et al. The *in vivo* fate of (225)Ac daughter nuclides using polymersomes as a model carrier. Sci Rep. 2019; 9: 11671.
23. Sanson C, Schatz C, Le Meins JF, Soum A, Thevenot J, Garanger E, et al. A simple method to achieve high doxorubicin loading in biodegradable polymersomes. J Control Release. 2010; 147: 428-35.
24. Wang G, de Kruijff R, Stuart MCA, Mendes E, Wolterbeek HT, Denkova AG. Polymersomes as radionuclide carriers loaded via active ion transport through the hydrophobic bilayer. Soft Matter. 2013; 9: 727-34.
25. Schindelin J, Arganda-Carreras I, Frise E, Kaynig V, Longair M, Pietzsch T, et al. Fiji: an open-source platform for biological-image analysis. Nat Methods. 2012; 9: 676-82.
26. Hartjes TAea. in prep.
27. Chemistry ECoN. Protocol for the elution of the ITU standard $^{255}Ac/^{213}Bi$ radionuclide generator and labelling of DTPA-chelated carriers with ^{231}Bi.
28. Wang G, Hoornweg A, Wolterbeek HT, Franken LE, Mendes E, Denkova AG. Enhanced retention of encapsulated ions in cross-linked polymersomes. J Phys Chem B. 2015; 119: 4300-8.
29. Ossipova O, Tabler J, Green JB, Sokol SY. PAR1 specifies ciliated cells in vertebrate ectoderm downstream of aPKC. Development. 2007; 134: 4297-306.
30. Tinevez JY, Perry N, Schindelin J, Hoopes GM, Reynolds GD, Laplantine E, et al. TrackMate: An open and extensible platform for single-particle tracking. Methods. 2017; 115: 80-90.
31. de Renzis S, Sonnichsen B, Zerial M. Divalent Rab effectors regulate the sub-compartmental organization and sorting of early endosomes. Nat Cell Biol. 2002; 4: 124-33.
32. Jullien D, Vagnarelli P, Earnshaw WC, Adachi Y. Kinetochore localisation of the DNA damage response component 53BP1 during mitosis. J Cell Sci. 2002; 115: 71-9.
33. Yang KS, Kohler RH, Landon M, Giedt R, Weissleder R. Single cell resolution *in vivo* imaging of DNA damage following PARP inhibition. Sci Rep. 2015; 5: 10129.
34. Roobol SJ, Kouwenberg JJM, Denkova AG, Kanaar R, Essers J. Large Field Alpha Irradiation Setup for Radiobiological Experiments. Methods Protoc. 2019; 2.
35. Palmer RBJ, Akhavanrezayat A. Stopping Power of Water, Water-Vapor and Aqueous Tissue Equivalent Solution for Alpha-Particles over Energy-Range O-5-8 Mev. J Phys D Appl Phys. 1978; 11: 605-16.
36. Gao J, Liao J, Yang GY. CAAX-box protein, prenylation process and carcinogenesis. Am J Transl Res. 2009; 1: 312-25.
37. Contini C, Schneemilch M, Gaisford S, Quirke N. Nanoparticle-membrane interactions. J Exp Nanosci. 2018; 13: 62-81.
38. Kulic IM, Brown AE, Kim H, Kural C, Blehm B, Selvin PR, et al. The role of microtubule movement in bidirectional organelle transport. Proc Natl Acad Sci U S A. 2008; 105: 10011-6.
39. Granger E, McNee G, Allan V, Woodman P. The role of the cytoskeleton and molecular motors in endosomal dynamics. Semin Cell Dev Biol. 2014; 31: 20-9.
40. Kouwenberg JJM, de Pooter JA, Wolterbeek HT, Denkova AG, Bos AJJ. Alpha radiation dosimetry using Fluorescent Nuclear Track Detectors. Radiat Meas. 2018; 113: 25-32.
41. Rothkamm K, Barnard S, Moquet J, Ellender M, Rana Z, Burdak-Rothkamm S. DNA damage foci: Meaning and significance. Environ Mol Mutagen. 2015; 56: 491-504.
42. Wang X, Hu X, Li J, Russe AC, Kawazoe N, Yang Y, et al. Influence of cell size on cellular uptake of gold nanoparticles. Biomater Sci. 2016; 4: 970-8.

43. Brinkhuis RP, Stojanov K, Laverman P, Eilander J, Zuhorn IS, Rutjes FP, et al. Size dependent biodistribution and SPECT imaging of (111)In-labeled polymersomes. Bioconjug Chem. 2012; 23: 958-65.
44. Bertrand N, Leroux JC. The journey of a drug-carrier in the body: an anatomo-physiological perspective. J Control Release. 2012; 161: 152-63.
45. Pan C, Kumar C, Bohl S, Klingmueller U, Mann M. Comparative proteomic phenotyping of cell lines and primary cells to assess preservation of cell type-specific functions. Mol Cell Proteomics. 2009; 8: 443-50.
46. Aparicio-Vergara M, Tencerova M, Morgantini C, Barreby E, Aouadi M. Isolation of Kupffer Cells and Hepatocytes from a Single Mouse Liver. Methods Mol Biol. 2017; 1639: 161-71.
47. Reichel D, Tripathi M, Perez JM. Biological Effects of Nanoparticles on Macrophage Polarization in the Tumor Microenvironment. Nanotheranostics. 2019; 3: 66-88.
48. Denz M, Chiantia S, Herrmann A, Mueller P, Korte T, Schwarzer R. Cell cycle dependent changes in the plasma membrane organization of mammalian cells. Biochim Biophys Acta Biomembr. 2017; 1859: 350-9.
49. McCusker D, Kellogg DR. Plasma membrane growth during the cell cycle: unsolved mysteries and recent progress. Curr Opin Cell Biol. 2012; 24: 845-51.
50. Serdiuk T, Lysenko V, Mognetti B, Skryshevsky V, Geloen A. Impact of cell division on intracellular uptake and nuclear targeting with fluorescent SiC-based nanoparticles. J Biophotonics. 2013; 6: 291-7.
51. Bareford LM, Swaan PW. Endocytic mechanisms for targeted drug delivery. Adv Drug Deliv Rev. 2007; 59: 748-58.
52. Cabukusta B, Neefjes J. Mechanisms of lysosomal positioning and movement. Traffic. 2018; 19: 761-9.
53. Bandyopadhyay D, Cyphersmith A, Zapata JA, Kim YJ, Payne CK. Lysosome Transport as a Function of Lysosome Diameter. Plos One. 2014; 9.
54. Schutz I, Lopez-Hernandez T, Gao Q, Puchkov D, Jabs S, Nordmeyer D, et al. Lysosomal Dysfunction Caused by Cellular Accumulation of Silica Nanoparticles. J Biol Chem. 2016; 291: 14170-84.
55. Gerhards NM, Blomen VA, Mutlu M, Nieuwenhuis J, Howald D, Guyader C, et al. Haploid genetic screens identify genetic vulnerabilities to microtubule-targeting agents. Mol Oncol. 2018; 12: 953-71.
56. Staring J, von Castelmur E, Blomen VA, van den Hengel LG, Brockmann M, Baggen J, et al. PLA2G16 represents a switch between entry and clearance of Picornaviridae. Nature. 2017; 541: 412-+.
57. Sgouros G, Roeske JC, McDevitt MR, Palm S, Allen BJ, Fisher DR, et al. MIRD Pamphlet No. 22 (abridged): radiobiology and dosimetry of alpha-particle emitters for targeted radionuclide therapy. J Nucl Med. 2010; 51: 311-28.
58. Behzadi S, Serpooshan V, Tao W, Hamaly MA, Alkawareek MY, Dreaden EC, et al. Cellular uptake of nanoparticles: journey inside the cell. Chem Soc Rev. 2017; 46: 4218-44.
59. Douglas KL, Piccirillo CA, Tabrizian M. Cell line-dependent internalization pathways and intracellular trafficking determine transfection efficiency of nanoparticle vectors. Eur J Pharm Biopharm. 2008; 68: 676-87.
60. de Kruijff RM, Raave R, Kip A, Molkenboer-Kuenen J, Roobol SJ, Essers J, et al. Elucidating the Influence of Tumor Presence on the Polymersome Circulation Time in Mice. Pharmaceutics. 2019; 11.
61. Li R, Zheng K, Yuan C, Chen Z, Huang M. Be Active or Not: the Relative Contribution of Active and Passive Tumor Targeting of Nanomaterials. Nanotheranostics. 2017; 1: 346-57.

62. Zhao Y, Fletcher NL, Liu T, Gemmell AC, Houston ZH, Blakey I, et al. *In vivo* therapeutic evaluation of polymeric nanomedicines: effect of different targeting peptides on therapeutic efficacy against breast cancer. Nanotheranostics. 2018; 2: 360-70.
63. Song L, Able S, Johnson E, Vallis KA. Accumulation of (111)In-Labelled EGF-Au-PEG Nanoparticles in EGFR-Positive Tumours is Enhanced by Coadministration of Targeting Ligand. Nanotheranostics. 2017; 1: 232-43.

Appendix

SUMMARY AND CONCLUSIONS

Ionizing radiation (IR) can induce a wide array of different types of DNA damage and, in the context of cancer therapy, is used to eradicate tumor cells. The underlying success of DNA damage-inducing radiation treatment is the rationale that tumor cells coordinately respond to DNA damage, thereby inducing a variety of responses that induce cell death or inhibit cellular proliferation. However, cells have evolved tightly controlled DNA damage repair mechanisms that can counteract the DNA damaging effects, possibly leading to radiation resistance. The most harmful type of DNA damage are DNA double-stranded breaks (DSBs) that are repaired in two fundamentally distinct manners, Non-Homologous End Joining (NHEJ) and Homologous Recombination (HR), depending on whether a DNA template is used during the process. More understanding how HR and NHEJ function together in DSBs repair, could assist in the search for possibilities to improve cancer therapy based on IR or counter IR resistance.

In cancer therapy, tumors are mostly treated from outside the body, using external beam radiation therapy (EBRT). However, irradiation of tumors deep within the body that reside next to healthy tissue can lead to toxicity. The development of radiopharmaceutical therapy (RPT) has improved treatment of cancers that are located deep in the body and of metastasized disease. In RPT, radionuclides are attached to delivery vehicles and systemically injected, delivering the radiation directly to the tumor. Internal irradiation provides the possibility to use radiation with a high linear energy transfer (LET), which is not an option for external irradiation due to a low penetration depth. High-LET radiation has a large probability to eradicate tumor cells, due to its potential to inflict a high amount of DSBs to cells in close proximity. However, to deliver the high-LET radiation efficiently and what types of DNA damage are inflicted is not yet fully understood.

This thesis describes; (1) The cooperation of NHEJ and HR in IR protection in mice and cells; (2) the development of a novel high-LET external irradiation device; (3) the differences in DSB processing after high- and low-LET irradiation and (4) polymersome processing after cellular uptake to assess efficient and safe delivery of high-LET radionuclides. In this section, we summarize our main findings and suggest future directions in which our research can continue.

In mammals, the two major DNA double-strand break repair pathways, HR and NHEJ, have overlapping as well as specialized roles. The relative contribution of these two DSB repair pathways can differ depending on mammalian developmental stage (i.e. cell type) and on the specific type of DNA damage. This implicates that the combination of NHEJ and HR regulates the grade of IR protection and further understanding how that combination is balanced could lead to more precise radiation treatment. In **Chapter 2,** we generated mice deficient for RAD54 (HR), DNA-PKcs (NHEJ) and both to investigate how NHEJ and HR cooperate in IR induced DNA damage repair. We found that mice lacking DNA-PK_{CS}, but not RAD54, have elevated and sustained p21 expression after IR, particularly in the gut. In addition, DNA-PK_{CS} appeared to play a

role in 53BP1 foci dissolution in both mouse embryonic stem (mES) cells and mouse embryonic fibroblasts (MEFs). Furthermore, RAD54 only contributed to IR protection in DNA-$PK_{CS}^{-/-}$ adult mice or in mES cells. This chapter supports the theory that the absence of DNA-PK_{CS} leads to an enhanced stress response and HR functions as a backup in IR protection with a larger role in undifferentiated cell types. In addition, we show that the use of p21-reporter mice can detect the consequences of DNA damage repair deficiencies with high sensitivity.

The notion of a balanced role between HR and NHEJ after low-LET IR implicates a similar scenario for high-LET irradiation. Indeed, high-LET irradiation is thought to induce complex DNA damage in which HR, having the requirement of a DNA template, plays a larger role than NHEJ. To investigate whether HR or NHEJ have different impact in DSB repair after high-LET irradiation we first addressed a technical problem: commercially available α-particle sources are often smaller in diameter than culture dishes, thereby precluding standardized biological experiments, such as quantitative cell colony formation assays. In **Chapter 3,** we report a novel procedure using large field external α-particle irradiation for standard radiobiological experiments. With the use of this setup, we showed clonogenic survival assays which are reproducible and can be compared with other types of external irradiation. Furthermore, by optimizing the irradiation set-up we add super-resolution microscopy imaging to our toolbox to investigate DNA damage inflicted by α-particles. In **Chapter 4,** we used the newly developed irradiation setup to compare DSB processing after α-particle and X-ray irradiation using live-cell imaging. We found that, in contrast to the already initially larger α-particle-induced 53BP1 foci, X-ray-induced foci increased in 53BP1 protein content and size over time. Moreover, α-particle irradiation induced 53BP1 foci co-localized with multiple individual RPA foci, indicative for multiple resection events at a single damaged site, which was not observed after X-ray irradiation. In conclusion, our results indicate that the condensed energy deposition pattern of high-LET α-particles induces closely interspaced DSBs. The abundance of multiple DSBs in close vicinity throughout the cell nucleus leads to 53BP1 protein insufficiency and ineffective DNA end protection.

In practice, irradiation using α-particles would be internal and not external. Therefore, delivery vehicles (DVs) are designed to specifically deliver the α-particle emitting radionuclides to the target tumor cells. Delivery of radionuclides to a therapeutic target comes with many challenges, such as target specificity, circulation time. However, with the high energy of α-particle emitting radionuclides comes another challenge: recoiling daughter radionuclides break free from their DV and can distribute freely in the body, potentially causing harm to healthy tissue. Robust polymersomes (PMs) could provide support, being highly effective in retaining recoiling daughter radionuclides. In **Chapter 5**, we set out to characterize the cellular uptake of PMs. We found that PM uptake is cell type dependent and mitotic cells have increased uptake. In addition, PM uptake is mediated via endocytosis where after post-uptake transportation went via microtubules, eventually leading to lysosomal aggregates. Furthermore, we show that PMs, which carry α-particle emitting radionuclides, only induce DNA damage to the cell in which they are taken up, as seen in a 2-D cell culture. These findings suggest that PM uptake and process-

ing can vastly differ between cell lines, which could possibly influence DNA damage inducing capabilities. In addition, the assays we report in this chapter provide advanced analysis of PM uptake and processing and should be considered to optimize PMs.

Overall, the studies presented in this thesis show fruitful collaborations between physics, radiology, and biology disciplines in which the basis encompasses: gaining fundamental knowledge of biological processes with the use of technological advances. The novel insights and assays we present could be useful for advancements in clinical treatment or drug development.

Future perspectives

A better understanding how DSB repair cooperates could enlighten new ideas on how to exploit these processes for clinical benefit. The cell biological effects of high-LET irradiation seem vastly different compared to low-LET irradiation. The rising interest in several high-LET treatment options, such as α-particle emitters and proton therapy, emphasize the need for better understanding. Therefore, DSB repair deficient mice or cells in combination with the newly developed high-LET irradiation set-up we present here can prove to be a successful combination to determine what processes are activated after high-LET irradiation. More specifically, α-particle irradiation on DSB repair deficient cells could uncover whether DSBs induced by high-LET irradiation indeed require HR-directed repair or perhaps other pathways that are necessary for repair. In addition, high-LET irradiation inflicts DNA ends that showed resection, even in G1 phases. Other reports show that increasing low-LET irradiation dose leads to 53BP1 exhaustion, which converts limited DNA end resection to hyper-resection, and results in a switch from error-free HR to mutagenic single-strand annealing by Rad52. It would be highly interesting to see whether the reliance on Rad52 also occurs after high-LET irradiation, possibly making Rad52 inhibitors worth to investigate. Moreover, in chapter 4 we show altered DSB processing, possibly caused by perturbed chromatin remodeling. The use of confocal live-cell can provide more spatio-temporal detail on how DSB repair protein cooperate to repair such closely interspaced DSB. Moreover, with the use of super resolution microscopy, the organization of macromolecular protein assemblies could be analyzed, which might provide insight on how chromatin remodeling is regulated after high-LET irradiation. Furthermore, characterized tumor types often have DNA repair defects. Accumulating data demonstrate that DNA repair-defective tumors, in particular those defective in HR, are highly sensitive to DNA-damaging agents. It will be interesting to investigate whether proton radiation can be used to cause enhanced lethality in DSB repair-defective tumors.

On the other hand, for α-particle emitters to be used as therapy, the radionuclides should be injected systemically for internal irradiation. Current delivery strategies show off targeting towards healthy tissue, which could be highly toxic with the use of α-particle irradiation. Many delivery vehicle (DV) strategies have bottlenecks for specificity and circulation time, mostly investigated in mice. The assays provided here can be used to evaluate what factors or cell types determine the off-target delivery and provide inexpensive *in vitro* assays for evaluation.

For example, macrophages are thought to play a major role in fast clearing of DVs and high liver or spleen uptake. Testing *in vitro* whether macrophages have enhanced uptake efficiencies compared to other cell types could help to adjust DVs for longer circulation times. In addition, microfluidic devices can mimic the bloodstream to study how DVs leave the bloodstream and enter cells. Furthermore, our assays are based on 2-D cell culture, it would be highly beneficial to apply these techniques to 3-D applications to gain more insight on how DVs are distributed in the target tumors. Overall, to understand how DVs enter target cells or are taken up by macrophages will help to improve specific targeting in (pre-) clinical settings.

To take the next steps in understanding and improving the topics discussed in this thesis, collaboration between the fields of radiology, biology and physics are crucial. Multidisciplinary research stands at the basis of both technological, fundamental, and clinical breakthrough and should be encouraged.

NEDERLANDSE SAMENVATTING

Ioniserende straling (IR) kan veel verschillende soorten DNA-schade veroorzaken en wordt in de context van kankertherapie gebruikt om tumorcellen uit te roeien. Het onderliggende succes van DNA-schade-inducerende bestralingsbehandeling is de grondgedachte dat tumorcellen gecoördineerd reageren op DNA-schade, waardoor ze een verscheidenheid aan reacties veroorzaken die celdood induceren of cellulaire proliferatie remmen. Cellen hebben echter streng gecontroleerde herstelmechanismen voor DNA-schade ontwikkeld die de DNA-beschadigende effecten kunnen tegengaan, mogelijk leidend tot stralingsweerstand. De meest schadelijke vorm van DNA-schade vormen de dubbelstrengs DNA-breuken (DSB's) die op twee fundamenteel verschillende manieren worden gerepareerd, non-homologous end joining (NHEJ) en homologe recombinatie (HR), afhankelijk van of een DNA-sjabloon wordt gebruikt tijdens de werkwijze. Meer begrip van de samenwerking tussen HR en NHEJ bij het herstel van DSB's, zou kunnen helpen bij het zoeken naar mogelijkheden om kankertherapie op basis van IR te verbeteren of IR-resistentie tegen te gaan.

Bij kankertherapie worden tumoren meestal van buiten het lichaam behandeld met behulp van externe bestralingstherapie (EBRT). Bestraling van tumoren diep in het lichaam die zich naast gezond weefsel bevinden, kan echter tot toxiciteit leiden. Door de ontwikkeling van radiofarmaceutische therapie (RPT) is de behandeling van kankers die diep in het lichaam zijn gelegen en van uitgezaaide ziekten verbeterd. Bij RPT worden radionucliden aan bezorgingsvehikels gehecht en systemisch geïnjecteerd, waardoor de straling rechtstreeks aan de tumor wordt afgegeven. Interne bestraling biedt de mogelijkheid om straling te gebruiken met een hoge lineaire energieoverdracht (LET), wat bij externe bestraling vanwege een lage indringdiepte geen optie is. Hoge-LET-straling heeft een grote kans om tumorcellen uit te roeien, vanwege het potentieel om een grote hoeveelheid DSB's toe te dienen aan cellen in de buurt. Het is echter nog niet helemaal duidelijk hoe de high-LET-straling het meest efficiënt afgeleverd kan worden en welke soorten DNA-schade worden toegebracht.

Dit proefschrift beschrijft; (1) de samenwerking van NHEJ en HR in IR-bescherming bij muizen en cellen; (2) de ontwikkeling van een nieuw extern bestralingsapparaat voor hoge-LET-bestraling; (3) de verschillen in DSB-verwerking na bestraling met hoge en lage LET en (4) polymersome verwerking na cellulaire opname in de zoektocht naar efficiënte en veilige levering van hoog-LET-radionucliden.

In het volgende stuk vatten we onze belangrijkste bevindingen samen en stellen we toekomstige richtingen voor waarin ons onderzoek kan worden voortgezet.

Bij zoogdieren hebben de twee belangrijkste herstelroutes voor dubbelstrengs herstel van DNA, HR en NHEJ, zowel overlappende als gespecialiseerde rollen. De relatieve bijdrage van deze twee DSB-herstelroutes kan verschillen afhankelijk van het ontwikkelingsstadium van zoogdieren (d.w.z. celtype) en van het specifieke type DNA-schade. Dit impliceert dat de combinatie van

NHEJ en HR de graad van IR-bescherming reguleert en een beter begrip van hoe die combinatie in evenwicht is, zou kunnen leiden tot een nauwkeurigere stralingsbehandeling. In **Hoofdstuk 2** hebben we muizen gegenereerd die deficiënt zijn voor RAD54 (HR), DNA-PKcs (NHEJ) en beide om te onderzoeken hoe NHEJ en HR samenwerken bij IR-geïnduceerde DNA-schadeherstel. We ontdekten dat muizen die DNA-PK_{CS} missen, maar niet RAD54, een verhoogde en aanhoudende p21-expressie hebben na IR, vooral in de darm. Bovendien bleek DNA-PK_{CS} een rol te spelen bij het oplossen van 53BP1-foci in zowel muis embryonale stam (mES) cellen als muis embryonale fibroblasten (MEF's). Bovendien droeg RAD54 alleen bij aan IR-bescherming in DNA-$PK_{CS}^{-/-}$ volwassen muizen of in mES-cellen. Dit hoofdstuk ondersteunt de theorie dat de afwezigheid van DNA-PK_{CS} leidt tot een verhoogde stressrespons en HR functioneert als back-up in IR-bescherming met een grotere rol in ongedifferentieerde celtypen. Bovendien laten we zien dat het gebruik van p21-reportermuizen de gevolgen van tekortkomingen in het herstel van DNA-schade met hoge gevoeligheid kan detecteren.

De suggestie van een gebalanceerde rol tussen HR en NHEJ na lage-LET-IR impliceert een soortgelijk scenario na hoge-LET-bestraling. Sterker nog, men denkt dat bestraling met een hoge-LET complexe DNA-schade induceert waarbij HR, met de vereiste van een DNA-template, een grotere rol speelt dan NHEJ. Om te onderzoeken of HR of NHEJ een verschillende impact hebben op DSB-reparatie na bestraling met hoge LET, hebben we eerst een technisch probleem aangepakt: commercieel verkrijgbare α-deeltjesbronnen zijn vaak kleiner in diameter dan kweekschalen, waardoor gestandaardiseerde biologische experimenten, zoals kwantitatieve klonogene overlevingsassays, uitgesloten zijn. In **Hoofdstuk 3** rapporteren we een nieuwe procedure die gebruik maakt van externe bestraling met α-deeltjes met een groot veld voor standaard radiobiologische experimenten. Met het gebruik van deze opstelling hebben we klonogene overlevingsassays getoond die reproduceerbaar zijn en kunnen worden vergeleken met andere soorten externe bestraling. Door de bestralingsopstelling te optimaliseren, voegen we bovendien superresolutie microscopiebeeldvorming toe aan onze toolbox om DNA-schade veroorzaakt door α-deeltjes te onderzoeken. In **Hoofdstuk 4** hebben we de nieuw ontwikkelde bestralingsopstelling gebruikt om DSB-verwerking na α-deeltjes en röntgenbestraling te vergelijken met behulp van live-cell imaging. We ontdekten dat, in tegenstelling tot de reeds aanvankelijk grotere door α-deeltjes geïnduceerde 53BP1-foci, door röntgenstraling geïnduceerde foci in de loop van de tijd toenamen in 53BP1-eiwitgehalte en -grootte. Bovendien induceerde bestraling van α-deeltjes 53BP1-foci die co-gelokaliseerd waren met meerdere individuele RPA-foci, wat indicatief is voor meerdere resectiegebeurtenissen op een enkele beschadigde locatie en wat niet werd waargenomen na bestraling met röntgenstraling. Concluderend geven onze resultaten aan dat het gecondenseerde energie-afzettingspatroon van hoog-LET α-deeltjes DSB's met nauwe tussenruimten induceert. De overvloed aan meerdere DSB's in de directe omgeving van de celkern leidt tot 53BP1-eiwitinsufficiëntie en ineffectieve DNA-eindbescherming.

In de praktijk zou bestraling met α-deeltjes intern en niet extern zijn. Daarom zijn afleveringsvehikels (DV's) ontworpen om specifiek de α-deeltjes die radionucliden afgeven aan de doelwit

tumorcellen af te leveren. De levering van radionucliden aan een therapeutisch doel brengt veel uitdagingen met zich mee, zoals de specificiteit van het doel en de circulatietijd. Met de hoge energie van α-deeltjes die radionucliden uitzenden, komt er echter nog een uitdaging bij: recoiling dochterradionucliden breken los van hun DV en kunnen zich vrij verspreiden in het lichaam, wat mogelijk schadelijk is voor gezond weefsel. Robuuste polymersomes (PM's) zouden ondersteuning kunnen bieden, omdat ze zeer effectief zijn in het vasthouden van recoiling dochterradionucliden. In **Hoofdstuk 5** wilden we de cellulaire opname van PM's karakteriseren. We ontdekten dat PM-opname afhankelijk is van het celtype en dat mitotische cellen een verhoogde opname hebben. Bovendien wordt PM-opname gemedieerd via endocytose, waar na opname het transport via microtubuli ging, wat uiteindelijk leidde tot lysosomale aggregaten. Verder laten we zien dat PM's, die α-deeltjes emitterende radionucliden dragen, alleen DNA-schade veroorzaken aan de cel waarin ze worden opgenomen, zoals te zien is in een 2-D celkweek. Deze bevindingen suggereren dat PM-opname en -verwerking enorm kunnen verschillen tussen cellijnen, wat mogelijk van invloed kan zijn op het vermogen om DNA-schade te induceren. Bovendien bieden de assays die we in dit hoofdstuk rapporteren een geavanceerde analyse van PM-opname en -verwerking en moeten worden overwogen om PMs te optimaliseren.

Over het geheel genomen laten de studies die in dit proefschrift worden gepresenteerd vruchtbare samenwerkingen zien tussen fysica, radiologie en biologie disciplines waarin de basis ligt: het verwerven van fundamentele kennis van biologische processen met behulp van technologische vooruitgang. De nieuwe inzichten en assays die we presenteren, kunnen nuttig zijn voor vorderingen in de klinische behandeling van ziekten of de geneesmiddelenontwikkeling.

CURRICULUM VITAE

Full name:	**Stefan Johan Roobol**
Date of Birth:	**April 9th 1991**
Place of Birth:	**Rotterdam**
Nationality:	**Dutch**

Research Experience

2019 - present	**Post-doc** Erasmus Medical Center – Rotterdam, The Netherlands Department of Molecular Genetics and Radiology & Nuclear Medicine 'Cellular radiation exposure effects of molecular radionuclide therapies'
2015 - 2019	**PhD student** Erasmus Medical Center – Rotterdam, The Netherlands Department of Molecular Genetics and Radiology & Nuclear Medicine 'Ionizing Radiation Quality and Dose Effects on DNA Double Strand Break Repair'
2014 - 2015	**Second Master research internship** Erasmus Medical Center – Rotterdam, The Netherlands Department of Experimental Urology 'Establishing a multimodality toolbox using a spontaneous prostate cancer liver metastasis model'
2013 - 2014	**First master research internship** Hubrecht Institute – Utrecht, The Netherlands Group of Jeroen den Hertog 'Regeneration of the Zebrafish caudal fin and the function of PTP1B'
2013	**Bachelor research internship** Leiden University – Leiden, The Netherlands Department of Molecular Cell Biology 'Scavenger receptors: MARCO and Cd36 in Zebrafish and their role in Tuberculosis'

Education

2015 - 2019	**Doctor of Philosophy (PhD)**, Medical Genetics Centre (MGC) Erasmus Medical Centre – Rotterdam, The Netherlands
2013 - 2015	**Master of Science (MSc)**, Animal Biology & Disease Models Leiden University – Leiden, The Netherlands
2010 - 2013	**Bachelor of Science (BSc)**, Biology Leiden University – Leiden, The Netherlands

LIST OF PUBLICATIONS

Homologous recombination and non-homologous end joining are mutually exclusive in ionizing radiation protection
(Manuscript in preparation)
Roobol SJ, Swagemakers S, Ridwan RY, van Heijningen P, Henderson C, Wolf R, Garinis G, Badie C, Kanaar R, van Gent DC, Essers J.

Comparison of High- and Low-LET Radiation-Induced DNA Double-Strand Break Processing in Living Cells.
(International Journal of Molecular Science, 2020)
Roobol SJ, van den Bent I, van Cappellen WA, Abraham TE, Paul MW, Kanaar R, Houtsmuller AB, van Gent DC, Essers J.

Uptake and subcellular distribution of radiolabeled polymersomes for radiotherapy.
(Nanotheranostics, 2019)
Roobol SJ*, Hartjes TA*, Slotman JA, de Kruijff RM, Torrelo G, Abraham TE, Bruchertseifer F, Morgenstern A, Kanaar R, van Gent DC, Houtsmuller AB, Denkova AG, van Royen ME, Essers J.
**Authors contributed equally*

Large Field Alpha Irradiation Setup for Radiobiological Experiments.
(Methods and Protocols, 2019)
Roobol SJ, Kouwenberg JJM, Denkova AG, Kanaar R, Essers J.

Elucidating the Influence of Tumor Presence on the Polymersome Circulation Time in Mice.
(Pharmaceutics, 2019)
de Kruijff RM, Raavé R, Kip A, Molkenboer-Kuenen J, **Roobol SJ**, Essers J, Heskamp S, Denkova AG.

The CST Complex Mediates End Protection at Double-Strand Breaks and Promotes PARP Inhibitor Sensitivity in BRCA1-Deficient Cells.
(Cell Reports, 2018)
Barazas M, Annunziato S, Pettitt SJ, de Krijger I, Ghezraoui H, **Roobol SJ**, Lutz C, Frankum J, Song FF, Brough R, Evers B, Gogola E, Bhin J, van de Ven M, van Gent DC, Jacobs JJL, Chapman R, Lord CJ, Jonkers J, Rottenberg S.

Other publications

Phagocytosis of mycobacteria by zebrafish macrophages is dependent on the scavenger receptor Marco, a key control factor of pro-inflammatory signalling.
(Developmental and Comparative Immunology, 2014)
Benard EL, **Roobol SJ**, Spaink HP, Meijer AH.

PHD PORTFOLIO

Courses

OIC course	3
5B	1
Safely working in the lab	0.5
Genome maintenance and cancer	0.8
Genetics	3
Biomedical writing	3
Special Topics Course: Chromatin Signalling	2
Research Integrity	0.3
Statistics	2

Workshops

MGC workshop; Dortmund	1
MGC workshop; Leuven(Including organisation as Chair)	3
MGC workshop; Texel	1
NKRV Workshop; Delft	0.25
STW-Workshop; Utrecht	0.25

Congress presentations

Oral

EMIM 2018; San Sebastian	1.5
Radiotherapy Research day	0.25
MGC workshop; Texel	1.5
MGC DDR meeting (Rotterdam)	0.25
EMIM 2019; Glasgow	1.5

Posters

MGC workshop (Leuven)	1
ERR meeting Amsterdam	0.5
WMIC 2017 Philadelphia	1
EMIM 2018 San Sebastian	0.25
Imaging on the Move (Radiology & Nuclear Medicine)	0.25

Attended

MGC workshop (Dortmund)	0.50

CGC Amsterdam	0.25
Egmond aan zee	0.25
Oncode Annual meetings	0.25

Teaching

Courses

Various Nanobiology courses	0.25

Students

Pim Bresselaar (Nanobiology bachelor student)	1
Carolien & Sabrah (NanoBiology minor students)	0.5
Meltem (Master medical student)	0.25
Stijn de Jong (Avans Hogeschool Bachelor student)	1
Irene van den Bent (Nanobiology bachelor student)	1
Total	34

DANKWOORD

Dit was hem dan, proefschift afgerond en (eindelijk) dit hoofdstuk afgesloten. In dit deel wil ik iedereen bedanken die mij geholpen heeft om mijn proefschrift compleet te maken. Zonder jullie was dit nooit gebeurd.

Graag wil ik beginnen met mijn copromotoren. Als eerste dr. Essers. Beste **Jeroen**, bedankt dat jij het vertrouwen in mij had om aan deze taak te beginnen. De kennis die je met me deelde en het enthousiasme dat je op mij overbracht van het begin tot aan het einde van dit project waren precies hetgeen wat ik nodig had om mij opgang te helpen en me over de streep te trekken. Daarnaast was het erg verfrissend en (gek genoeg) motiverend om met mijn directe begeleider meermaals per week gewoon slap te ouwehoeren. Onze fiets-tripjes naar Delft, de lange gesprekken over volleybal en nu de wielren-gekte zullen mij zeker bijblijven. Het was natuurlijk niet altijd 'geouwehoer', je liet me ook af en toe meekijken hoe het achter de schermen gaat bij samenwerkingen met bedrijven, wat mijn interesse altijd heeft gehad. Ik zal ook nooit vergeten dat ik meermaals met prangende vragen voor je kantoor stond, maar jij stoom moest afblazen ten aanzien van een totaal ander onderwerp en ik hierdoor met lege handen stond. Vergis je niet; dit zorgde voor zelfstandigheid en gaf mij uiteindelijk veel vertrouwen. Al met al wil ik je bedanken voor een zeer prettige samenwerking, welke ik de komende tijd nog hoop voort te zetten.

Als tweede dr. van Gent. Beste **Dik**, ook jij bedankt voor het vertrouwen. Jouw scherpe inzichten tijdens de werkbesprekingen hebben mijn verschillende projecten naar een hoger niveau getild. Ik heb veel bewondering voor je interpretatie van resultaten en het 'gemak' waarmee je verder filosofeert. Dit gaf bij een aantal projecten en publicaties de doorslag om het af te ronden of om juist de 'missing-link' te vinden. Ook jou wil ik bedanken voor de prettige samenwerking de afgelopen tijd en we gaan elkaar zeker weer zien op het lab.

Dan gaan we over naar mijn promotoren. Als eerste prof. dr. Kanaar. Beste **Roland**, hartelijk dank dat ik in jou groep mijn promotie onderzoek mocht starten. Al in de eerste paar weken wist ik dat ik op mijn plek zat en dat kwam grotendeels door de sfeer die ook jij in stand houdt. Daarnaast was jouw input tijdens de werkbesprekingen precies wat ik af en toe nodig had. Er werd gewoon gezegd waar het op staat, om daarna weer met goede moed verder te kunnen met mijn onderzoek. Het was ontzettend prettig om in de eindsprint van dit proefschrift met een of twee meetings een richting te krijgen waar we naar toe konden werken. Ik hoop dat ik ook de komende 2 jaar weer veel van je mag leren in de volgende stap van mijn carrière.

Als tweede mijn andere promotor, prof. dr. De Jong. Beste **Marion**, ook jij hartelijk dank dat ik mocht beginnen als OIO onder jouw vleugels. We hebben het al een aantal keren tegen elkaar gezegd: het project is anders verlopen dan verwacht. Maar dat dat heeft de interesse in het meedenken met het project zeker niet verminderd. Hoewel mijn project inderdaad steeds iets verder van de (toenmalige) SPECTRIM-groep ging staan, was jouw input tijdens de meetings altijd waardevol. Ik heb er enorm veel bewondering voor hoe jij, ondanks alles, de SPECTRIM-

en nu TRACER-groep laat uitbreiden en naar een hoger niveau tilt. Ik kijk uit naar de komende 2 jaar waarin onze interesses zeker weer dichter bij elkaar zullen te komen liggen.

Over naar mijn kleine commissie: Prof. dr. Houtsmuller, Prof. dr. ir. Marteijn en Dr. ir. Denkova. Hartelijk dank voor het accepteren van de taak om mijn proefschrift te beoordelen. Dan mijn grote commissie: Dr. Nonnekens en Dr. Krawczyck. Ook jullie bedankt voor het plaatsnemen in mijn promotiecommissie.

Ik ben ongeveer 3x van lab-bench gewisseld waardoor ik mij eigenlijk in zowel lab 655 (nu 702C) als in lab 663 (nu 702D) thuis voel. De mensen die in deze twee labs hebben gewerkt of eraan gelieerd waren hebben mij enorm geholpen de afgelopen jaren. Of het nu ging om kleine vragen over een antilichaam of grotere vragen over de zin van het leven, altijd was er antwoord en konden de kleinste gesprekken uitmonden in één groot lab vol gezelligheid. De combinatie waarin er zowel serieus gediscussieerd als gerelativeerd kon worden, maakte het lab een tweede thuis. Een werkplek waar ik met veel plezier heen ging en nog steeds ga. Ik denk dat wij boffen met zo'n sfeer, wat alles leuker maakt. Ook als er experimenten tegenzitten of simpelweg geestdodend zijn.

Het opsommen van namen van zo'n grote groep gaat mij waarschijnlijk zeer slecht af; ik vergeet er vast wel één. Dus, aan iedereen die zich aangesproken voelt, mijn dank is groot. Next to the labs of 702C and D, are of course the other conjoining labs of 702. In addition, the groups of the other corridors of the 7th floor, which houses all other colleagues of the Molecular Genetics. As I said before in Dutch, summing up names makes me forget some. So, I want to thank all the current and previous colleagues for any fruitful discussion or burning questions I had. Good luck with your careers and future plans.

Dan zijn er een aantal die ik toch even wil noemen, vanwege uiteenlopende redenen.

Yanto, zonder jou had ik waarschijnlijk niet in deze positie gekomen. Nu je constant in de bunker bent, hoop ik dat we snel weer wat feestjes kunnen bijwonen. **Kishan**, ons contract overlapte 1 dag. Dat was genoeg! Bedankt voor alle gesprekken op en rond het terras, die hebben zeker geholpen met de laatste loodjes. Grappig dat we nu samen weer een nieuwe fase in gaan, spannend! **Nicole**, als ik ergens een ongezouten mening over wil hebben ben ik bij jou aan het juiste adres. Naast dat ik als Rotterdammert dit weleens kon gebruiken, bleek het in sommige situaties ook heel waardevol om de juiste beslissing te nemen. **Danny**, het feit dat je mijn paranimf bent zegt denk ik al genoeg. Je bent een maatje geworden op het lab en buiten het lab om. **Thom,** jij bent erbij gekomen en de 3 musketiers waren compleet. De gekkigheid die wij met z'n drieen uithalen hebben mij zeker uit een soort 'schrijf-sleur' gehaald. Daarnaast kan het gesprek binnen 1 seconde wél over iets nuttigs gaan. **Maarten**, bedankt dat je mij in de wereld van microscopie geholpen hebt. Hoe snel en makkelijk jij ingewikkelde microscopen bedient en de data daaruit (kritisch) analyseert is indrukwekkend. Ik hoop met mijn nieuwe projecten nog veel met je samen te werken. **Julie**, jij was degene die mij mijn eerste rondleiding gaf op de afdeling, net voor (of na?) mijn sollicitatiegesprek. We hebben veel jaren in hetzelfde kantoor gezeten en nu heb je mij het vertrouwen gegeven om als postdoc in jouw groep aan

mijn volgende carrière-stap te werken. Bedankt hiervoor! Ik kijk uit naar onze samenwerking de komende tijd en ook nog vele rondjes op de racefiets!

To the TRACER-group. As I said to Marion, my PhD-project gradually parted ways from the TRACER-group and the CIL lab. However, during my presentations or discussions with you, your input was most valued and indeed, changed the way I looked at some results or experiments. For the better of course! Apart from work-related things, the Christmas parties of the past 4 years were legendary which I always will remember. Let's hope in 2021 we can repeat that legendary-ness again. To all of my current and previous colleagues: good luck in finishing your projects. Last year I was, and coming year I will be around much more frequently. I'm looking forward to it!

Zonder de hulp van het OIC had ik dit proefschrift nooit kunnen afmaken. In elk hoofdstuk zijn jullie microscopen aan bod gekomen en daarnaast is jullie input en ervaring van onschatbaar waarde gebleken. **Adriaan**, jouw input tijdens onze knusse meetings in jouw kantoor was zeer waardevol en wees me soms naar totaal onverwachtte richtingen. **Thomas en Martin**, ons project met de polymersomes kwam in een stroomversnelling, mede door jullie eerder opgedane kennis. **Johan**, jouw hulp om de polymersomes in beeld te brengen met SIM heeft een hoop diepte aan het paper gegeven. **Gert-Jan**, jouw enthousiasme over de FNTDs en andere objecten die ik in beeld wilde brengen werkte zeer aanstekelijk. **Gert**, zonder jouw voorwerk en hulp bij het analyseren van bewegende 53BP1 foci was het niet gelukt. **Tsion,** zonder jouw hulp waren die bewegende 53BP1 foci nooit goed vastgelegd. Allemaal hartelijk dank!

Over naar Delft, het reactor instituut, de groep van **Antionia.** Bedankt voor de gastvrijheid om daar te komen en experimenten te doen. **Astrid,** onder jouw begeleiding ging het altijd goed en je had de beste ideeën om de experimenten toch uit te voeren. Ik zal de zomermiddag nooit vergeten toen alles op het lab besmet was en ik op slippers naar huis moest. **Guzman**, thank you for always providing us with plenty of polymersomes. Your enthusiasm for good coffee was inspiring! **Robin**, bedankt voor het beantwoorden van al mijn vragen omtrent hoe polymersomes gelabeled en/of opgenomen worden. Daarnaast zijn jouw data over circulatietijden zeer intrigerend en ben ik benieuwd wat er nog meer uitkomt. **Jasper**, de snelheid van het afronden van jouw proefschrift is ongeëvenaard, ik bleef iets achter. Jouw alpha-stralings apparaat heeft veel losgemaakt bij mij en in mijn onderzoek. Bedankt voor je hulp bij het perfectioneren van dit apparaat en de artikelen die ermee gemoeid zijn.

Aan veel van dit werk hebben ook studenten gewerkt. **Pim, Stijn, Carolien, Sabrah en Irene,** jullie inzet heeft zeker geholpen en het was ook zeer leerzaam voor mij om jullie te begeleiden in de afstudeerstages.

Tussen de experimenten door gingen de **MGC-PhD-studenten** een aantal keren naar een workshop. Naast het wetenschappelijke programma, zal ik de nachten in de verschillende kroegen in Dortmund, Leuven en op Texel nooit vergeten. Dank voor deze weekjes fun.

Ook de steun buiten de werkomgeving heeft bijgedragen aan het tot stand komen van dit proefschrift. In dit volgende stukje wil ik diegenen bedanken die interesse toonden in wat ik de afgelopen jaren aan het doen was.

Alle vrienden en teamgenoten van **VCN**, hartelijk dank voor de interesse. Maar voornamelijk voor de kans om mijn stoom af te blazen na soms frustrerende en lange dagen of weekenden op het lab. Het steekt mij nog steeds dat ik (deels) door dit proefschrift de opmars van Heren 1 heb moeten missen, die tot in de eredivisie is opgeklommen. Als alles mee zit hoop ik nog veel met volleybal te maken te krijgen de komende tijd, in of buiten het veld.

Daarnaast zijn er ook vrienden naast het volleybal geweest die interesse in mijn onderzoek hebben getoond. Het klinkt misschien gek, maar alleen al de getoonde interesse was steun. Het uitleggen van mijn onderzoek aan iemand die niets tot nauwelijks iets van het onderwerp weet is lastig, maar creëerde voor mij juist hele duidelijke lijnen om het onderzoek voort te zetten. Ook hier heb ik er een aantal in het bijzonder. **René**, ik hoop dat dit boekje je nu wat meer (of minder?) duidelijkheid geeft. **Thomas, Marit, Michael, Eveline, Marcel en Myrthe,** de middagen, avonden of nachten met jullie hebben óók bijgedragen aan dit stuk. Al was het alleen maar om even te klagen of om gewoon heel veel bier te drinken. **Vu luitjes & consorten, fantastic 4 en Long time no see** groepjes, ook jullie bedankt voor het aanhoren van een soms ietwat cryptische beschrijving van mijn werkzaamheden. Boven alles: bedankt voor de gezelligheid! Op naar nog meer jaren.

Naast vrienden is er altijd familie. Ik wil alle leden van de **Roobol, Bouts, en Waasdorp** families hartelijk bedanken voor de interesse. Niet al te lang geleden heb ik nog wat familie erbij gekregen. Ook alle **van Thiel, van der Steene en Kluver** familie wil ik bedanken voor de interesse. Er was altijd wel de vraag: “hoe gaat het met je onderzoek?” En dan kon ik even mijn ei kwijt.

Oma, deze mijlpaal pakt u gewoon nog mee hoor. Er komt er dit jaar nog eentje, ook daar bent u bij.

Pa en ma, de basis die jullie ons thuis hebben gegeven is van onschatbare waarde. Jullie steun, en af en toe een schop onder mijn hol, heeft er mede voor gezorgd dat ik alles uit mijn opleiding heb willen en kunnen halen. Ik kan denk ik nooit genoeg zeggen hoe dankbaar ik hiervoor ben. Jullie zijn mijn voorbeelden!

Dennis, je staat bij de verdediging achter mij als paranimf, maar eigenlijk meer als mijn broer(tje). Onze band is de afgelopen jaren heel sterk geworden waar ik heel veel waarde aan hecht. Ik ben enorm trots op hoe jij je de afgelopen tijd hebt ontwikkeld en kijk uit naar een nóg hechtere band als ome Dennie.

Bibi, lieve bieb, bedankt voor je begrip, steun en liefde de afgelopen jaren. Jij hebt gezorgd voor een stabiele basis in ons thuis en liet me zien hoe erg dat nodig was. Hoe leuk ook al die feestjes tussendoor. Ik ben enorm trots op wat we samen in zo’n korte tijd hebben opgebouwd. Hoewel we met onze kat **Ony** al een raddraaier in huis hebben, krijgen we in juni een nieuwe huisgenoot die ons leven op z’n kop zal zetten. Ik kan niet wachten om dit met jou te beleven, ik hou van je!